IntechOpen

IntechOpen Book Series
Heat and Mass Transfer, Volume 1

Heat and Mass Transfer

Advances in Modelling and Experimental Study for Industrial Applications

Edited by Yong Ren

HEAT AND MASS TRANSFER - ADVANCES IN MODELLING AND EXPERIMENTAL STUDY FOR INDUSTRIAL APPLICATIONS

Edited by **Yong Ren**

Heat and Mass Transfer - Advances in Modelling and Experimental Study for Industrial Applications
http://dx.doi.org/10.5772/intechopen.71818
Edited by Yong Ren

Part of IntechOpen Book Series: Heat and Mass Transfer, Volume 1
Book Series Editor: Yong Ren

Contributors
Dae-Won Cho, Desmond Adair, Kairat Ismailov, Zhumabay Bakenov, Ramesh G K, Esteban Quijada-Maldonado, Wytze Meindersma, André De Haan, Wu-Yang Sean, Honda (Hung-Ta) Wu, Tsair-Wang Chung, Xiaogang Yang, Weibin Shi, Jie Yang, Guang Li, Yuan Zong

First published in London, United Kingdom, 2018 by IntechOpen
IntechOpen is the global imprint of INTECHOPEN LIMITED, registered in England and Wales, registration number:
11086078, The Shard, 25th floor, 32 London Bridge Street
London, SE19SG – United Kingdom
Printed in Croatia

British Library Cataloguing-in-Publication Data
A catalogue record for this book is available from the British Library

Additional hard copies can be obtained from orders@intechopen.com

Heat and Mass Transfer - Advances in Modelling and Experimental Study for Industrial Applications, Edited by Yong Ren
p. cm.
Print ISBN 978-1-78923-772-6
Online ISBN 978-1-78923-773-3
ISSN 2631-6196

IntechOpen Book Series

Heat and Mass Transfer

Volume 1

Dr Yong Ren is an associate professor at the University of Nottingham Ningbo China (UNNC). He obtained his BEng degree in mechanical engineering at the Beihang University, and was awarded his PhD degree in mechanical engineering at the Hong Kong Polytechnic University for the investigation of centrifugal microfluidic flow and mixing with applications in cell culture and cell lysing, and the research led to automated bio-sample preparation and nucleic acid analysis for lab-on-a-chip applications. He has worked as a research assistant at the Hong Kong Polytechnic University, and postdoctoral research associate at the University of Hong Kong before joining UNNC. He has a broad range of academic interests including microscale fluid dynamics, enhanced heat transfer, CFD modelling, multiphase flow, microfluidic device fabrication, biomaterial synthesis, and biomedical applications using droplet microfluidics.

Book Series Editor and Editor of Volume 1: Yong Ren
University of Nottingham Ningbo, China

Scope of the Series

Heat and mass transfer are ubiquitous transport phenomena in manifold fields from the natural environment and living organisms to engineering processes. This book series will cover the latest advances in applying fundamental heat and mass transfer theory and newly developed technologies and materials for solving practical industrial engineering, biomedical and health care problems, while tackling challenges arising from limitations of existing theory and methods that may be associated with simplified assumptions, inaccuracy of fabrication process and/or measurement instruments.
This book series aims to promote developments in basic research on heat and mass transfer phenomena and serve as a platform for the exchanging of new ideas to boost further development.

Topics may include:

- New analytical modelling and numerical methods of engineering thermodynamics
- New technology or methods for material thermal property measurement and correlation
- Heat and mass transfer in flow flow and chemical reactions
- Environmental applications of heat and mass transfer
- Biomedical applications of heat and mass transfer
- Heat and mass transfer in development of functional material

Contents

Preface

Heat and mass transfer is one of the most important engineering disciplines. An understanding of the transport processes from mass, momentum and energy perspectives is indispensable to effective and efficient application of a number of technologies related to energy, materials, food processing, manufacturing and chemical processes. Heat and mass transfer research areas are increasingly linked with microfluidics and nanofluid, leading to new challenges and opportunities. New developments in heat and mass transfer enhancement techniques and computational methods have been proposed recently. This book focuses on the latest advances in applying fundamental heat and mass transfer theory, using experiments or novel mathematical and CFD modelling technologies to address a wide range of practical engineering problems of interest, including bubbly flow in column reactors, Casson nanofluid, hydrate dissociation in porous media, surface tension effect on water vapor absorption, battery thermal management, mass transfer in extractive distillation, molten pool behavior for submerged arc welding process, as well as the characterization of structure and property factors when designing a plate heat exchanger. The presented interesting results and findings in the book are closely related to industrial applications.

We sincerely hope that the readers will enjoy the seven chapters in this book, which will contribute to advancing our understanding of heat and mass transfer processes to develop new and exciting technologies for future demands.

Yong Ren
Associate Professor
University of Nottingham Ningbo
China

Section 1

Advances in Modelling of Heat and Mass Transfer

Chapter 1

Modeling and Analysis of Molten Pool Behavior for Submerged Arc Welding Process with Single and Multi-Wire Electrodes

Dae-Won Cho

Additional information is available at the end of the chapter

http://dx.doi.org/10.5772/intechopen.76725

Abstract

This chapter describes the procedure of modelling and analysis of molten pool behavior for submerged arc welding process with single and multi-electrodes. As submerged arc welding process is conducted under the covered flux, it is very difficult to extract the various arc shapes and its physical models such as arc heat flux, arc pressure, electromagnetic force, droplet impingement and heat source by consumed flux. This chapter suggests the way to extract the various arc models for submerged arc welding process for single and multi-wire electrodes. As the droplet movements in submerged arc welding process are different from the arc current, this chapter tries to make the flux-wall guided droplet impingement models for low current value (I < 500 A) and spray droplet impingement model for high current value. In high current single electrode submerged arc welding, the molten pool flow pattern for different electrode angle and welding signal wave forms (DC and AC) are analyzed. This chapter also modeled and analyzed the molten pool behaviors for multi-wire electrodes in submerged arc welding process with an arc interaction models for different current values.

Keywords: computational fluid dynamics (CFD), submerged arc welding (SAW), molten pool flow, arc interaction, multi-wire electrode

1. Introduction

Submerged arc welding (SAW) is a very complex process that includes physical and chemical reactions. Moreover, it is very difficult to investigate the whole SAW process using numerical simulations [1–4]. However, the molten zone and heat-affected zone (HAZ) could be estimated using the finite element method (FEM) and considering just the conduction heat transfer.

Wen et al. [1] modeled multi-wire SAW of thick-wall line pipe and calculated the thermal distributions under various welding conditions. Sharma et al. [2] predicted the temperature distributions and angular distortions in single-pass butt joints using three-dimensional simulations. Mahapatra et al. [3] suggested and validated a volumetric heat source model of twin-wire SAW by using different electrode diameters and polarities. Kiran et al. [4] simulated a three-dimensional heat transfer of a V-groove tandem SAW process for various welding conditions using FEM. However, these studies with FEM only considered the heat conduction transfer in the welding process, which is insufficient to explain the curve weld bead such as fingertip penetration.

To overcome these disadvantages, computational fluid dynamics (CFD) is widely used to investigate molten pool flows and final weld beads because it makes it possible to approach the welding process more realistically [5]. Considering the importance of weld pool convection in the welding process, numerous researchers have attempted to analyze the heat transfer and fluid flow. Kim et al. [6] calculated the convective heat transfer and resultant temperature distributions for a filet gas metal arc welding (GMAW) process. Kim et al. [7] obtained the thermal data and analyzed the molten pool flows for various driving forces in stationary gas tungsten arc welding (GTAW). However, these studies assumed that the welding process was in a quasi-steady-state. Thus it was very difficult to approximate the droplet impingent and arc variation with alternating current (AC). Therefore, it is necessary to apply a transient analysis to the welding simulation because it can detect the free surface variation during the simulation time. One transient analysis method is the volume of fluid (VOF) method, which can track the molten pool surface; therefore, the variable models from arc plasma could be implemented in the simulations. Cho et al. [8] calculated the electromagnetic force (EMF) with mapping coordinates in V-groove GTAW and GMAW, and then applied it to the numerical simulation to obtain the dynamic molten pool behavior and final weld bead using the commercial software, Flow-3D. With the advantage of VOF transient simulation, Cho et al. [9] could calculate unstable molten pool flow patterns such as humping and overflow in V-groove positional GMAW. Cho et al. [10] obtained the heat flux distribution of the arc plasma in gas hollow tungsten arc welding (GHTAW) using the Abel inversion method and applied it to the VOF model to predict the molten zone area. Additionally, a more complex welding process can also be calculated by VOF. Cho and Na [11] conducted a laser welding simulation that included the multiple reflection and keyhole formation. Moreover, Cho and Na [12] conducted the three-dimensional laser-GMA hybrid welding, which adopted the laser welding and GMAW. Han et al. [13] compared the driving forces for the weld pool dynamics in GTAW and laser welding. The VOF method could also be applied to describe the alloying element distributions and pore generation in the laser-GMA hybrid welding process [14].

The modeling and the molten pool flow analysis of SAW process are mostly conducted by Cho et al. [15–21]. Cho et al. [15] conducted molten pool analysis of SAW for single electrode for high-current ($I > 500$ A) condition with spray metal transfer droplet impingement. They considered electrode angle and wave form and modeled to analyze the molten pool behavior for single electrode direct current (DC) and alternative current (AC) welding signals. It was found that the penetration of weld bead is closely related with electrode angle and waveform of welding signal. Cho et al. [16] also found that droplet impingement of low-current ($I < 500$)

could be expected as a flux-wall guided (FWG) metal transfer using CFD simulation. They modeled FWG metal transfer with a moving cylinder and randomly directed droplet impingement. Therefore, it is possible to simulate how porosity can be trapped in the V-groove joint with a FWG metal transfer. For better productivity, the multi-electrode SAW process is proposed. Kiran et al. [17] developed physical and regression equations to predict the arc interaction and arc size as a function of the welding conditions for tandem submerged arc welding process. They modeled arc center displacements for tandem SAW under different welding conditions with a spring model. It was found that the arc center displacement of high current shifted less while that of low current shifted wider. Cho et al. [18] applied the arc interaction effect to simulate the molten pool behavior for tandem SAW process. They compared the various molten pool flow patterns where the combinations of the welding signals were different. Moreover, they found that the direction of droplet impingement was very important to expect the welding penetration. Kiran et al. [19] analyzed the temperature histories of tandem SAW CFD simulations within the same heat input. They compared cooling times from 800 to 500°C and volume fractions for different welding conditions and they found that molten pool behavior played an important role to decide the volume fraction and micro hardness. Cho et al. [20] analyzed the flux consumption rate for tandem SAW process where the heat inputs were the same except the combination of welding signals (current and voltage). They found that the arc interaction, droplet impingement direction and metal transfer mode (spray & FWG) affected the overall flux consumption rates. Kiran et al. [21] modeled three wire SAW molten pool simulation which considered arc center displacement and droplet impingement with a physical approach and then analyzed molten pool flow patterns. This chapter briefly introduces the contents how to model and analyze the molten pool behaviors from numerical simulations for single and multi-wire SAW process.

2. Modeling of molten pool behavior for SAW process

2.1. CFD modeling for single electrode

Figure 1 shows a schematic diagram of SAW to allow the following characteristics to be understood [15]: (a) the flux and molten slag cover the overall weld bead and, (b) the fabricated flux wall protects the flux cavity.

Although it is very difficult to observe the metal transfer of SAW, some previous studies succeeded in capturing the motion of a droplet in SAW. Franz [22] and Van Adrichem [23] observed the metal transfer through a ceramic tube using a X-ray cinematography and found that drops travel in free flight to the weld pool, or they may project sideways to collide with the molten flux wall. This metal transfer in SAW is the so-called flux-wall guided (FWG) transfer, as shown in **Figure 2**.

During the SAW process, a small portion of the flux is melted and consumed. Chandel [24] found that the flux consumption relies upon three sources: (a) conduction from the molten metal, (b) radiation from arc and (c) resistance heating of the slag. However, their individual

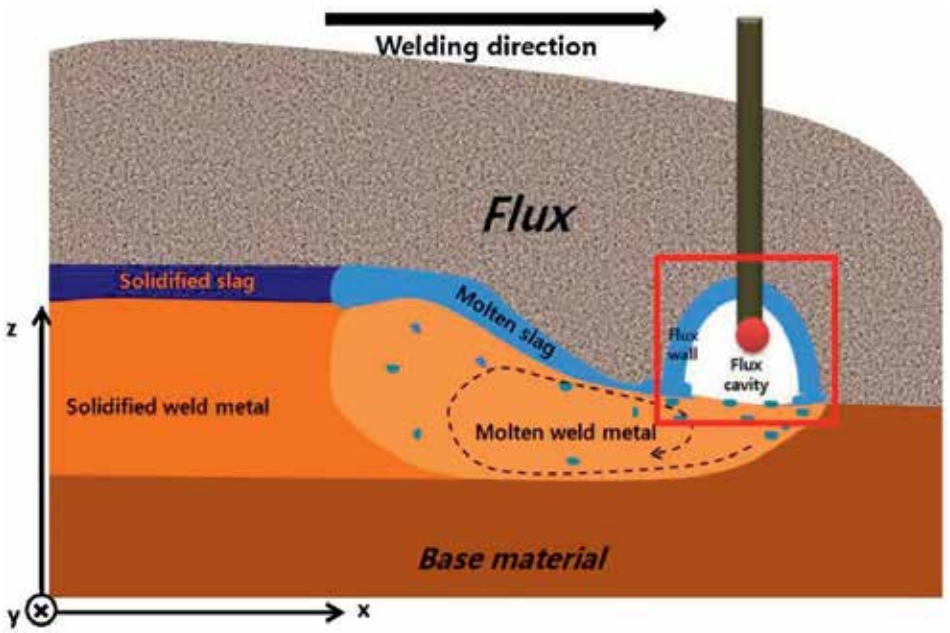

Figure 1. Schematic of SAW [15].

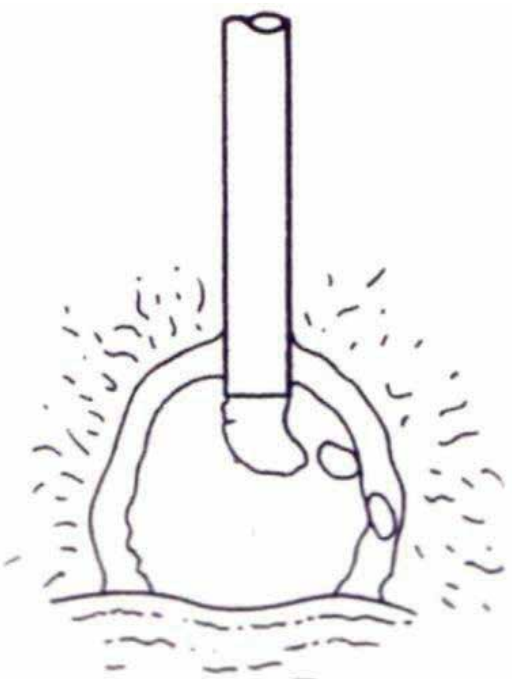

Figure 2. FWG transfer in SAW [15].

http://dx.doi.org/10.5772/intechopen.76725

contributions to flux consumption are still unclear. In any case, the total flux consumption can be calculated by measuring the mass of the flux used. Renwick and Patchett [25] analyzed the relations between welding parameters and the flux consumption and found that flux consumption initially increased with increasing current, reached a maximum, and then decreased. Chandel [24] also measured the flux consumption of SAW with various welding parameters and showed that the flux consumption reached a peak value at 500 A and decreased at higher currents, as shown in **Figure 3** [15]. This decrease at a high current is a result of the increasing current causing the droplet size to decrease. Therefore, the contact area between the droplet and the flux-wall could be decreased, as shown in **Figure 4**. In short, FWG transfer is difficult to observe at high current and the spray mode of transfer can be expected to be considered in high current SAW [15].

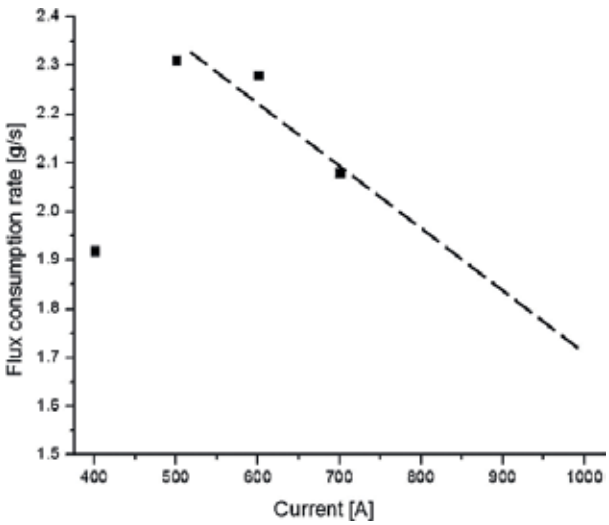

Figure 3. Current vs. flux consumption rate in single DC [15].

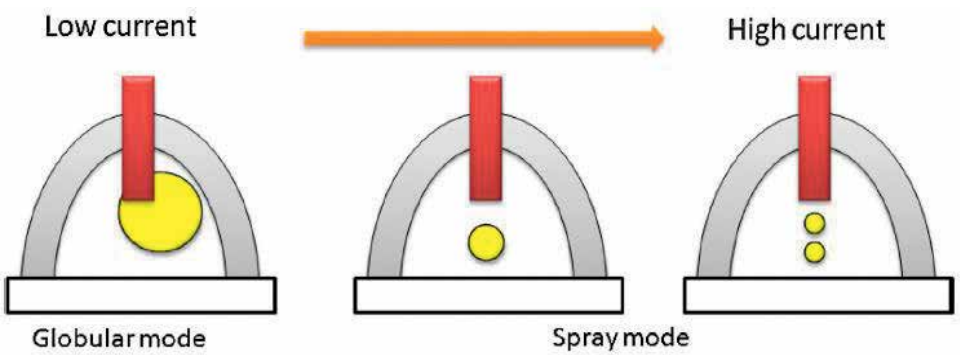

Figure 4. Expected metal transfer in single SAW process [15].

2.1.1. Governing equations

The governing equations in the CFD simulation of a weld pool involve the mass conservation equation, momentum conservation equation (Navier-Stokes equations), and energy conservation equation. The time step used in the numerical simulation is 0.00001 s. To describe the molten pool behavior, the commercial package, Flow-3D was widely used [15, 16, 18, 21] (**Table 1**).

- Momentum equation

$$\frac{\partial \vec{V}}{\partial t} + \vec{V} \cdot \nabla \vec{V} = -\frac{\nabla p}{\rho} + \nu \nabla^2 \vec{V} + \frac{\dot{m}_s}{\rho}\left(\vec{V}_s - \vec{V}\right) + f_b \tag{1}$$

- Mass conservation equation

$$\nabla \cdot \vec{V} = \frac{\dot{m}_s}{\rho} \tag{2}$$

- Energy equation

$$\frac{\partial h}{\partial t} + \vec{V} \cdot \nabla h = \frac{1}{\rho} \nabla \cdot (k \nabla T) + \dot{h}_s, \tag{3}$$

where

$$\begin{aligned} h &= \rho_s C_s T \qquad\qquad (T \le T_s) \\ h &= h(T_s) + h_{sl} \frac{T - T_s}{T_l - T_s} \qquad (T_s < T \le T_l) \\ h &= h(T_l) + \rho_l C_l (T - T_l) \quad (T_s < T \le T_l) \end{aligned} \tag{4}$$

- VOF equation

$$\frac{\partial F}{\partial t} + \nabla \cdot \left(\vec{V} F\right) = \dot{F}_s \tag{5}$$

2.1.2. Boundary conditions

There is no heat loss from the radiation, convection and evaporation on the molten pool surface because slag and flux cover the overall weld bead as shown in **Figure 1**. In SAW, the heat is input from the slag to the molten pool and lost from the molten pool to the slag. However, the summation of the heat input and heat loss can be regarded as the slag heat transfer (q_s), and the energy boundary condition in equation (6) is used [15, 16, 18, 21].

$$k \frac{\partial T}{\partial \vec{n}} = q_a + q_{slag\_input} - q_{slag\_loss} = q_a + q_s. \tag{6}$$

Symbol	Nomenclature	Symbol	Nomenclature
ρ	Density, (solid:7.8, liquid:6.9, g/cm3)	p_A	Arc pressure
$\vec{V}$	Velocity vector	R_c	Radius of the surface curvature
ν	Kinematic viscosity	γ	Surface tension
$\dot{m}_s$	Mass source of droplet	r_w	Radius of wire, 2.0 mm
h	Enthalpy	r_d	Radius of droplet, 2.1 mm
$\dot{h}_s$	Enthalpy source of droplet	WFR	Wire feed rate
$\vec{V}_s$	Velocity vector for mass source	C_s	Specific heat of liquid, 7.32x 10^6 erg/g s K
f_b	Body force	C_p	Specific heat
h_s	Enthalpy of solid	T_o	Room temperature, 298 K
h_{sl}	Enthalpy between solid and solid	η_s	Slag efficiency of SAW
T_s	Solidus temperature, 1768 K	η_d	Droplet efficiency of SAW
T_l	Liquidus temperature, 1798 K	$\dot{m}_f$	Flux consumption (g/s)
F	Fraction of fluid	x_0, y_0	Location of the electrode center in x and y directions
$\dot{F}_s$	Volume source of droplet	x_1, y_1	Location of the arc center in x and y directions
k	Thermal conductivity	J_0	First kind of Bessel function of zero order
$\vec{n}$	Normal vector to free surface	μ_0	Permeability of vacuum, 1.26 × 10^6 H/m
q_a	Heat input from arc plasma	μ_m	Material permeability, 1.26 × 10^6 H/m
q_d	Heat input from droplet	J_z	Vertical component of the current density
q_{slag_input}	Heat transfer from slag to molten pool	J_r	Radial component of the current density
q_{slag_loss}	Heat transfer from slag to molten pool	B_θ	Angular component of the magnetic field
η_a	Arc efficiency of SAW	σ_x, σ_y	Effective radius of the arc in x-direction and y-direction
I	Current	Γ_s	Surface excess at saturation
V	Voltage	$\overline{R}$	Universal gas constant
F_b	Buoyancy force	k_1	Constant related to the entropy of segregation
γ_m^0	Surface tension of pure metal at melting point	a_1	Weight percent of sulfur
A	Negative surface tension gradient for pure metal	I_L, I_T	Current of leading and trailing electrodes
ΔH^0	Standard heat of adsorption	l_L, l_T	Arc length of leading and trailing leading electrodes
X_L, X_T	Arc center position of x-direction for leading and trailing electrodes	β_n^{ij}	Coefficients of effective radius model
$B_{\theta L}, B_{\theta T}$	Angular component of the magnetic field for leading and trailing electrodes	d	Distance between leading and trailing electrode
σ_{RL}, σ_{FL}	Rear and front effective radii of leading arc in x-direction	J_{zL}, J_{zT}	Vertical component of the current density for leading and trailing arcs

Symbol	Nomenclature	Symbol	Nomenclature
σ_{RT}, σ_{FT}	Rear and front effective radii of trailing arc in x-direction	J_{rL}, J_{rT}	Radial component of the current density for leading and trailing arcs
q_{aL}, q_{aT}	Arc heat flux for leading and trailing electrodes	P_{aL}, P_{aT}	Arc heat flux for leading and trailing electrodes

Table 1. Properties and constants used in simulations.

Previous studies found that the thermal efficiency of SAW is between 0.90 and 0.99, and many studies have used a thermal efficiency of 0.95 in numerical simulations [15, 16, 18, 21]. It is reasonable to use total thermal efficiency of 0.95 with the heat transfer from the arc plasma, droplets, and molten slag to the weld pool [15, 16, 18, 21].

$$\eta_a = \frac{q_a + q_d + q_s}{VI} \approx 0.95 \tag{7}$$

The pressure boundary on the free surface is applied as follows:

$$p = p_A + \frac{\gamma}{R_c}. \tag{8}$$

- Droplet model

The droplet efficiency relies on the wire feed rate and it is possible to be calculated using Eqs. (9) to (11). The droplet efficiency can be varied from the wire feed rate and welding signals [15, 16, 18, 21].

$$f_d = \frac{3r_w^2 WFR}{4r_d^3} \tag{9}$$

$$q_d = \frac{4}{3}\pi r_d^3 \rho [C_s(T_s - T_o) + C_l(T_d - T_s) + h_{sl}] f_d, \tag{10}$$

$$\eta_d = \frac{q_d}{VI}. \tag{11}$$

For the high current (I > 500 A), some studies proved that spray mode of metal transfer, which is very similar to droplet impingement of GMAW, can be considered as a droplet impingement model [15, 18]. However, the metal transfer of the low current (I < 500 A) can be assumed as FWG metal transfer as shown in **Figure 5** [16].

- Slag heat source model

Cho et al. [15, 16, 18]. used a slag heat source model that considers the flux consumption rate, and they assumed that the distribution of the slag heat input to the material surface would be an elliptical ring as shown in **Figure 6**. The slag heat source model can be calculated from equation (12) to (14).

http://dx.doi.org/10.5772/intechopen.76725

$$\eta_s = \frac{\dot{m}_f C_{pf}\left(T_{m,flux} - T_0\right)}{VI} \tag{12}$$

$$r_e = \sqrt{(x - x_0)^2 \left(\frac{\sigma_y}{\sigma_x}\right)^2 + \left(y - y_0\right)^2} \tag{13}$$

$$\begin{aligned} &if\ R_a < r_e \leq R_b \text{ then,} \\ &q_s = \frac{\eta_s VI}{\pi\left(R_b^2 - R_a^2\right)}, \text{where } R_a = 3\sigma_q, R_b = R_a + 3.0mm \end{aligned} \tag{14}$$

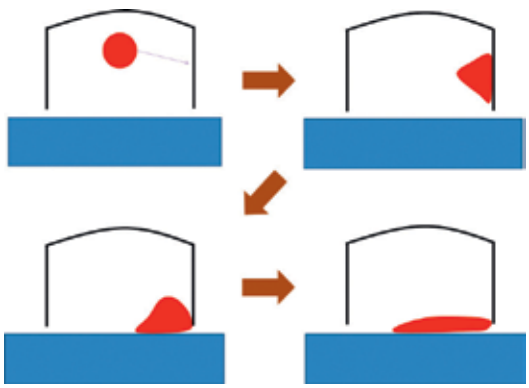

Figure 5. Schematic of droplet impingement on the wall to describe FWG transfer [16].

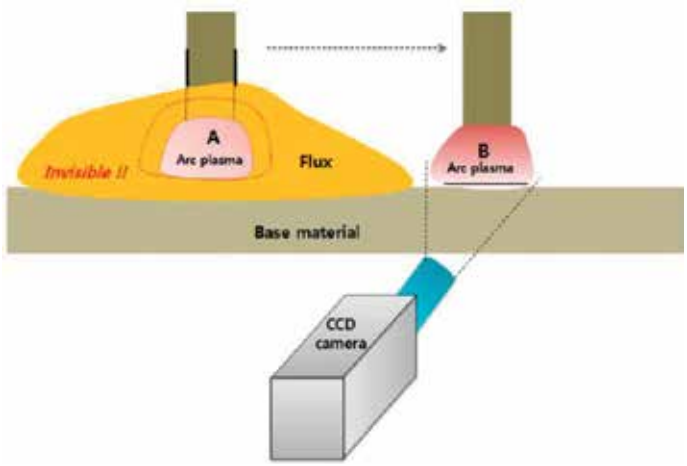

Figure 6. Process acquiring the arc plasma image [15].

- Arc heat source model

The actual arc plasma shape of SAW is very difficult to determine. Therefore, several studies assume some conditions to obtain the arc heat flux distributions [15].

a. The shape of the arc plasma inside the flux (A) is very similar to the arc plasma outside the flux (B) that just escaped (within 50 ms) as shown in **Figure 6**.

b. The metal vapor in the arc plasma root is neglected.

Therefore, it is reasonable to apply the elliptically symmetric Gaussian arc heat flux model in Eq. (15).

$$q_A(x,y) = \eta_A \frac{VI}{2\pi\sigma_x\sigma_y} \exp\left(-\frac{(x-x_1)^2}{2\sigma_x^2} - \frac{(y-y_1)^2}{2\sigma_y^2}\right) \tag{15}$$

- Arc pressure model

Due to the physical relationship, the effective radii of the arc heat flux and arc pressure are the same each other [10]. The resultant arc pressure model can be described in Eq. (16).

$$P_A(x,y) = \frac{\mu I^2}{4\pi^2\sigma_x\sigma_y} \exp\left(-\frac{(x-x_1)^2}{2\sigma_x^2} - \frac{(y-y_1)^2}{2\sigma_y^2}\right) \tag{16}$$

2.1.3. Electromagnetic force

In the arc welding process, Kou and Sun [26] found that the current density and self-induced magnetic field should be used to calculate the EMF in the molten pool. In the molten slag of a high current SAW process, however, Cho et al. [15, 16, 18] ignored the current flow effect in the molten slag because the magnitude of the current in the molten slag is tiny compared to the total current. Therefore, due to the physical relationship, the effective radius of electromagnetic force (EMF) model could be the same with that of the arc pressure and arc heat flux models [10]. For the elliptically symmetric distribution, EMF model can be calculated as follows:

$$k_1 = \frac{\sigma_y}{\sigma_x}, \quad (x-x_1)^2 + \frac{(y-y_1)^2}{k_1^2} = r_a^2 \tag{17}$$

$$J_z = \frac{I}{2\pi}\int_0^\infty \lambda J_0(\lambda r_a)\exp\left(-\lambda^2\sigma_r^2/4d_a\right)\frac{\sinh\left[\lambda(c-z)\right]}{\sinh\left(\lambda c\right)}d\lambda \tag{18}$$

$$J_r = \frac{I}{2\pi}\int_0^\infty \lambda J_1(\lambda r_a)\exp\left(-\lambda^2\sigma_r^2/4d\right)\frac{\cosh\left[\lambda(c-z)\right]}{\sinh\left(\lambda c\right)}d\lambda \tag{19}$$

$$B_\theta = \frac{\mu_m I}{2\pi}\int_0^\infty J_1(\lambda r_a)\exp\left(-\lambda^2\sigma_a^2/4d\right)\frac{\sinh\left[\lambda(c-z)\right]}{\sinh\left(\lambda c\right)}d\lambda \tag{20}$$

http://dx.doi.org/10.5772/intechopen.76725

$$F_x = -J_z B_\theta \frac{x}{r_a} \tag{21}$$

$$F_y = -J_z B_\theta \frac{y}{r_a} \tag{22}$$

$$F_z = J_z B_\theta. \tag{23}$$

2.1.4. Other models

The surface tension and buoyance force models are not affected by the arc plasma distribution [14]. The buoyancy force can be modeled by the Boussinesq approximation and then expressed in Eq. (24).

$$F_b = \rho g \beta (T - T_0) \tag{24}$$

A surface tension model that Sahoo et al. [27] developed for a binary Fe–S system is used to model the Marangoni flow. Thus, the surface tension can be expressed in Eq. (25)

$$\gamma(T) = \gamma_m^0 - A(T - T_m) - \overline{R}TT_s \ln\left(1 + k_1 a_i e^{-\Delta H^o/\overline{R}T}\right) \tag{25}$$

2.2. CFD modeling for multi-wire electrodes

For the better productivity, many industries applied two-wire or multi-electrode tandem SAW process. When the multi-wire electrodes are used, the arc shapes and the arc center positions are changed due to electromagnetic forces of arc plasma as shown in **Figure 7**.

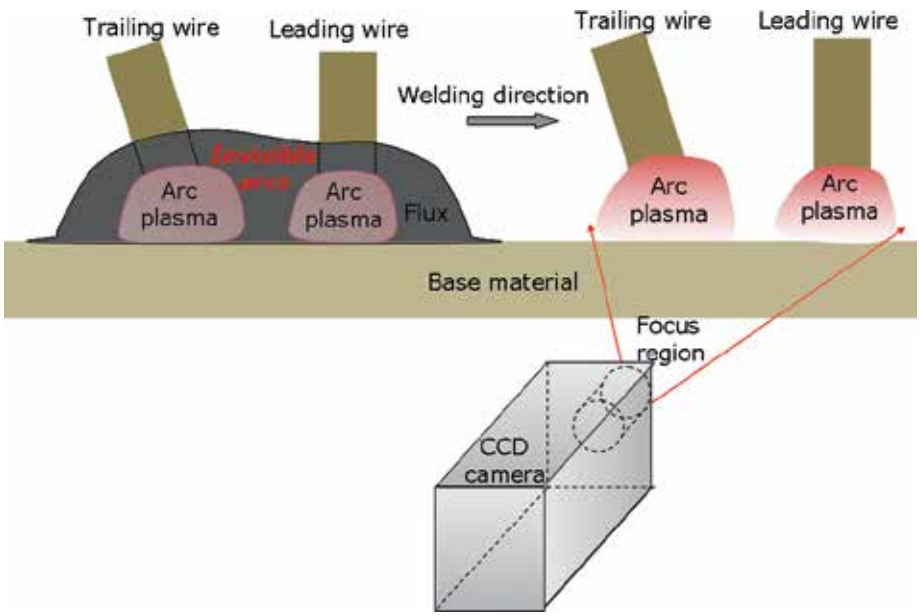

Figure 7. Schematic representation of the arc images acquisition method [17].

$$X_L = C_1\left(\frac{I_T}{I_L}\right)\left(\frac{l_L^2}{d}\right) \tag{26}$$

$$X_T = C_2\left(\frac{I_L}{I_T}\right)\left(\frac{l_T^2}{d}\right) \tag{27}$$

$$\sigma_{ij} = \beta_0^{ij} + \beta_1^{ij}I_j + \beta_2^{ij}V_j + \beta_3^{ij}X_j + \beta_4^{ij}I_j^2 + \beta_5^{ij}V_j^2 + \beta_6^{ij}X_j^2 + \beta_7^{ij}I_jV_j + \beta_8^{ij}V_jX_j + \beta_9^{ij}I_jX_j \tag{28}$$

2.2.1. Arc interaction model

Figure 7 illustrates the procedure followed to capture the arc images. The procedure to capture the arc images of multi-wire SAW process are very similar to single wire SAW process. Initially, the leading and trailing arcs are completely submerged under the granular flux, and a CCD camera starts to record side images of the arcs at a sampling rate of 1 kHz from the instant both the arcs come out of the flux. Kiran et al. [17, 21] considered the physical models for the arc center displacement and arc shape factors in two-wire and three wire tandem SAW process. From Eqs. (26) and (27), it is possible to expect that the higher current arc plasma is more stable than the lower current arc plasma. Additionally, the lower current arc plasma can be shifted more due to the arc interaction effect with AC welding signal. Kiran et al. [17] also proposed the effective radius of arc plasma model (27), where the welding current and voltage values are used.

2.2.2. Boundary conditions

The boundary conditions of single wire SAW from equation (6) to (8) are the same with that of multi-wire SAW process. However, two arc plasmas were used in the simulation so the arc heat source models, arc pressure, EMF models are different from those of the single wire model.

- Arc heat source model

As two arc plasmas were used in the simulations, two Gaussian asymmetric arc heat sources model, which contains different temperature distributions for the front and rear part in Eqs. (29) and (30). Therefore, Cho et al. [18] adopted the resultant effective radius to describe the Gaussian asymmetric arc models with DC and AC welding signals.

$$\begin{aligned} &\text{if } x \le x_0 \text{ then, } q_{aL}(x,y) = \frac{\eta_a V_L I_L}{2\pi\sigma_{AL}^2}\exp\left(-\frac{(x-x_0)^2}{2\sigma_{RL}^2} - \frac{y^2}{2\sigma_{AL}^2}\right) \\ &\text{if } x > x_0 \text{ then, } q_{aL}(x,y) = \frac{\eta_a V_L I_L}{2\pi\sigma_{AL}^2}\exp\left(-\frac{(x-x_0)^2}{2\sigma_{FL}^2} - \frac{y^2}{2\sigma_{AL}^2}\right) \end{aligned} \tag{29}$$

$$\begin{aligned} &\text{if } x \le x_1 \text{ then, } q_{aT}(x,y) = \frac{\eta_a V_T I_T}{2\pi\sigma_{AT}^2}\exp\left(-\frac{(x-x_0)^2}{2\sigma_{RT}^2} - \frac{y^2}{2\sigma_{AT}^2}\right) \\ &\text{if } x > x_1 \text{ then, } q_{aT}(x,y) = \frac{\eta_a V_T I_T}{2\pi\sigma_{AT}^2}\exp\left(-\frac{(x-x_0)^2}{2\sigma_{FT}^2} - \frac{y^2}{2\sigma_{AT}^2}\right) \end{aligned} \tag{30}$$

- Arc pressure model

The distribution of arc pressure model is the same with that of arc heat source model [10]; therefore, arc pressure model can be derived in equation (31) and (32).

$$\begin{aligned} &\text{if } x \le x_0 \text{ then, } P_{aL}(x,y) = \frac{\mu_0 I_L^2}{4\pi^2 \sigma_{AL}^2} \exp\left(-\frac{(x-x_0)^2}{2\sigma_{RL}^2} - \frac{y^2}{2\sigma_{AL}^2}\right) \\ &\text{if } x > x_0 \text{ then, } P_{aL}(x,y) = \frac{\mu_0 I_L^2}{4\pi^2 \sigma_{AL}^2} \exp\left(-\frac{(x-x_0)^2}{2\sigma_{FL}^2} - \frac{y^2}{2\sigma_{AL}^2}\right) \end{aligned} \tag{31}$$

$$\begin{aligned} &\text{if } x \le x_1 \text{ then, } P_{aT}(x,y) = \frac{\mu_0 I_T^2}{4\pi^2 \sigma_{AT}^2} \exp\left(-\frac{(x-x_0)^2}{2\sigma_{RT}^2} - \frac{y^2}{2\sigma_{AT}^2}\right) \\ &\text{if } x > x_1 \text{ then, } P_{aT}(x,y) = \frac{\mu_0 I_T^2}{4\pi^2 \sigma_{AT}^2} \exp\left(-\frac{(x-x_0)^2}{2\sigma_{FT}^2} - \frac{y^2}{2\sigma_{AT}^2}\right) \end{aligned} \tag{32}$$

- Slag heat source model

Slag heat source model in the two-wire SAW process are the same as that of single wire SAW process.

- Droplet model

Kiran et al. [17] found that the molten droplet is directed to the arc center when it is just detached. Moreover, the direction of the droplet could not be changed during the free flight. Cho et al. [18] consider that physical phenomena and then applied to the numerical simulation as shown in **Figures 8** and **9**.

The droplet efficiency relies on the wire feed rate and it is possible to be calculated using equation (9) to (11). The droplet efficiency can be varied from the wire feed rate and welding signals [15, 16, 18, 21].

2.2.3. EMF model

EMF can be induced from the two different arc plasmas; therefore EMF model used in the two-wire SAW process can be followed [18]:

$$J_{zL} = \frac{I}{2\pi} \int_0^\infty \lambda J_0(\lambda r_a) \exp\left(-\lambda^2 \sigma_{AL}^2 / 4 d_a\right) \frac{\sinh\left[\lambda(c-z)\right]}{\sinh\left(\lambda c\right)} d\lambda \tag{33}$$

$$J_{rL} = \frac{I}{2\pi} \int_0^\infty \lambda J_1(\lambda r_a) \exp\left(-\lambda^2 \sigma_{AL}^2 / 4 d_a\right) \frac{\cosh\left[\lambda(c-z)\right]}{\sinh\left(\lambda c\right)} d\lambda \tag{34}$$

$$B_{\theta L} = \frac{\mu_m I_L}{2\pi} \int_0^\infty J_1(\lambda r_a) \exp\left(-\lambda^2 \sigma_{AL}^2 / 4 d_a\right) \frac{\sinh\left[\lambda(c-z)\right]}{\sinh\left(\lambda c\right)} d\lambda \tag{35}$$

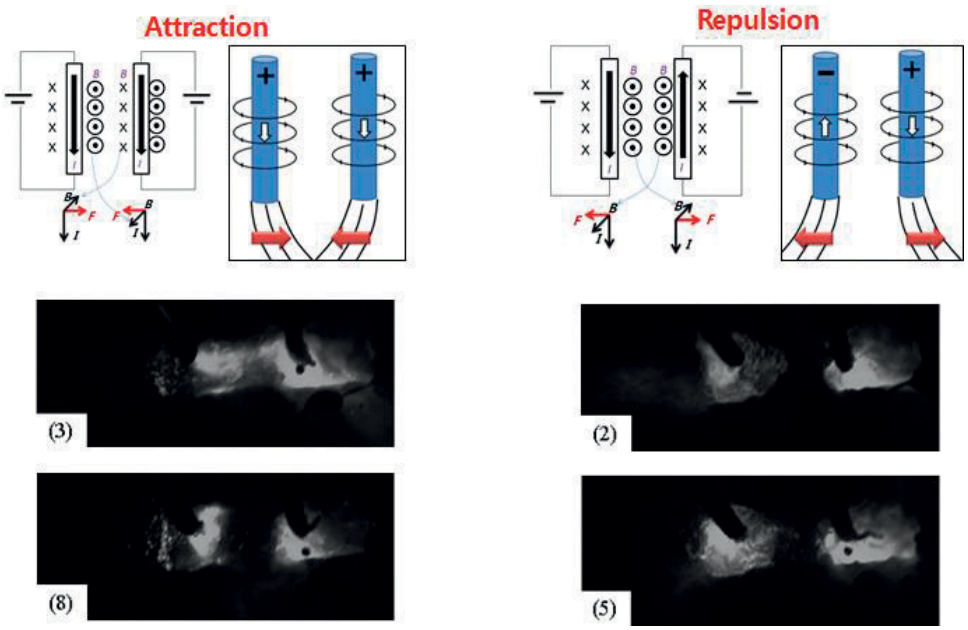

Figure 8. Arc interaction effect of the two wire tandem SAW [17, 28].

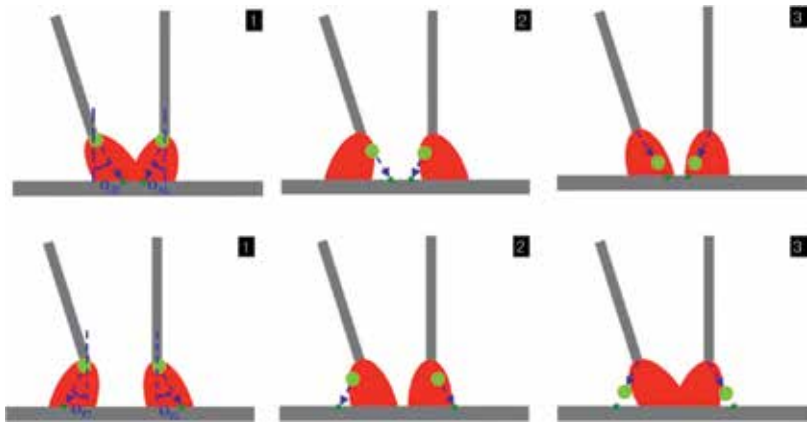

Figure 9. Droplet flights due to the arc interaction effect in two wire SAW process [18].

$$F_{rL} = J_{zL} B_{\theta L} \tag{36}$$

$$F_{zL} = J_{rL} B_{\theta L} \tag{37}$$

$$J_{zT} = \frac{I}{2\pi} \int_0^\infty \lambda J_0(\lambda r_a) \exp\left(-\lambda^2 \sigma_{AT}^2 / 4 d_a\right) \frac{\sinh\left[\lambda(c-z)\right]}{\sinh\left(\lambda c\right)} d\lambda \tag{38}$$

$$J_{rT} = \frac{I}{2\pi}\int_0^\infty \lambda J_1(\lambda r_a)\exp\left(-\lambda^2\sigma_{AT}^2/4d_a\right)\frac{\cosh\left[\lambda(c-z)\right]}{\sinh\left(\lambda c\right)}d\lambda \tag{39}$$

$$B_{\theta T} = \frac{\mu_m I_T}{2\pi}\int_0^\infty J_1(\lambda r_a)\exp\left(-\lambda^2\sigma_{AT}^2/4d_a\right)\frac{\sinh\left[\lambda(c-z)\right]}{\sinh\left(\lambda c\right)}d\lambda \tag{40}$$

$$F_{rT} = J_{zT}B_{\theta T} \tag{41}$$

$$F_{zT} = J_{rT}B_{\theta T} \tag{42}$$

2.2.4. Other models

The same surface tension and buoyance force models in equation (24) and (25) are applied.

3. Simulation results for SAW process

3.1. Single wire SAW process

3.1.1. Spray mode of metal transfer

- Single DC

Cho et al. [15] simulated the molten pool behaviors for single DC SAW process which compared the molten pool behaviors for different electrode angles as shown in **Figure 10**. They found that electrode angle plays on important role to form the bead shapes such as penetration and bead width.

When the negative electrode angle is applied, the penetration of weld bead increases deeper because the droplet impingement direction is very similar to the molten poo circulation. Thus the momentum can be transferred sufficiently to the weld pool. Specifically, the molten pool flows downward and backward in the dotted box between droplet generations (**Figure 11(a)** and **(b)**) and then forms a sharp and deep penetration on a transverse cross-section by convection heat transfer as shown in **Figure 12(a)**. However, the positive electrode angle induces

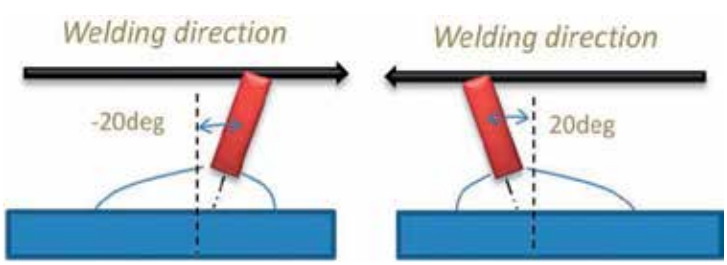

Figure 10. Electrode angle used in the simulation [28].

somewhat different flow patterns because the droplet impingement direction does not match the molten pool direction as shown in **Figure 13(a)** and **(b)**. Therefore, less momentum from the droplet impingement can be transferred in positive electrode angle compared to negative electrode angle.

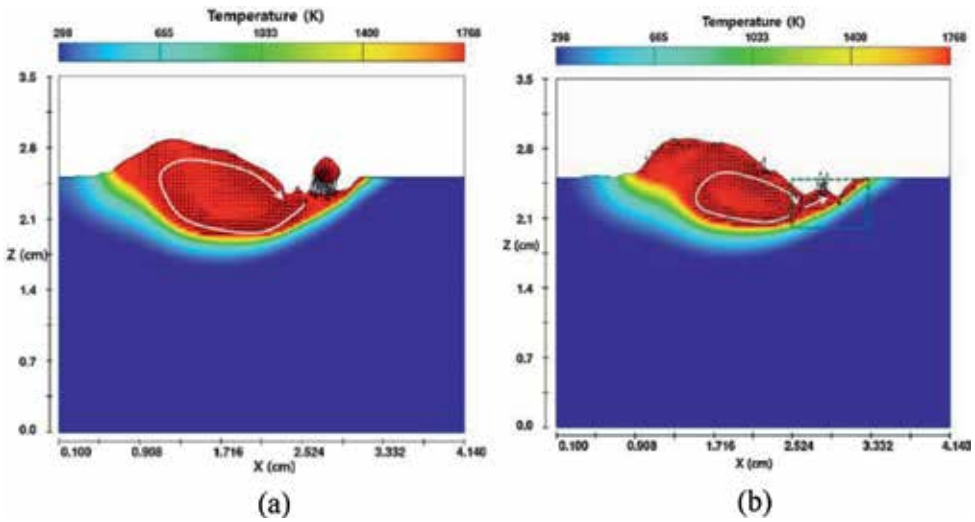

Figure 11. Calculated temperature profiles and flow patterns on a longitudinal cross section for negative electrode angle (−20° C) [15] (a) 0.528 s (b) 0.538 s.

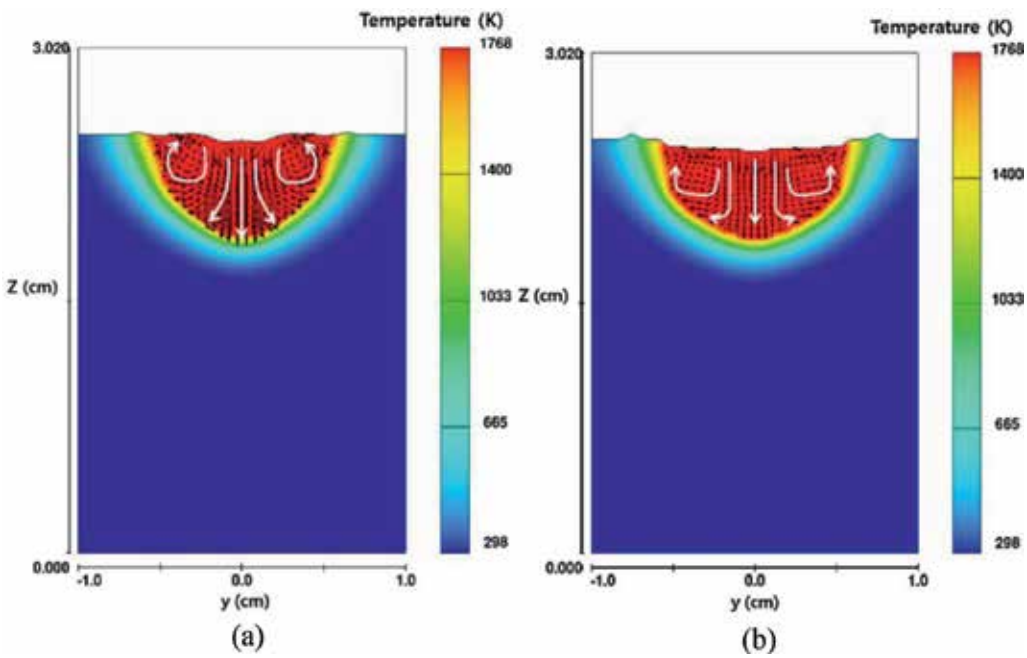

Figure 12. Calculated temperature profiles and flow patterns on a transverse cross section at 0.598 s for negative and positive electrode angle [15] (a) negative angle (−20°) (b) positive angle (+20°).

http://dx.doi.org/10.5772/intechopen.76725

AC welding signals can bring the different simulation results. Cho et al. [15] simulated the molten pool simulation with sinusoidal AC waveform with a negative electrode angle. As the arc shape and signals vary with the welding time, it could induce more dynamic molten pool flows than DC welding. Normally, the frequency of droplet impingement and welding signals cannot be the same so the molten pool under the arc flows forward and backward repeatedly with a welding time as shown in **Figure 14**.

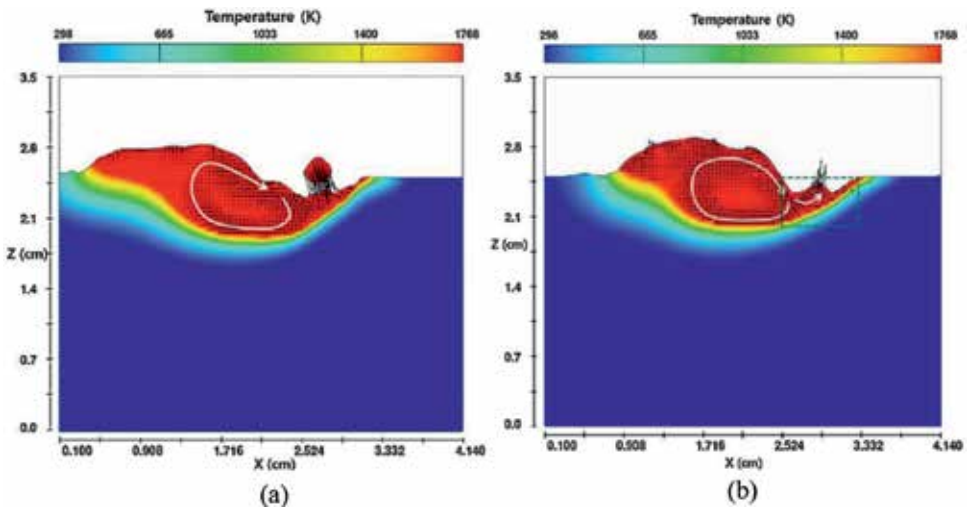

Figure 13. Calculated temperature profiles and flow patterns on a longitudinal cross section for positive electrode angle (+20°C) [15] (a) 0.528 s (b) 0.538 s.

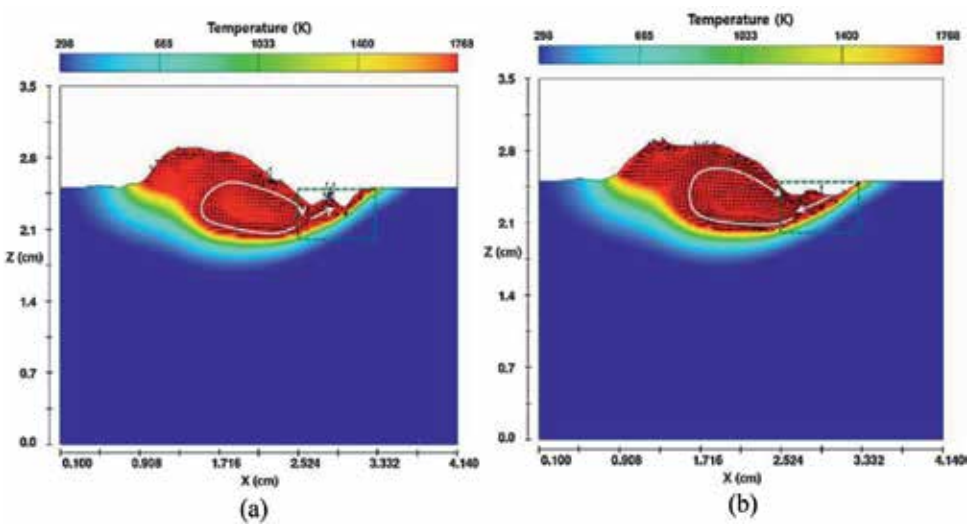

Figure 14. Calculated temperature profiles and flow patterns on a longitudinal cross section for sinusoidal AC waveform (current, voltage) with a negative electrode angle [15] (a) 0.528 s (b) 0.538 s.

When the welding current value is not enough to form the spray metal transfer, it is possible to expect FWG metal transfer mode. Cho et al. [16] simulated the molten pool behavior of FWG metal transfer in V-groove SAW process. The molten droplet impinges to the inner wall boundary and then moves to the V-groove joint sequentially as shown in **Figure 15**. The V-groove joint hardly melts because the arc heat and arc forces (arc pressure & EMF) are not focused on the V-groove joint and. Therefore, it is expected that the inclined side surface melts while the molten pool behavior induces the void in the V-groove joint.

3.2. Multi-wire SAW process

3.2.1. Two wire tandem SAW

Kiran et al. [17] found that when the absolute current value was higher, the arc stiffness increased; thus, the arc tended to be fixed. However, when the absolute current value of the opposite electrode is higher, the arc stiffness decreases, so the arc tends to move backward or forward by the Lorentz force. Finally, the combination of current values from each electrode affects the arc center locations and droplet free flights [18]. For instance, the higher absolute current value can result in an increase in the wire feed rate, which can induce a frequent droplet impingement and a concentration of the arc heat and arc forces.

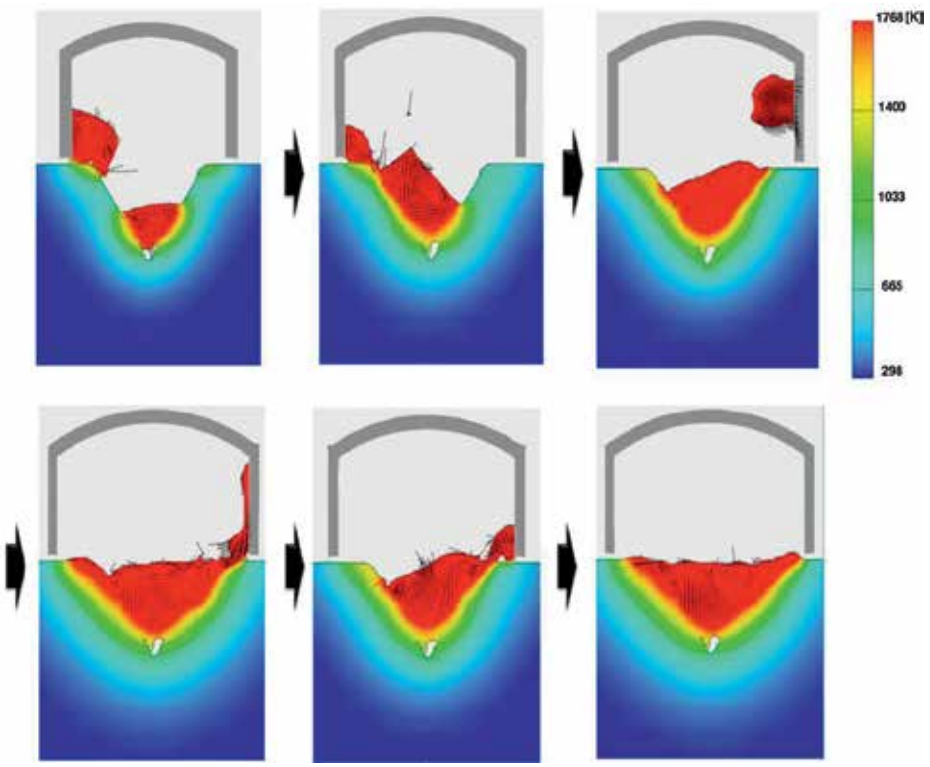

Figure 15. Temperature profiles and flow distributions on the transverse cross section in FWG mode [16].

http://dx.doi.org/10.5772/intechopen.76725

Using this principle, Cho et al. [18] performed CFD simulations and analyzed the results. For higher current in the leading electrode, the arc center displacement of the leading electrode is very small; moreover, the arc heat, arc force and droplet impingement can be focused under the leading electrode. Therefore, the volume of the molten pool ahead of the leading electrode is very small because droplets do not fly ahead of the leading electrode as shown in **Figure 16(a)**.

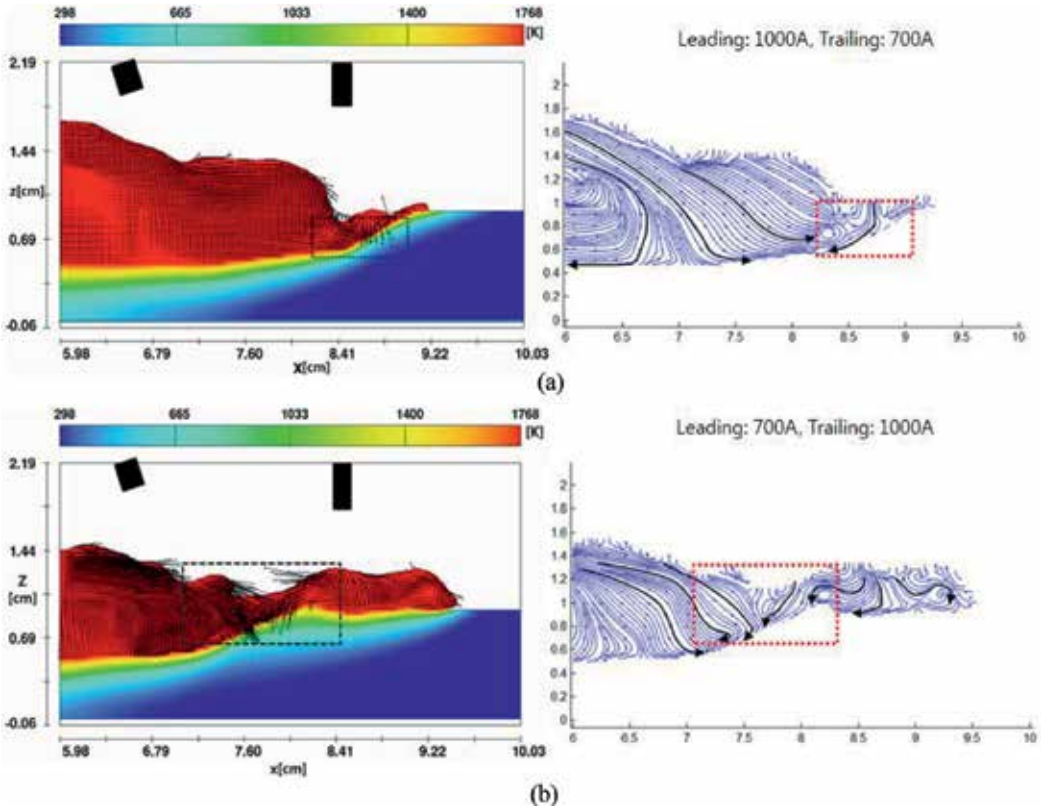

Figure 16. Temperature profiles and streamlines on the longitudinal cross section for two wire tandem SAW process [18] (a) higher current in the leading electrode (b) higher current in the trailing electrode.

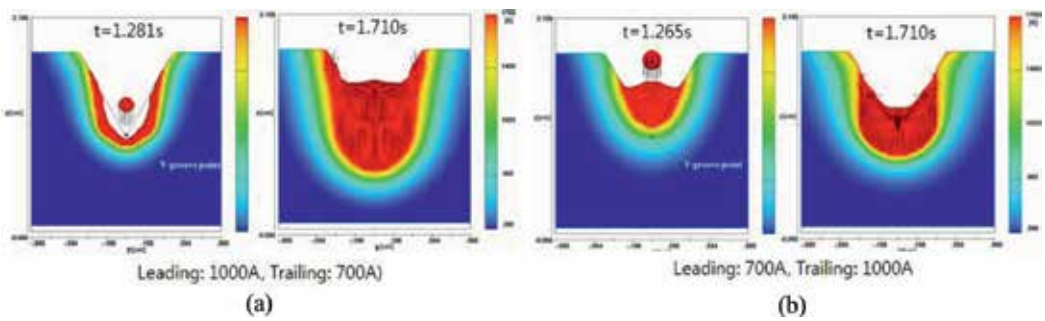

Figure 17. Temperature profiles and streamlines on the transverse cross section for two wire tandem SAW process [18] (a) higher current in the leading electrode (b) higher current in the trailing electrode.

In the transverse section, droplets from the leading electrode impinged on the weld pool whose height is lower than the initial V-grove point; therefore, deep penetration can be from as shown in **Figure 17(a)**. Moreover, the weld pool flows long after droplet impingement in the longitudinal section so this can be another reason to make the deep penetration due to the dynamic convection heat transfer. On the contrary, when the higher current welding signal in the trailing electrode is applied, the arc center displacement of the leading electrode due to the arc

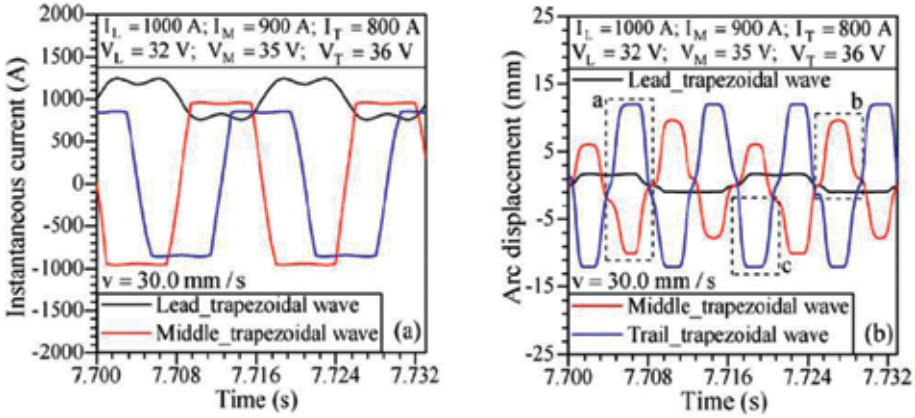

Figure 18. Current waveforms and the corresponding arc center displacement for three wire tandem SAW process [21].

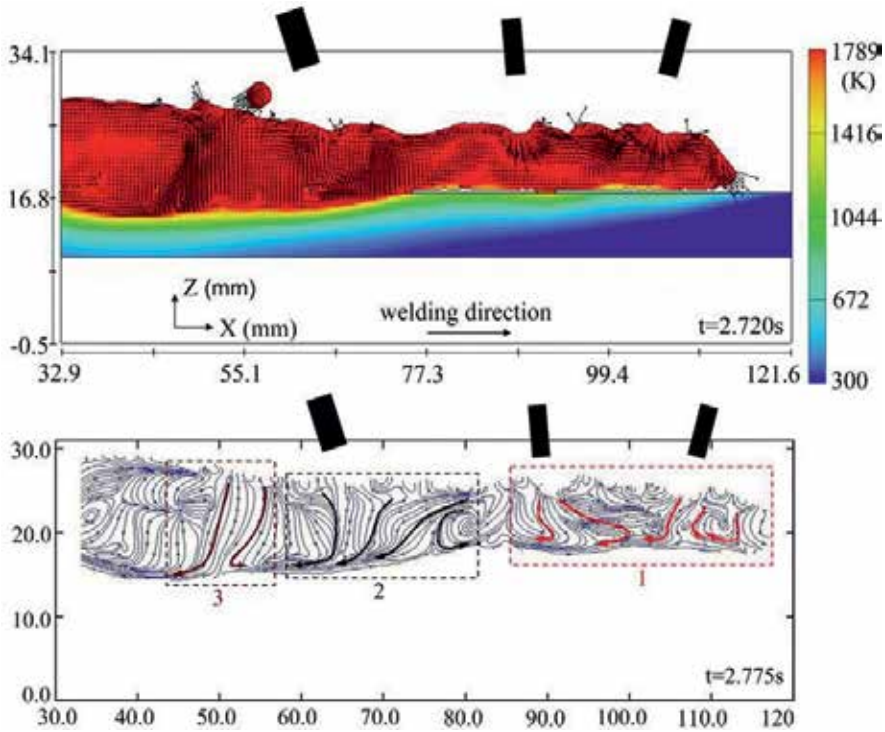

Figure 19. Temperature profiles and streamlines on the longitudinal cross section for three wire tandem SAW process [21].

http://dx.doi.org/10.5772/intechopen.76725

interaction is much bigger than that of the trailing electrode. Therefore, the droplets, arc heat and arc forces from the leading electrode cannot be focused on a similar weld pool spot, but the droplets disperse forward or backward of the welding direction and the form the volume of the molten pool ahead of the leading electrode as shown in **Figure 16(b)**. With these fluid behaviors, the molten pool can fill in the V-groove point; therefore, the molten pool penetrates to a lesser degree than in the higher current in the leading electrode (**Figure 17(b)**).

3.2.2. Three wire tandem SAW

Kiran et al. [21] modeled and simulated the molten pool flow behavior for three wire tandem SAW in V-groove. They firstly measured welding signals and the arc interaction position of three wire SAW process as shown in **Figure 18** and they found that the molten pool behavior from the arc interaction played an important role to increase the penetration of V-groove. It is evident that the middle and trailing arcs are closely concentrated during the attraction (dotted box 'a') compared to that of the same between leading and middle arcs (dotted box 'b'). When the distances of middle and trailing arcs are short (dotted box 'a'), the focused arc heat and arc forces activate the molten pool behavior more dynamic and these increase penetration in the

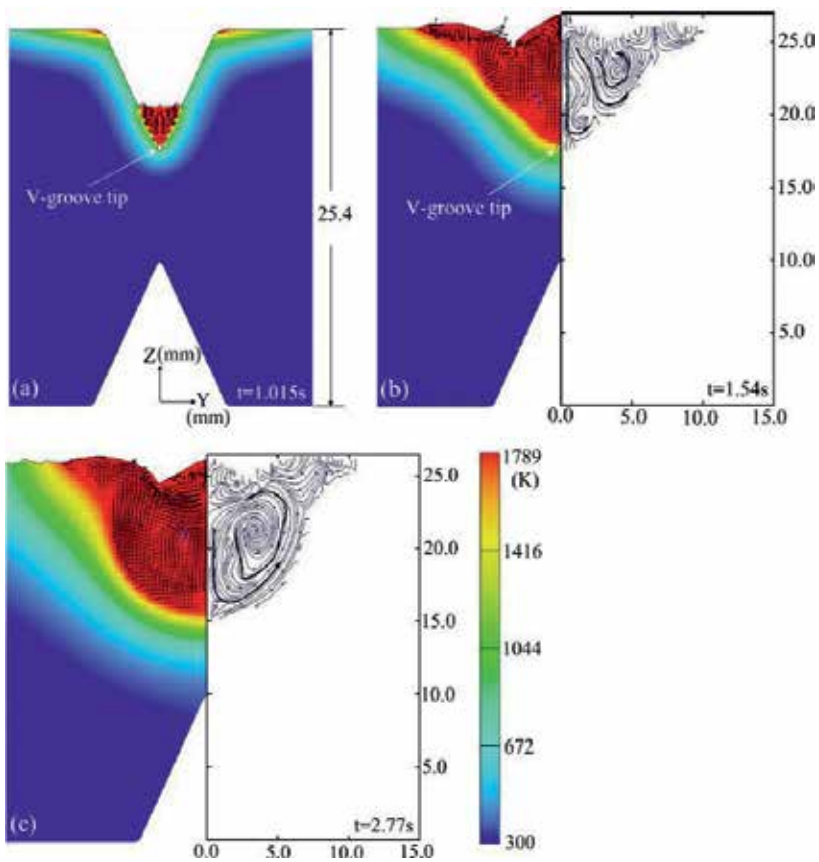

Figure 20. Temperature profiles and streamlines on the transverse cross section for three wire tandem SAW process [21].

longitudinal cross section as shown in **Figure 19**. The molten pool flow patterns in the transverse section are also described in **Figure 20**.

Acknowledgements

The authors gratefully acknowledge the support from Korea Ministry of Trade, Industry and Energy (No.10076430).

Author details

Dae-Won Cho

Address all correspondence to: chodaewon@gmail.com

Busan Machinery Research Center, Korea Institute of Machinery and Materials,
Republic of Korea

References

[1] Wen SW, Hilton P, Farrugia DCJ. Finite element modelling of a submerged arc welding process. Journal of Materials Processing Technology. 2001;**119**(1–3):203-209

[2] Sharma A, Chaudhary AK, Arora N, Mishra BK. Estimation of heat source model parameters for twin-wire submerged arc welding. The International Journal of Advanced Manufacturing Technology. 2009;**45**(11–12):1096

[3] Mahapatra MM, Datta GL, Pradhan B, Mandal NR. Three-dimensional finite element analysis to predict the effects of SAW process parameters on temperature distribution and angular distortions in single-pass butt joints with top and bottom reinforcements. International Journal of Pressure Vessels and Piping. 2006;**83**(10):721-729

[4] Kiran DV, Basu B, Shah AK, Mishra S, De A. Three-dimensional heat transfer analysis of two wire tandem submerged arc welding. ISIJ International. 2011;**51**(5):793-798

[5] Kim JW, Na SJ. A study on the three-dimensional analysis of heat and fluid flow in gas metal arc welding using boundary-fitted coordinates. Journal of Engineering for industry. 1994;**116**(1):78-85

[6] Kim CH, Zhang W, DebRoy T. Modeling of temperature field and solidified surface profile during gas–metal arc fillet welding. Journal of Applied Physics. 2003;**94**(4):2667-2679

[7] Kim WH, Fan HG, Na SJ. Effect of various driving forces on heat and mass transfer in arc welding. Numerical Heat Transfer, Part A Applications. 1997;**32**(6):633-652

[8] Cho DW, Na SJ, Cho MH, Lee JS. Simulations of weld pool dynamics in V-groove GTA and GMA welding. Welding in the World. 2013;**57**(2):223-233

[9] Cho DW, Na SJ, Cho MH, Lee JS. A study on V-groove GMAW for various welding positions. Journal of Materials Processing Technology. 2013;**213**(9):1640-1652

[10] Cho DW, Lee SH, Na SJ. Characterization of welding arc and weld pool formation in vacuum gas hollow tungsten arc welding. Journal of Materials Processing Technology. 2013;**213**(2):143-152

[11] Cho JH, Na SJ. Implementation of real-time multiple reflection and Fresnel absorption of laser beam in keyhole. Journal of Physics D: Applied Physics. 2006;**39**(24):5372

[12] Cho JH, Na SJ. Three-dimensional analysis of molten pool in GMA-laser hybrid welding. Welding Journal. 2009;**88**(2):35-43

[13] Han SW, Cho WI, Na SJ, Kim CH. Influence of driving forces on weld pool dynamics in GTA and laser welding. Welding in the World. 2013;**57**(2):257-264

[14] Cho WI, Na SJ, Cho MH, Lee JS. Numerical study of alloying element distribution in CO2 laser–GMA hybrid welding. Computational Materials Science. 2010;**49**(4):792-800

[15] Cho DW, Song WH, Cho MH, Na SJ. Analysis of submerged arc welding process by three-dimensional computational fluid dynamics simulations. Journal of Materials Processing Technology. 2013;**213**(12):2278-2291

[16] Cho DW, Kiran DV, Na SJ. Analysis of molten pool behavior by flux-wall guided metal transfer in low-current submerged arc welding process. International Journal of Heat and Mass Transfer. 2017;**110**:104-112

[17] Kiran DV, Cho DW, Song WH, Na SJ. Arc behavior in two wire tandem submerged arc welding. Journal of Materials Processing Technology. 2014;**214**(8):1546-1556

[18] Cho DW, Kiran DV, Song WH, Na SJ. Molten pool behavior in the tandem submerged arc welding process. Journal of Materials Processing Technology. 2014;**214**(11):2233-2247

[19] Kiran DV, Cho DW, Lee HK, Kang CY, Na SJ. A study on the quality of two-wire tandem submerged arc welds under iso-heat input conditions. The International Journal of Advanced Manufacturing Technology. 2015;**78**(1–4):53-62

[20] Cho DW, Kiran DV, Na SJ. Analysis of the flux consumption and metal transfer for tandem submerged arc welding process under iso-heat input condition. Welding Journal. 2015;**94**: 396-401

[21] Kiran DV, Cho DW, Song WH, Na SJ. Arc interaction and molten pool behavior in the three wire submerged arc welding process. International Journal of Heat and Mass Transfer. 2015;**87**:327-340

[22] Franz U. Vorgange in der Kaverne beim UP-Schweissen Teil I. Schweiss Tech. 1965;**15**:145-150

[23] Van Adrichem JT. Metal transfer in submerged arc welding. International Institute of Welding Document. 1966:212-278

[24] Chandel RS. The effect of process variables on the flux consumption in submerged arc welding. Material and Manufacturing Process. 1998;**13**(2):181-188

[25] Renwick BG, Patchett BM. Operating characteristics of the submerged arc process. Welding Journal. 1976;**55**(3):69

[26] Kou S, Sun DK. Fluid flow and weld penetration in stationary arc welds. Metallurgical Transactions A. 1985;**16**(1):203-213

[27] Sahoo P, DebRoy T, McNallan MJ. Surface tension of binary metal—Surface active solute systems under conditions relevant to welding metallurgy. Metallurgical Transactions B. 1988;**19**(3):483-491

[28] Cho DW. A Study on Molten Pool Flow Behavior in Pipe Seam Welding and Girth Welding Processes by Computational Fluid Dynamics. Kaist Ph. D [Thesis] 2014

Chapter 2

Direct Numerical Simulation of Hydrate Dissociation in Homogeneous Porous Media by Applying CFD Method: One Example of CO_2 Hydrate

Wu-Yang Sean

Additional information is available at the end of the chapter

http://dx.doi.org/10.5772/intechopen.74874

Abstract

Computational fluid method (CFD) is popular in either large-scale or meso-scale simulations. One example is to establish a new pore-scale (m~μm) model of laboratory-scale sediment samples for estimating the dissociation rate of synthesized CO_2 hydrate (CO_2H) reported by Jeong. It is assumed that CO_2H formed homogeneously in spherical pellets. In the bulk flow, concentration and temperature of liquid CO_2 in water flow was analyzed by CFD method under high-pressure state. Finite volume method (FVM) were applied in a face-centered packing in unstructured mesh. At the surface of hydrate, a dissociation model has been employed. Surface mass and heat transfer between hydrate and water are both visualized. The initial temperature 253.15K of CO_2H pellets dissociated due to ambient warm water flow of 276.15 and 282.15K and fugacity variation, ex. 2.01 and 1.23 MPa. Three tentative cases with porosity 74, 66, and 49% are individually simulated in this study. In the calculation, periodic conditions are imposed at each surface of packing. Numerical results of this work show good agreement with Nihous' model. Kinetic modeling by using 3D unstructured mesh and CFD scheme seems a simple tool, and could be easily extended to determine complex phenomena coupled with momentum, mass and heat transfer in the sediment samples.

Keywords: heat and mass transfer, finite volume method (FVM), computational fluid dynamics (CFD), pore-scale flow

1. Introduction

Computational fluid method (CFD) is popular in either large-scale or meso-scale simulations. One example is to establish a new pore-scale (m~μm) model of laboratory-scale sediment

samples for estimating the dissociation rate of synthesized CO_2 hydrate (CO_2H) reported by [1]. To decrease the CO_2 concentration in the air, carbon dioxide capture and storage (CCS) is regarded to be an effective way. One concept of CCS is to store CO_2 in gas hydrate in sub-seabed geological formation, as was illustrated by [6]. Besides, many studies about the formation and dissociation of CO_2 hydrate (CO_2H) while stored in the deep ocean or geologic sediment have been introduced. In particular, flow and transport in sediment is multidisciplinary science including the recovery of oil, groundwater hydrology and CO_2 sequestration. It reported the measurements of the dissociation rate of well-characterized, laboratory-synthesized carbon dioxide hydrates in an open-ocean seafloor [5]. The pore effect in the phase equilibrium mainly due to the water activity change was discussed in [7]. The reactive transport at the pore-scale to estimate realistic reaction rates in natural sediments was discussed in [3]. This result can be used to inform continuum scale models and analyze the processes that lead to rate discrepancies in field applications. Pore-scale model is applied to examine engineered fluids [4]. Unstructured mesh is well suited to pore-scale modeling because of adaptive sizing of target unit with high mesh resolution and the ability to handle complicated geometries [17, 18]. Particularly, it can easily be coupled with computational fluid dynamics (CFD) methods, such as finite volume method (FVM) or finite element method (FEM). Unstructured tetrahedral mesh used to define the pore structure is discussed in [19]. Another case includes a numerical simulation of laminar flow based on FVM with unstructured meshes was used to solve the incompressible, steady Navier-Stokes equations through a cluster of metal idealized pores by [20].

The objective of this work is to develop a new pore-scale model for estimating the dissociation rate of CO_2H in homogeneous porous media. To cooperate with molecular simulation and field-scale simulators, we aim at establishing pore-scale modeling to analyze the simultaneous kinetic process of CO_2H dissociation due to non-equilibrium states. Major assumptions in this study are listed as below:

1. Only dissociation occurred at the surface, no any formation occurred immediately with dissociation.
2. CO_2 dissociated at the surface is assumed to be dissolved into liquid water totally without considering the gas nucleated.
3. The surface structure does not collapse with the dissociation of CO_2H at the surface of pellets.
4. Homogeneous face-centered packing of multi-CO_2H pellets.
5. Single phase flow coupled with mass, heat, and momentum transfers.

2. Dissociation modeling at the surface

In this study, the dissociation flux (F_1) is assumed to be proportional to the driving force, the free energy difference ($\Delta\mu$) introduced by [6], presented as

$$F_1 = k_{\mathrm{bl}}\mathrm{RTln}\left(\frac{C_{Hsol}}{C_I}\right) \tag{1}$$

where k_{bl} is the rate constant $\left[\text{mol}^2\ \text{J}^{-1}\ \text{s}^{-1}\text{m}^{-2}\right]$ of dissociation. According to [21], k_{bl} is listed as below:

$$k_{bl} = \exp\left(-\frac{11,729}{T} + 26.398\right) \tag{2}$$

where C_{Hsol} is the mole fraction of CO_2 in the aqueous solution at equilibrium state with hydrate, and C_I means surface concentration in the ambient aqueous solution at the surface of the hydrate C_I.

3. Basic transport equations

Flow in the porous media around CO_2H is governed by the continuity and the Navier-Stoke's equations. The advection-diffusion equations of non-conservative type for mass concentration C and temperature T are also considered.

$$\nabla \cdot \mathbf{u} = 0 \tag{3}$$

$$\frac{\partial \mathbf{u}}{\partial t} + \nabla \cdot (\mathbf{uu}) = -\nabla P + \frac{1}{\text{Re}} \nabla \cdot \left[\nabla \mathbf{u} + (\nabla \mathbf{u})^T\right] + \frac{\rho_w}{\text{Fn}^2} g \tag{4}$$

No.	Function	Definition
1	$D = 7.4 \times 10^{-12} \frac{(\varphi M_B)^{1/2} T}{\eta_L V_A^{0.6}}$	D: diffusion coefficient of CO_2 in water φ(=2.6): association parameter for the solvent water $M_B\left(= 18\ \text{gmol}^{-1}\right)$: molecular weight of water $V_A\left(= 3.4 \times 10^{-5}\ \text{m}^3\text{mol}^{-1}\right)$: molar volume of CO_2 η_L[mPa·s]: viscosity of water
2	$\nu_L = \left(8.8286 \times 10^{-10}\right)T^2 - \left(5.3886 \times 10^{-7}\right)T + 8.314 \times 10^{-5}$	$\nu_L\left[\text{ms}^{-2}\right]$: kinematic viscosity
3	$\lambda_L = 487.85\ln(T) - 2173.8$	$\lambda_L\left[\text{WKm}^{-1}\right]$: heat conductivity of water
4	$\alpha_L = \frac{\lambda_L}{\rho_W C_p}$	$\alpha_L\left[\text{ms}^{-2}\right]$: the thermal diffusivity of aqueous phase $\rho_W\left(= 997.1 \frac{\text{kg}}{\text{m}^3}\right)$: density of water $C_p\left(= 4,180 \frac{\text{J}}{\text{kg}} \cdot \text{K}\right)$: isobaric specific heat, quoted from "Chemical Engineering Handbook", Japan (1985)
5	$P_{eq} = \exp\left(\alpha + \frac{\beta}{T}\right) \times 10^3$	α=44.580 and β = − 10246.28
6	$C_{Hsol} = a \cdot \exp\left(b \cdot P \times 10^{-6} + 1.321 \times 10^{-4} T - 2.292 \times 10^{-2}\right) \cdot 1.8 \times 10^{-5}$	$C_{Hsol}\left[\text{mole}\cdot\text{m}^{-3}\right]$: solubility of hydrate (275.15 K < T < 281.15 K) $a = 0.0016(T - 273.15)^{0.9211}$ $b = -0.0199\log(T - 273.15) + 0.0942$ by Aya et al. [10], Yang et al. [11], and Servio and Englezos [12]

Table 1. Parameters used in this study.

$$\frac{\partial C}{\partial t} + \mathbf{u} \cdot \nabla C = \frac{1}{\mathrm{ReSc}} \nabla^2 C \tag{5}$$

$$\frac{\partial T}{\partial t} + \mathbf{u} \cdot \nabla T = \frac{1}{\mathrm{RePr}} \nabla^2 T \tag{6}$$

where the viscosity, diffusivity, and thermal conductivity of pure water are included in dimensionless parameters such as the Reynolds number, the Schmit number, and the Prandtl number, which are interpolated as functions of temperature and are updated at every computational time step as summarized in **Table 1**. U and d (=0.001 m) are the velocity of inflow and diameter of hydrate pellet.

4. Mass transfer

To rewrite Eq. (1), the flux at the surface of the hydrate can be discretized as

$$k_{bl} R T \ln\left(\frac{C_{Hsol}}{C_I}\right) = D \nabla C = D \frac{C_I - C'}{h_I} \tag{7}$$

where C_I is the varying surface concentration calculated locally at each surface cell, C' is the centroid concentration, and h_I is the thickness of centroid surface cell, as shown in **Figure 1**.

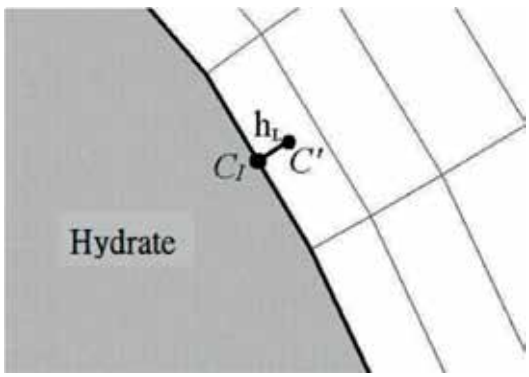

Figure 1. Schematic image of discretized surface concentration.

5. Heat transfer

The equation of energy balance at the surface of CO_2H is given by

$$\dot{Q}_H + \lambda_H \nabla T_H = \lambda_L \nabla T_L \tag{8}$$

where $\dot{Q}_H$ (= $H_L F_1$, where H_L is the latent heat of hydrate dissociation) is the dissociation heat transferred to the CO_2H, λ_H is the thermal conductivity of hydrate. Dissociation heat per mole of hydrate, H_L, is interpolated from [2] as

$$H_L = 207,917 - 530.97 \times T_I \tag{9}$$

where T_I is the surface temperature. Then, we have

$$T_I = \frac{\lambda_L h_H T_L + \lambda_H h_L T_H - 207,917 \cdot F_{cal} h_L h_H}{\lambda_L h_H + \lambda_H h_L - 530.97 \cdot F_{cal} h_L h_H} \tag{10}$$

where T_L and T_H are the temperatures defined at the centroids cell in the aqueous phase and solid hydrate, respectively; h_L and h_H are half widths of centroid in the aqueous phase and solid hydrate, respectively. Besides, the temperature in the pellet is calculated by using the heat conductivity equation.

$$\frac{\partial T}{\partial t} = \alpha_H \frac{\partial^2 T}{\partial x^2} \tag{11}$$

where $\alpha_H = \frac{\lambda_H}{\rho_H C_p'}$ is the thermal diffusivity of CO_2H. These relative properties of CO_2H are quoted from [9], the thermal diffusivity of aqueous phase (α_H) of $1.38 \times 10^{-7} ms^{-2}$, the heat capacity of hydrate (C_p') of $2080.0\ JK^{-1}kg^{-1}$, and the thermal conductivity (λ_H) of $0.324\ WK^{-1}m^{-1}$. The density of CO_2H (ρ_H) is given as $1116.8\ kgm^{-3}$.

6. Computational conditions

Two types of cells, tetrahedrons and triangular prisms, are applied in the present unstructured grid system, as introduced in **Figure 2**. In detailed, the surface of hydrate uses prism. Both the flow field and inside the pellet are tetrahedral meshes. Upward is the inflow where initially the uniform velocity profile is adopted. Prism mesh and no-slip condition are imposed at the surface of the pellet. To analyze more detailed mass and heat transfer simulatneously, one cell-layer of the prisms that attached to the CO_2H surface is divided into at least five very thin layers as referred in [8] for high Prandtl or Schmidt number. The basic parameters of computation are denoted in **Table 1**. The initial values of dimensionless parameters are listed in **Table 2** at the temperatures from 276.15 to 283.15 K. Reynolds number, Schmidt number, and Prandtl number function of the temperature or pressure are listed in **Table 2**. The minimum grid size of this computational model is listed in **Table 3**. Lm, Lc, and LT are the applied mesh thicknesses. δm, δc, and δT are the thickness of momentum, concentration, and thermal boundary layers, respectively. The relationship between δm, δc, and δT quoted from the theory of flat plate boundary layer is listed below:

$$\delta_m = \frac{5.48\, d}{\sqrt{\mathrm{Re}}\, 2} \tag{12}$$

$$\delta_c = \frac{\delta_m}{1.026 \cdot Sc^{1/3}} \tag{13}$$

$$\delta_T = \frac{\delta_c}{\mathrm{Pr}^{1/3}} \tag{14}$$

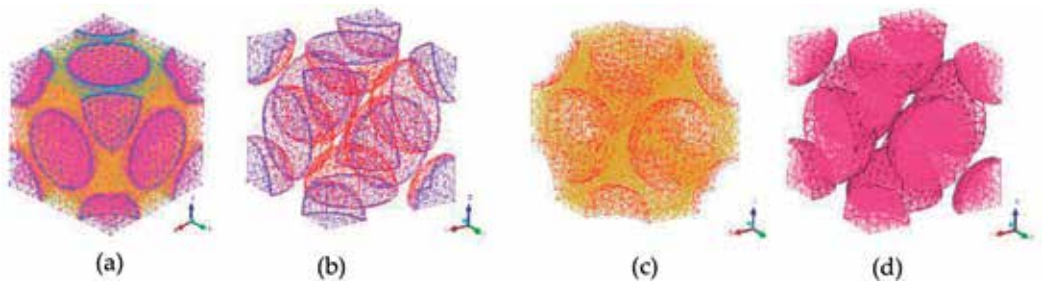

Figure 2. Description of mesh in unstructured grid system of 67,104 cells. (a) Overview, (b) surface of CO_2H, (c) water, and (d) pellets of CO_2H.

Case	Reynold number	Prandtl number	Froude number	Schmidt number	Porous ratio	Temperature of water (K)	Fugacity of equilibrium (MPa)	Fugacity (MPa)
1	50	10	0.023	755	74%	282.15	3.89	3
2		12		880		276.15	1.77	1
3		10		755	66%	282.15	3.89	3
4		12		880		276.15	1.77	1
5		10		755	49%	282.15	3.89	3
6		12		880		276.15	1.77	1
7	100	10	0.046	755		282.15	3.89	3
8	135		0.062					

Table 2. Calculation conditions of this work.

Cell number (porosity)	Sc*	δ_m*	$\delta_{c\&T}$*	L_m	VTL number	$L_{c\&T}$
53,440 (49%)	755	2.358E-04	2.252E-05	1.0E-05	5	2.0E-06
67,104 (66%)	755	2.345E-03	2.252E-04	6.0E-05	5	1.2E-05
77,432 (74%)	755	2.594E-03	2.276E-04	6.0E-05	5	1.2E-05

*Values are quoted from "Chemical Engineering Handbook", Japan (1985)

Table 3. The thicknesses of boundary layers, δ_m and $\delta_{c\&T}$, and grid sizes, L_m and $L_{c\&T}$ (unit: meter).

http://dx.doi.org/10.5772/intechopen.74874

To follow [22] of Eq. (14), the boundary layer's thickness for temperature, δ_T is assumed as the same size as that for mass concentration, δ_c. For the initial temperature of the CO_2H pellet, T_{ini} is assumed as a constant value of 253.15 K.

7. Verification

The in-house code originally developed by [7] has been applied to determine the intrinsic dissociation rate of methane hydrate. The numerical results verified by experimental results are successfully used in calculating one pellet of hydrate in a slow flow rate of high pressure without considering the collapse of hydrate and the nucleation of bubbles referring to [6, 20] as well.

8. Results of case study

In this study, cases with porosity of 74, 66, and 49 are individually discretized as face-centered unstructured packing of hydrate in sediment. CO_2H pellets with initial temperature of 253.15 K dissociate due to the variation of driving force, ex. 0.89 and 0.77 MPa, under thermal stimulation of ambient warm water, ex. 282.15 and 276.15 K. Comparative small driving forces selected here is due to the assumption of no surface's collapse. Computational conditions are listed in **Table 2**. Result of flux at the surface is the converge value as shown in **Figure 3**. In **Figure 4(a)–(c)** at time 0.16(s) show velocity vector of case 1 in three specific sections. In **Figure 5**, the distributions of concentration at 0.16 s are presented. Slight CO_2 discharges at the surface. Relative temperature distributions are indicated in **Figure 6**. As time increases, the dissociation heat of CO_2 hydrate results in water temperature drop significantly as shown in

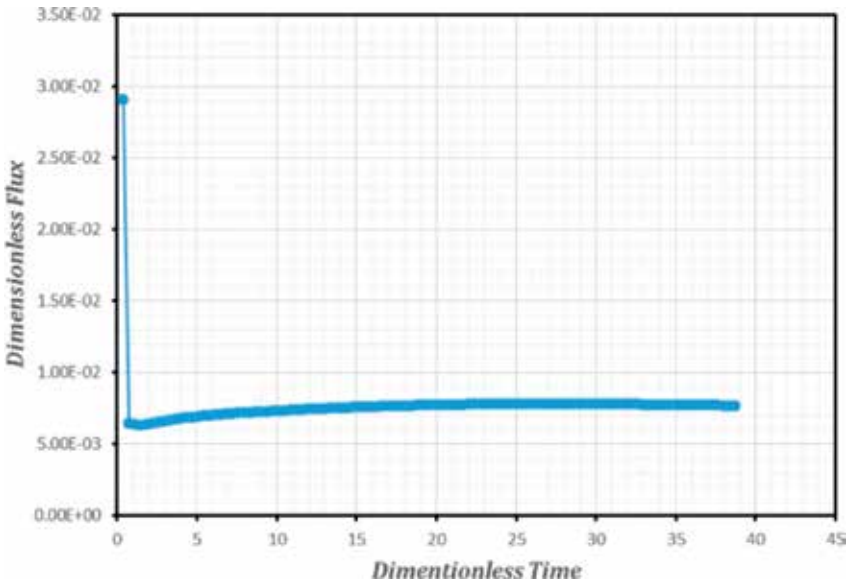

Figure 3. Converge value of case 1.

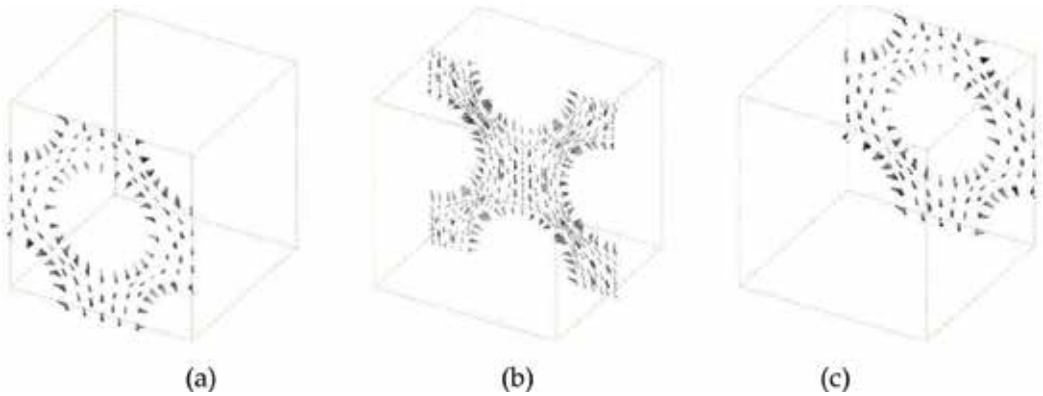

Figure 4. Velocity vector in the vicinity of pellets (case 1: T = 282.15 K, T_{ini} = 253.15 K, Re = 50, Sc = 755, Pr = 10, VTL = 5, and time = 0.16 s). (a) Front section, (b) Center section and (c) Back section.

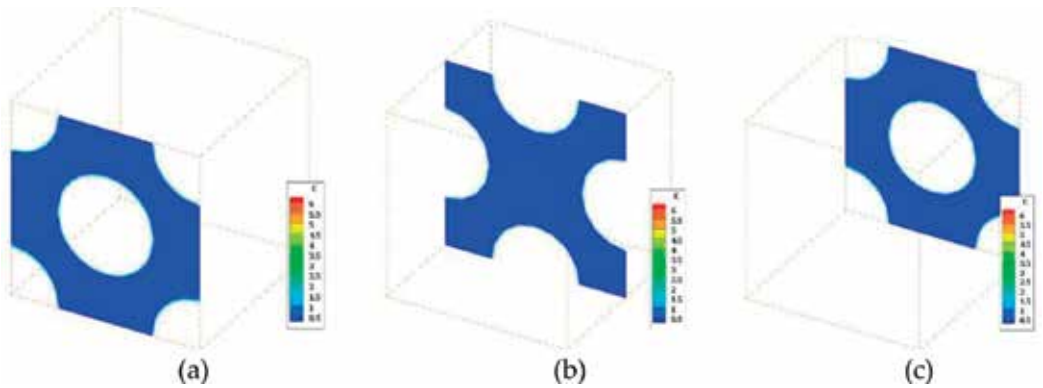

Figure 5. Concentration profile in three specific sections of cubic unit (case 1: time = 0.16 s, unit: mole/m^2 s). (a) Front section, (b) Center section and (c) Back section.

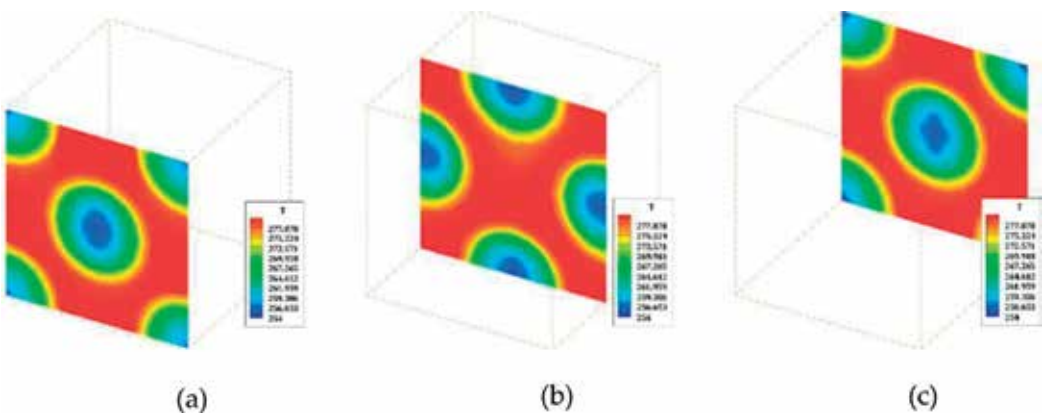

Figure 6. Temperature profile in three specific sections of cubic unit (case 1, time = 0.16 s, unit: K). (a) Front section, (b) Center section and (c) Back section.

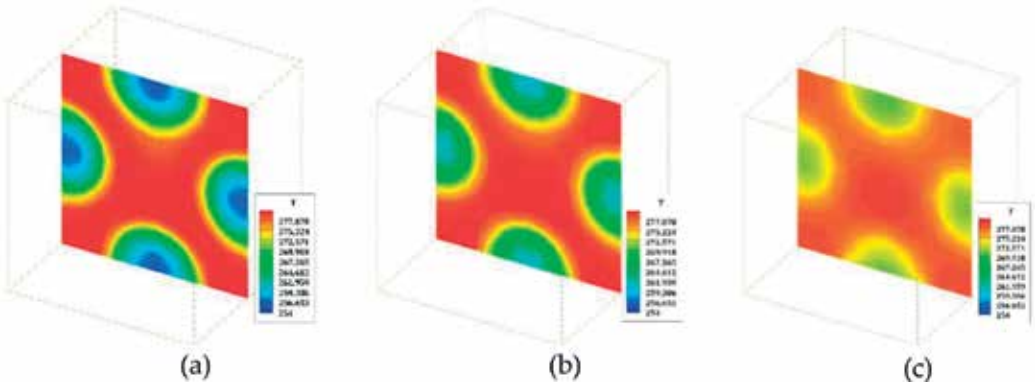

Figure 7. Temperature versus time in center section of cubic unit (case 1, time = 0.16 s, 0.27 s, and 0.54 s, unit: K). (a) Front section, (b) Center section and (c) Back section.

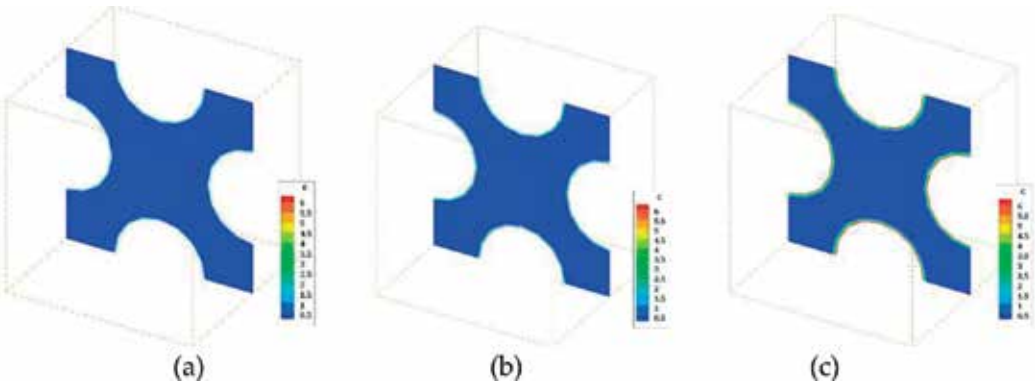

Figure 8. Concentration versus time in center section of cubic unit (case 1, time = 0.16 s, 0.27 s, and 0.54 s, unit: mole/m^2 s). (a) Front section, (b) Center section and (c) Back section.

Figure 7(a)–(c). Relative concentration distribution in center section is shown in **Figure 8**. The heat of water conducts to the solid-side pellet rapidly in few seconds, and slow mass transfer at the surface dominates the dissociation rate rather than fast heat transfer at the surface.

9. Discussion

To follow the modeling illustrated in [14]:

$$F_3 = k_D\left(f_{eq} - f_g\right) = k_{D0}\exp\left(-\frac{\Delta E}{RT}\right)\left(f_{eq} - f_g\right) \tag{15}$$

where $k_{D0}\left[\text{mol Pa}^{-1}\text{s}^{-1}\text{m}^{-2}\right]$ is the rate constant, $f_g(\text{Pa})$ is the fugacity of gaseous CO_2, and f_{eq} is the fugacity of the quadruple equilibrium. They obtained k_{D0} and ΔE for CO_2H as 1.83×10^8 mol Pa^{-1}s^{-1}m^{-2} and 102.88 kJ mol^{-1}, respectively, at temperature and pressure

ranging from 274.15 to 281.15 K and from 1.4 to 3.3 MPa. However, new modified value of ΔE, if considered the real case in the ocean quoted from [16], is 96.49 kJ mol^{-1}. The order of Reynolds number based on the size of a particle, about 16 μm, is calculated as 50. Clarke et al. [28] determined the dissociation rate of CO2H by measuring the nucleated methane gas in V-L state [14]. The comparison of three models is listed in **Table 4**. The results of dissociation flux are summarized in **Figure 9**. Higher water temperature induces higher dissociation flux at the surface of hydrate. Data correlated by [14] show much lower level than both Nihous' model and new model. The numerical results in this work marked as new model in **Figure 9** show consistent result compared with Nihous' model. The dissociation flux in various flow rates in cases 5, 7, and 8 are listed in **Figure 10**. Here, it is noted that porosity is not considered in both Clarke's and Nihous' models, and these two models are only function of temperature and fugacity as presented in Eq. (15). The trend of flux becomes saturated in the figure due to the surface dissociation flux that becomes slow due to the fast mass transfer in bulk flow at Reynolds number over 100.

Item	Modeling	Intrinsic rate of dissociation	Ref.
Clarke's Model	Eq. (15)	K_{D0} = 1.83 * 10^8mole/Pa s m; ΔE = 102.89 kJ/mole	[14]
Nihous' Model	Eq. (15)	K_{D0} = 1.83 * 10^8mole/Pa s m; ΔE = 96.49 kJ/mole	[16]
New Model	Eq. (1)	K_{bl} = exp(−11,729/T + 26,398)	[21]

Table 4. The comparison of three models.

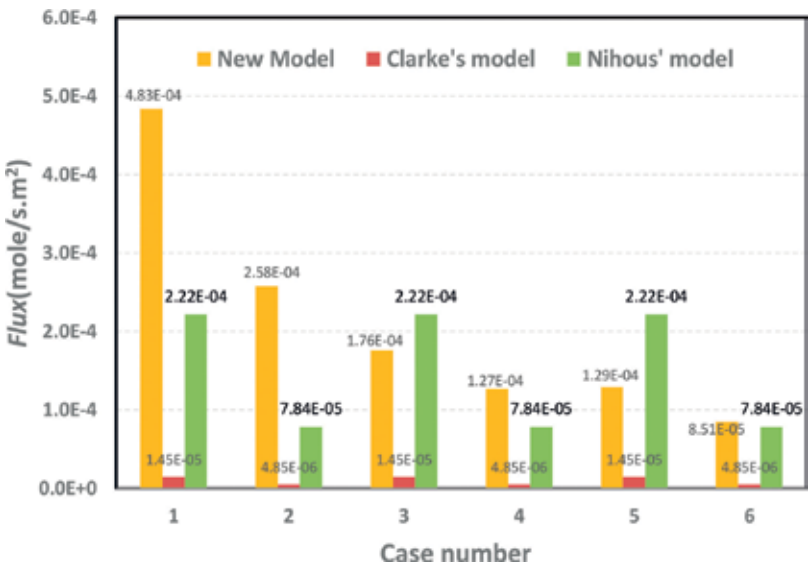

Figure 9. Results of simulation compared to existing two models.

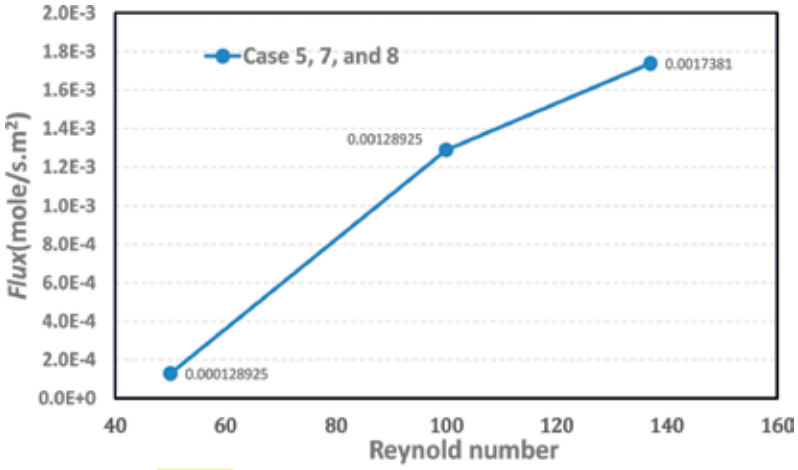

Figure 10. Results of flux in cases 5, 7, and 8.

10. Conclusions

The objective of this work is to establish a new pore-scale model for estimating the dissociation rate of CO_2H in laboratory-scale sediment samples. It is assumed that CO_2H formed homogeneously in spherical pellets. In the bulk flow, concentration and temperature of liquid CO_2 in water flow was analyzed by computational fluid dynamics (CFD) method without considering gas nucleation under high-pressure state. In this work, finite volume method (FVM) was applied in a face-centered regular packing in unstructured mesh. At the surface of hydrate, a dissociation model has been employed. Surface mass and heat transfer between hydrate and water are both visualized. The initial temperature 253.15 K of CO_2H pellets dissociated due to ambient warm water flow of 276.15 and 282.15 K and fugacity variation, ex. 2.01 and 1.23 MPa. Three tentative cases with porosity 74, 66, and 49% are individually simulated in this study. In the calculation, periodic conditions are imposed at each surface of packing. Additionally, the flux at CO_2H's surfaces is compared to Clarke and Bishnoi [13] and Nihous and Masutani [15] 's correlations at Reynolds number of 50. Numerical results of this work show good agreement with Nihous' model. Kinetic modeling by using 3D unstructured mesh of regular cubic unit and CFD scheme seems to be a simple tool to estimate the dissociation rate of CO_2H in laboratory-scale experiments, and could be easily extended to determine complex phenomena coupled with momentum, mass, and heat transfer in the sediment samples.

Acknowledgements

This work was supported by DOIT, Ministry of Science and Technology under contract No. MOST 106-3113-M-002-006. The authors also wish to acknowledge Professor Toru SATO for the valuable advices and guidance.

Nomenclature

C	volumetric molar concentration of CO_2 in the ambient water $\left[\text{mol m}^{-3}\right]$
C_H	volumetric molar concentration of CO_2 in the aqueous solution equilibrated with the stable hydrate phase $\left[\text{mol m}^{-3}\right]$
C'	volumetric molar concentration of CO_2 in water at the centroid of a cell attaching to the hydrate surface $\left[\text{mol m}^{-3}\right]$
C_I	volumetric molar concentration of CO_2 in the ambient aqueous solution at the surface of the hydrate ball $\left[\text{mol m}^{-3}\right]$
C_X	average molar volumetric concentration of CO_2 in the ambient water flow for a given cross section of water flow $\left[\text{mol m}^{-3}\right]$
d	diameter of the CO_2 hydrate ball [m]
D	diffusion coefficient of CO_2 in water $\left[\text{m s}^{-2}\right]$
E	activation energy $\left[\text{J mol}^{-1}\right]$
F	dissociation rate flux $\left[\text{mol s}^{-1}\ \text{m}^{-2}\right]$
f_{eq}	fugacity of the quadruple equilibrium [Pa].
f_g	fugacity of gaseous CO_2 [Pa]
G	molar Gibbs free energy $\left[\text{J mol}^{-1}\right]$
H_L	latent heat of hydrate dissociation $\left[\text{J mol}^{-1}\right]$
h_L	length of the water layer attached to the hydrate surface [m]
k_{D0}	intrinsic dissociate rate constant based on Clarke-Bishnoi model $\left[\text{mol Pa}^{-1}\text{s}^{-1}\text{m}^{-2}\right]$
k_{bl}	dissociation rate constant based on new model $\left[\text{mol}^2\ \text{J}^{-1}\ \text{s}^{-1}\text{m}^{-2}\right]$
L	thickness of computational cell [m]
M_B	molecular weight of water $\left[\text{g mol}^{-1}\right]$
P	thermodynamic pressure [Pa]
P_{eq}	quadruple equilibrium pressure for CO_2 hydrate as a function of T [Pa]
Q	volumetric flow rate of the ambient water $\left[\text{m}^3\text{s}^{-1}\right]$

$\dot{Q}_H$	the rate at which the latent heat is transferred to the CO_2 hydrate by dissociation $\left[\mathrm{Jm^{-2}s^{-1}}\right]$
R	gas constant, 8.314 $\left[\mathrm{J\ K^{-1}\ mol^{-1}}\right]$
T	absolute temperature [K]
T_L	temperature at the centroids of a cell in the solid hydrate [K]
T_H	temperature at the centroids of a cell in the aqueous phase [K]
$\boldsymbol{u}$	velocity vectors [m/s]
x	mole fraction of CO_2 [-]
x_{eq}	solubility of CO_2 in the aqueous solution in equilibrium with the stable hydrate phase [-]
x_I	mole fraction of CO_2 in the aqueous phase at the surface of the hydrate ball [-]
α_L	thermal diffusivity in the aqueous phase $\left[\mathrm{m\ s^{-2}}\right]$
α_H	thermal diffusivity in the hydrate ball $\left[\mathrm{m\ s^{-2}}\right]$
Δr	thickness of the computational cell [m]
δ	thickness of the boundary layer [m]
$\Delta\mu$	chemical potential difference $\left[\mathrm{J\ mol^{-1}}\right]$
ρ_w	density of the ambient water $\left[\mathrm{kg\ m^{-3}}\right]$
φ	the association parameter for the solvent water
η_L	the viscosity of water [mPa s]
V_A	the molar volume of CO_2 $\left[\mathrm{m^3mol^{-1}}\right]$
ν_L	kinematic viscosity of water $\left[\mathrm{ms^{-2}}\right]$
λ_L	heat conductivity of water $\left[\mathrm{W\ K^{-1}\ m^{-1}}\right]$
λ_H and λ_L	the heat conductivities in the hydrate and water $\left[\mathrm{WK^{-1}m^{-1}}\right]$

Author details

Wu-Yang Sean

Address all correspondence to: wuyangsean@gmail.com

Department of Environmental Engineering, Chung Yuan Christian University, Taiwan

References

[1] Jeong S-M, Hsieh L-HC, Huang C-Y, Sean W-Y. Direct numerical simulation of CO_2 hydrate dissociation in pore-scale flow by applying CFD method. International Journal of Heat and Mass Transfer. 2017;**107**:300-306

[2] Andersson V, Kvaerner A, Haines M. Gas hydrates for deep ocean storage of CO_2—novel technology for utilising hydrates for transport of CO_2. In: Wilson M, Morris T, Gale J, Thambimuthu K, editors. Greenhouse Gas Control Technologies, Volume II. New York: Elsevier; 2005. pp. 1487-1492

[3] Molins S, Trebotich D, Steefel CI, Shen C. An investigation of the effect of pore scale flow on average geochemical reaction rates using direct numerical simulation. Water Resources Research. 2012;**48**:7453-7460. DOI: 10.1029/2011WR011404

[4] Davison SM, Yoon H, Martinez MJ. Pore scale analysis of the impact of mixing-induced reaction dependent viscosity variations. US Department of Energy Publications. Paper 110. 2012. http://digitalcommons.unl.edu/usdoepub/110

[5] Gregor R, Stephen HK, William BD, Laura AS, Edward TP, John P, Peter GB. Dissolution rates of pure methane hydrate and carbon-dioxide hydrate in undersaturated seawater at 1000-m depth. Geochimica et Cosmochimica Acta. 2004;**68**(2):285-292

[6] Inui M, Sato T. Economical feasibility study on CO_2 sequestration in the form of hydrate under seafloor. Proceedings of 26th International Conference on Offshore Mechanical and Arctic Engineering. 2006;OMAE06-92306:1-10

[7] Uchida T, Ebinuma T, Takeya S, Nagao J, Narita H. Effects of pore sizes on dissociation temperatures and pressures of methane, carbon dioxide, and propane hydrates in porous media. The Journal of Physical Chemistry. B. 2002;**106**:820-826

[8] Jung RT, Sato T. Numerical simulation of high Schmidt number flow on unstructured hybrid mesh. Journal of Computational Physics. 2004;**203**:221-249

[9] Sloan ED. Clathrate hydrate of natural gases. New York: Dekker; 1998

[10] Aya I, Yamane K, Nariai H. Solubility of CO_2 and density of CO_2 hydrate at 30MPa. Energy. 1997;**22**:263-271

[11] Yang SO, Yang IM, Kim YS, Lee CS. Measurement and prediction of phase equilibria for water + CO_2 in hydrate forming condition. Fluid Phase Equilibria. 2000;**175**:75-89

[12] Servio P, Englezos P. Effect of temperature and pressure on the solubility of carbon dioxide in water in the presence of gas hydrate. Fluid Phase Equilibria. 2001;**190**:127-134

[13] Clarke MA, Bishnoi PR. Determination of the intrinsic rate constant and activation energy of CO_2 gas hydrate decomposition using in-situ particle size analysis. Chemical Engineering Science. 2004;**59**:2983-2993

[14] Sean W, Sato T, Yamasaki A, Kiyono F. CFD and experimental study on methane hydrate dissociation part II. General cases. AICHE Journal. 2007;**53**:2148-2160

[15] Nihous GC, Masutani SM. Notes on the dissolution rate of gas hydrates in undersaturated water. Chemical Engineering Science. 2006;**61**:7827-7830

[16] O'Connor RM, Fredrich JT. Microscale flow modelling in geologic materials. Physics and Chemistry of the Earth, Part A: Solid Earth and Geodesy. 1999;**24**(7):611-616

[17] Piller M, Nolich M, Favretto S, Radaelli F, Rossi E. Analysis of hydraulic permeability in porous media: From high resolution X-ray tomography to direct numerical simulation. Transport in Porous Media. 2009;**80**(1):57-78

[18] Sahimi M. Flow and Transport in Porous Media and Fractured Rock. Weinheim: VCG; 1995

[19] Boomsma K, Poulikakos D, Ventikos Y. International Journal of Heat and Fluid Flow. 2003;**24**:825

[20] Fukumoto A, Sean WY, Sato T, Yamasaki A, Kiyono F. Estimation of dissociation rate constant of CO_2 hydrate in water flow. Greenhouse Gases: Science and Technology. 2015; **5**(2):169-179

[21] Pohlhausen E. Der Wärmeaustausch zwischen festen Körpern und Flüssigkeiten mit kleiner reibung und kleiner Wärmeleitung. Zeitschrift für Angewandte Mathematik und Mechanik. 1921;**1**:115-121. DOI: 10.1002/zamm.19210010205

[22] Shu SS, Lee MJ. Dynamic behavior of methane hydrates formation and decomposition with a visual high-pressure apparatus. Journal of the Taiwan Institute of Chemical Engineers. 2016;**62**:1-9

Chapter 3

Darcy-Forchheimer Flow of Casson Nanofluid with Heat Source/Sink: A Three-Dimensional Study

Gosikere Kenchappa Ramesh

Additional information is available at the end of the chapter

http://dx.doi.org/10.5772/intechopen.74170

Abstract

In this chapter, three-dimensional Casson nanoliquid flow in two lateral directions past a porous space by Darcy-Forchheimer articulation is examined. The study includes the impact of uniform heat source/sink and convective boundary condition. The administering partial differential equations are shaped to utilizing comparability changes into a set of nonlinear normal differential conditions which are fathomed numerically. The self-comparative arrangements are gotten and contrasted and accessible information for uncommon cases. The conduct of parameters is displayed graphically and examined for velocity, temperature, and nanoparticle volume part. It is discovered that temperature and nanoparticle volume fraction rise for enhancement of Forchheimer and porosity parameters.

Keywords: three-dimensional flow, Darcy-Forchheimer porous medium, Casson nanoliquid, uniform heat source/sink, convective boundary condition, numerical solutions

1. Introduction

In many assembling processes and for mechanical reason, the investigation of heat exchange and boundary layer flow over linearly and nonlinearly extending surface are much imperative. These procedures and applications incorporate streamlined feature forming, wire drawing, and paper generation where a specific temperature will be required for cooling the particles in the liquid. At first, the stream qualities have been analyzed by [1] overextending surfaces. The perfection of finishing up item relies upon the rate of warmth exchange at the surface of extending material. Many creators expanded crafted by [1] managed heat exchange qualities alongside the flow conduct in different physical circumstances in [2–8].

Non-Newtonian fluids can't be portrayed because of nonexistence of single constitutive connection among stress and rate of strain. In the current year, non-Newtonian fluids have turned out to be increasingly essential because of its mechanical applications. Truth be told, the enthusiasm for boundary layer flows of non-Newtonian fluid is expanding significantly because of its extensive number of functional applications in industry producing preparing and natural fluids. Maybe, a couple of principle illustrations identified with applications are plastic polymer, boring mud, optical fibers, paper generation, hot moving, metal turning, and cooling of metallic plates in a cooling shower and numerous others. Since no single non-Newtonian model predicts every one of the properties of non-Newtonian fluid along these lines examinations proposed different non-Newtonian fluid models. These models are essentially classified into three classifications specifically differential-, rate-, and fundamental-type fluids. In non-Newtonian fluid, shear stresses and rates of strain/disfigurement are not directly related. Such fluid underthought which does not comply with Newton's law is a straightforward non-Newtonian fluid model of respectful sort. In 1959, Casson displayed this model for the flow of viscoelastic fluids. This model has a more slow progress from Newtonian to the yield locale. This model is utilized by oil builds in the portrayal of bond slurry and is better to predict high shear-rate viscosities when just low and middle road shear-rate information are accessible. The Casson show is more exact at both high and low shear rates. Casson liquid has one of the kind attributes, which have wide application in sustenance handling, in metallurgy, in penetrating operation and bio-designing operations, and so on. The Casson show has been utilized as a part of different businesses to give more exact portrayal of high shear-rate viscosities when just low and moderate shear-rate information are accessible [9]. Toward the starting Nadeem et al. [10] introduce the idea of Casson fluid and demonstrate over an exponentially extending sheet. Numerous examinations identified with viscoelastic properties of liquid are underthought [11–17].

The nanoparticles in by and large are made of metal oxides, metallic, carbon, or some other materials [18]. Standard fluid has weaker conductivity. This weaker conductivity can be enhanced incredibly with the utilization of nanoparticles. Truly, the Brownian movement factor of nanoparticles is base fluid and is essential toward this path. An extraordinary measure of warmth is delivered in warm exchangers and microelectromechanical procedures to lessen the framework execution. Fluid thermal conductivity is enhanced by nanoparticle expansion just to cool such modern procedures. The nanoparticles have shallow significance in natural and building applications like prescription, turbine sharp-edge cooling, plasma- and laser-cutting procedure, and so on. Sizeable examinations on nanofluids have been tended to in the writing. Buongiorno [19] has investigated the mechanisms of nanofluid by means of snapshot of nanoparticles in customary base fluid. Such instruments incorporate nanoparticle measure, Magnus effect, dormancy, molecule agglomeration, Brownian movement, thermophoresis, and volume portion. Here, we introduce some imperative scientists who have been accounted for by considering the highlights of thermophoretic and Brownian movement [20–27].

In displaying the flow in permeable media, Darcy's law is a standout among the most prominent models. Particularly, flow in permeable media is exceptionally valuable in grain stockpiling, development of water in repositories, frameworks of groundwater, fermentation process, raw petroleum generation, and oil assets. In any case, it is by and large

perceived that Darcy's model may over anticipate the convective streams when the inertial drag and vorticity dissemination coproductive are considered. The expansion of established Darcy demonstrates incorporates inertial drag and vorticity dispersion. To think about the inertial drag and vorticity dispersion, Forchheimer [28] joined the root mean square. Forchheimer's term was named by Muskat [29] and inferred that the consideration of Forchheimer's term is substantial for high Reynolds number. Pal and Mondal [30] examined the hydromagnetic Darcy-Forchheimer flow for variable liquid property. Utilizing HAM strategy, Hayat et al. [31] got the systematic answer for Darcy-Forchheimer stream of Maxwell liquid by considering the Cattaneo-Christov hypothesis. Vishnu Ganesh et al. [32] analyzed the thick and Ohmic dispersals, and the second-order slip consequences for Darcy-Forchheimer flow of nanoliquid past an extending/contracting surface. Scientific model for Darcy-Forchheimer stream of Maxwell fluid with attractive field and convective boundary condition is given by Sadiq and Hayat [33]. Utilizing Keller's box strategy, Ishak et al. [34] numerically examined the magnetohydrodynamic flow and heat exchange exhibitions over an extending cylinder. Mixed convective flow and the related warmth and mass exchange qualities over a vertical sheet immersed in a permeable medium have been explored by Pal and Mondal [35] by considering different impacts, for example, Soret, Dufour, and thermal radiation.

The principle objective here is to uncover the Darcy-Forchheimer connection on a three-dimensional Casson nanofluid flow past a stretching sheet. Heat transfer is handled with regular heat generation/absorption and convective-type boundary condition.

2. Mathematical formulation

Three-dimensional flow of Casson nanofluid filling permeable space by Darcy-Forchheimer connection is considered. Flow is bidirectional extending surface. Nanofluid model depicts the properties of Brownian dispersion and thermophoresis. Concurrent states of heat convective and heat source/sink are executed. We receive the Cartesian coordinate in such a way to the point that and pivot are picked along x and y ordinary to the stretchable surface. Let $U_w(x) = ax$ and $V_w(y) = by$ be the extending velocity along x and y directions separately. The surface temperature is directed by a convective heating procedure which is depicted by heat exchange coefficient h_f and temperature of hot liquid T_f under the surface (see **Figure 1**). The boundary layer equations for flow underthought are

$$\frac{\partial u}{\partial x} + \frac{\partial v}{\partial y} + \frac{\partial w}{\partial z} = 0, \tag{1}$$

$$u\frac{\partial u}{\partial x} + v\frac{\partial u}{\partial y} + w\frac{\partial u}{\partial z} = \nu\left(1 + \frac{1}{\beta}\right)\frac{\partial^2 u}{\partial z^2} - \frac{\nu}{K}u - Fu^2, \tag{2}$$

$$u\frac{\partial v}{\partial x} + v\frac{\partial v}{\partial y} + w\frac{\partial v}{\partial z} = \nu\left(1 + \frac{1}{\beta}\right)\frac{\partial^2 v}{\partial z^2} - \frac{\nu}{K}v - Fv^2, \tag{3}$$

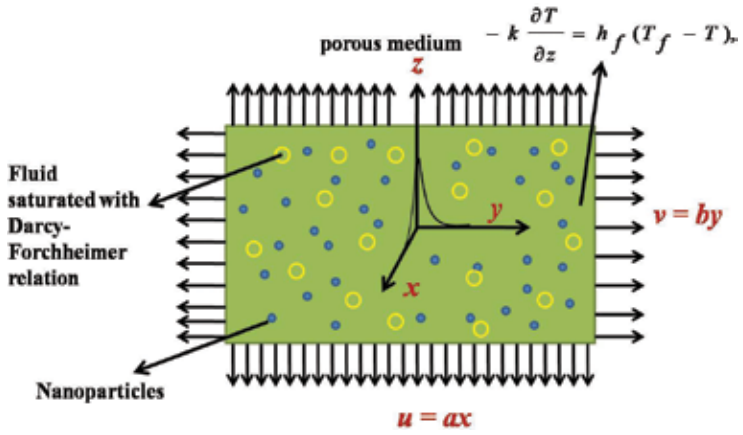

Figure 1. Geometry of the problem.

$$u\frac{\partial T}{\partial x} + v\frac{\partial T}{\partial y} + w\frac{\partial T}{\partial z} = \alpha_m\frac{\partial^2 T}{\partial z^2} + \frac{(\rho c)_p}{(\rho c)_f}\left(D_B\left(\frac{\partial T}{\partial z}\frac{\partial C}{\partial z}\right) + \frac{D_T}{T_\infty}\left(\frac{\partial T}{\partial z}\right)^2\right) + \frac{q_0}{(\rho c)_p}(T - T_\infty) \tag{4}$$

$$u\frac{\partial C}{\partial x} + v\frac{\partial C}{\partial y} + w\frac{\partial C}{\partial z} = D_B\left(\frac{\partial^2 C}{\partial z^2}\right) + \frac{D_T}{T_\infty}\left(\frac{\partial^2 T}{\partial z^2}\right) \tag{5}$$

and boundary conditions of the problem is

$$u = ax, v = by, w = 0, -k\frac{\partial T}{\partial z} = h_f(T_f - T), C = C_w \text{ at } z = 0$$

$$u \to 0, v \to 0, T \to T_\infty, C \to C_\infty \text{ as } z \to \infty \tag{6}$$

Here u, v and w represent as components of velocity in x, y and z directions, respectively; $\nu = \frac{\mu}{\rho_f}$ stands for kinematic viscosity; μ for dynamic viscosity; ρ_f for density of base liquid; K for permeability of porous medium; $F = \frac{C_b}{xK^{\frac{1}{2}}}$ for nonuniform inertia coefficient of porous medium; C_b for drag coefficient; T for temperature; $\alpha_m = \frac{K}{(\rho c)_f}$ for thermal diffusivity; q_0 volumetric rate of heat generation and absorption; β is the Casson parameter; k for thermal conductivity; $(\rho c)_p$ for effective heat capacity of nanoparticles; $(\rho c)_f$ for heat capacity of fluid; C for concentration; D_B for Brownian diffusion coefficient; D_T for thermophoretic diffusion coefficient; T_∞ for ambient fluid temperature; C_∞ for ambient fluid concentration; and a and b for positive constants.

Selecting similarity transformations are

$$u = axf'(\varsigma), v = ayg'(\varsigma), w = -(a\nu)^{\frac{1}{2}}(f + g),$$

$$\theta(\varsigma) = \frac{T - T_\infty}{T_f - T_\infty}, \phi(\varsigma) = \frac{C - C_\infty}{C_w - C_\infty}, \varsigma = \left(\frac{a}{\nu}\right)^{\frac{1}{2}} z \tag{7}$$

Applying Eq. (7) in (1) is verified. and Eqs. (2)–(5) are

$$\left(1 + \frac{1}{\beta}\right) f''' + (f + g) f'' - f'^2 - \lambda f' - F_r f'^2 = 0 \tag{8}$$

$$\left(1 + \frac{1}{\beta}\right) g''' + (f + g) g'' - g'^2 - \lambda g' - F_r g'^2 = 0 \tag{9}$$

$$\theta'' + \Pr\left((f + g)\theta' + Nb\theta'\phi' + Nt\theta'^2\right) + \Pr Q\theta(\eta) = 0 \tag{10}$$

$$\phi'' + Le \Pr(f + g)\phi' + \frac{Nt}{Nb}\theta'' = 0 \tag{11}$$

Boundary conditions of Eq. (6) become

$$f(0) = g(0) = 0,\ f'(0) = 1,\ g'(0) = \alpha,\ \theta'(0) = -Bi(1 - \theta(0)), \phi(0) = 1,$$

$$f'(\infty) \to 0,\ g'(\infty) \to 0,\ \theta(\infty) \to 0, \phi(\infty) \to 0 \tag{12}$$

In the above expressions, λ stands for porosity parameter, F_r for Forchheimer parameter, α for ratio parameter, Pr for Prandtl number, Le for Schmidt number, Bi for Biot number, Nt for thermophoresis parameter, Nb for Brownian motion parameter, and Q heat source/sink parameter.

These dimensionless variables are given by

$$\lambda = \frac{\nu}{Ka}, F_r = \frac{C_b}{K^{\frac{1}{2}}},\ \alpha = \frac{b}{a}, \Pr = \frac{\nu}{\alpha_m},\ Le = \frac{\nu}{D_B},\ Q = \frac{q_0}{a\rho c_p},\ Bi = \frac{h_f}{k}\sqrt{\frac{\nu}{a}},$$
$$Nt = \frac{(\rho c)_p D_T (T_f - T_\infty)}{(\rho c)_f \nu\, T_\infty},\ Nb = \frac{(\rho c)_p D_B C_\infty}{(\rho c)_f \nu}.$$

Dimensionless relations of skin friction coefficient, local Nusselt number, and local Sherwood number are as follows:

$$\mathrm{Re}_x^{\frac{1}{2}} C_{fx} = \left(1 + \frac{1}{\beta}\right) f''(0),\ \left(\frac{x}{y}\right) \mathrm{Re}_y^{\frac{1}{2}} C_{fy} = \alpha\left(1 + \frac{1}{\beta}\right) g''(0),$$

$$\mathrm{Re}_x^{-\frac{1}{2}} N u_x = -\theta'(0), \text{ and } \mathrm{Re}_x^{-\frac{1}{2}} S u_x = -\phi'(0),$$

where $\mathrm{Re}_x = U_w \frac{x}{\nu}$ and $\mathrm{Re}_y = V_w \frac{y}{\nu}$ depict the local Reynolds numbers.

3. Results and discussion

The correct arrangements do not appear to be achievable for an entire arrangement of Eqs. (8)–(11) with proper limit conditions given in Eq. (12) in light of the nonlinear shape. This reality compels one to get the arrangement of the issue numerically. Suitable likeness change is received to change the overseeing incomplete differential conditions into an arrangement of non-straight customary differential conditions. The resultant limit esteem issue is understood numerically utilizing an efficient fourth-order Runge-Kutta method alongside shooting method (see Ramesh and Gireesha [27]). Facilitate the union examination is available in **Table 1**. For the verification of precision of the connected numerical plan, an examination of the present outcomes compared to the $-\left(1+\frac{1}{\beta}\right)f''(0)$ and $-\left(1+\frac{1}{\beta}\right)g''(0)$ (nonappearance of Forchheimer parameter, porosity parameter) with the accessible distributed consequences of Ahmad and Nazar [16] and Nadeem et al. [15] is made and exhibited in **Table 2**, demonstrates a great understanding in this manner give confidence that the numerical outcomes got are precise.

This section is fundamentally arranged to depict the effect of different correlated physical parameters on velocity profiles $f'(\varsigma)$, $g'(\varsigma)$, temperature profile $\theta(\varsigma)$, nanoparticle part $\phi(\varsigma)$, skin

ς	$f(\varsigma)$	$f'(\varsigma)$	$-f''(\varsigma)$
0	0.000000	1.000000	0.763674
1	0.695167	0.456344	0.365768
2	1.008110	0.202536	0.166242
3	1.146071	0.088680	0.073585
4	1.206291	0.038589	0.032175
5	1.232460	0.016746	0.013992
6	1.243809	0.007258	0.006070
7	1.248727	0.003144	0.002630
8	1.250857	0.001362	0.001139
9	1.251780	0.000590	0.000493
10	1.252179	0.000255	0.000213
11	1.252352	0.000111	0.000092
12	1.252427	0.000047	0.000040
13	1.252460	0.000020	0.000017
14	1.252474	0.000008	0.000007
15	1.252480	0.000006	0.000003
16	1.252482	0.000001	0.000001
17	1.252483	0.000000	0.000000

Table 1. Convergence analysis of the present work.

β	$c = 0$	$c = 0.5$		$c = 1.0$
	$-\left(1+\frac{1}{\beta}\right)f''(0)$	$-\left(1+\frac{1}{\beta}\right)f''(0)$	$-\left(1+\frac{1}{\beta}\right)g''(0)$	$-\left(1+\frac{1}{\beta}\right)g''(0)$
1	1.414213	1.545869	0.657899	1.659891
	[15, 16]	[15, 16]	[15, 16]	[15, 16]
5	1.095445	1.197425	0.509606	1.285746
	[15, 16]	[15, 16]	[15, 16]	[15, 16]
1000	1.000499	1.093641	0.465437	1.174307
	[15, 16]	[15, 16]	[15, 16]	[15, 16]

Table 2. Current numerical values and validation for friction factor $-\left(1+\frac{1}{\beta}\right)f''(0)$.

friction coefficient, and the local Nusselt and local Sherwood number through **Figures 2–16**. Give the first focus on the impact of extending parameter (α) on velocity profile as shown in **Figure 2**. It is noticed that for expanding benefits of extending parameter α, it decreases the speed $f'(\varsigma)$, while $g'(\varsigma)$ fluctuates for different benefits of extending parameter α. It see that for $\alpha = 0$, exhibit wonders lessen the instance of two dimensional linear stretching, while for

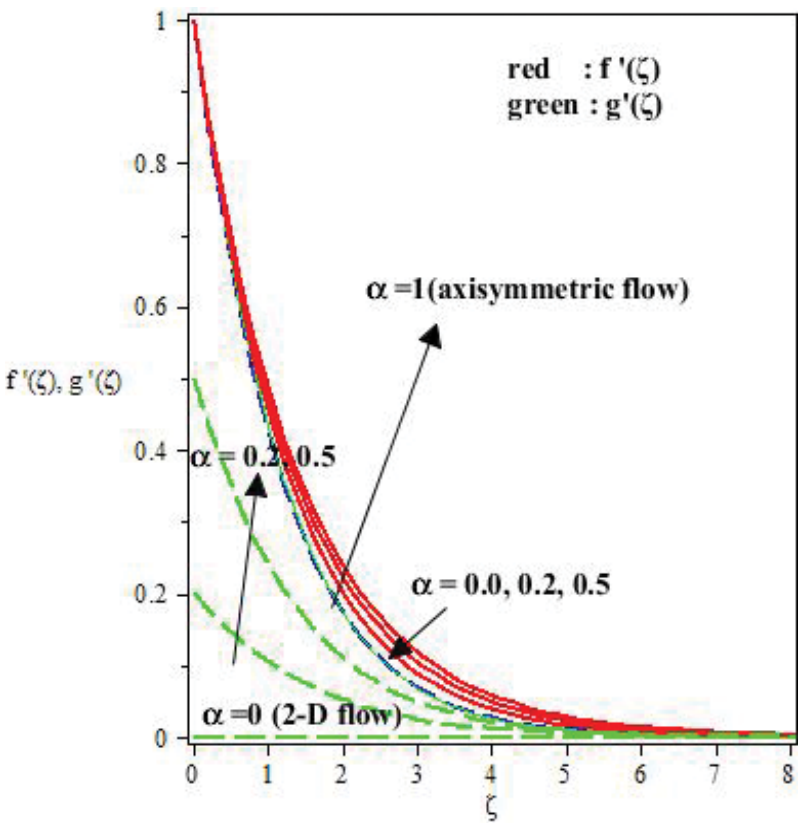

Figure 2. Influence of α on velocity field.

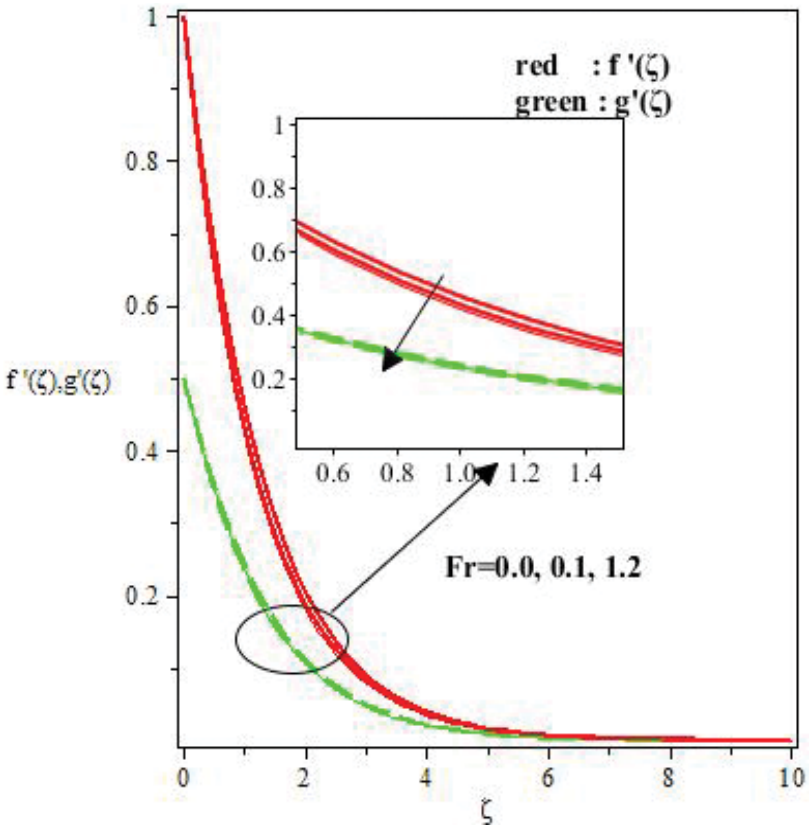

Figure 3. Influence of *Fr* on velocity fields.

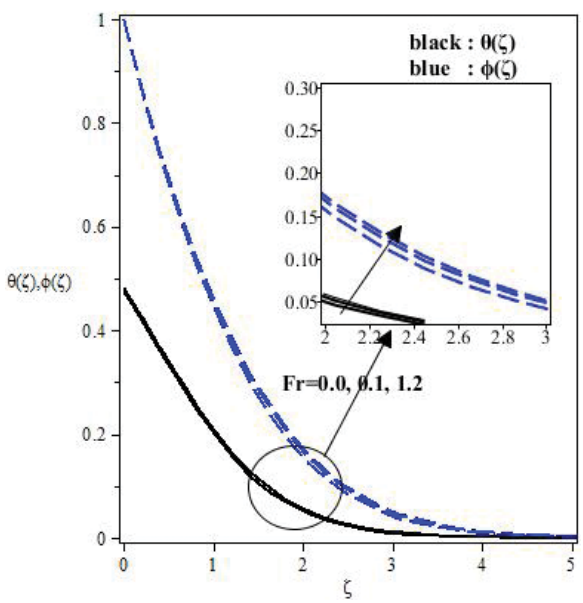

Figure 4. Influence of *Fr* on temperature and concentration fields.

http://dx.doi.org/10.5772/intechopen.74170

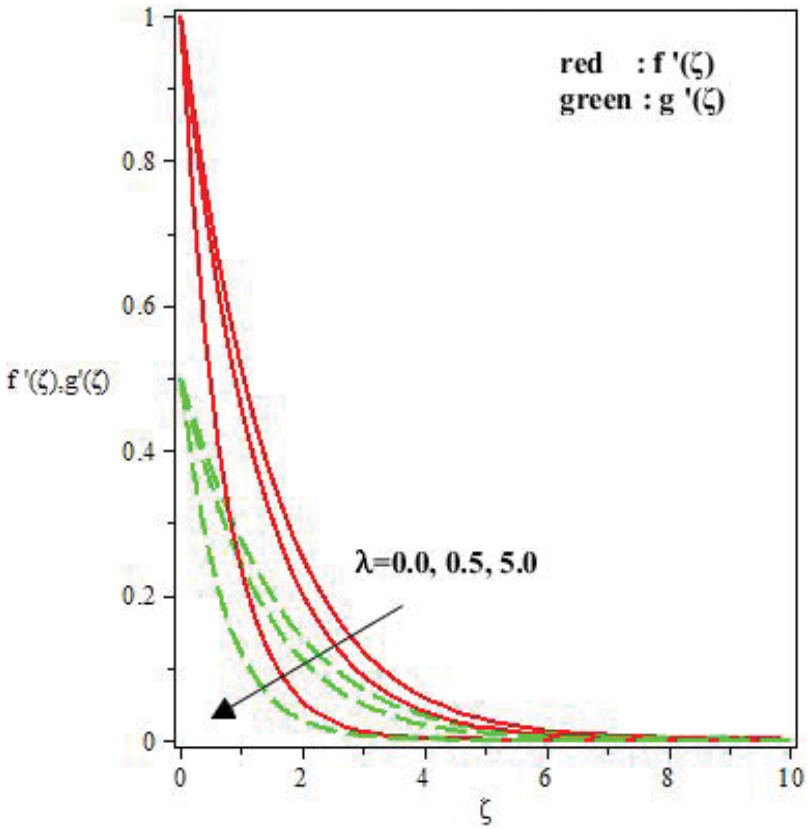

Figure 5. Influence of λ on velocity field.

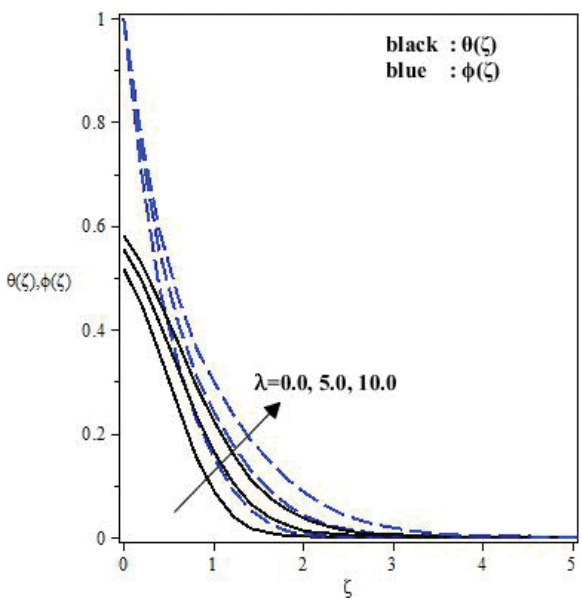

Figure 6. Influence of λ on temperature and concentration fields.

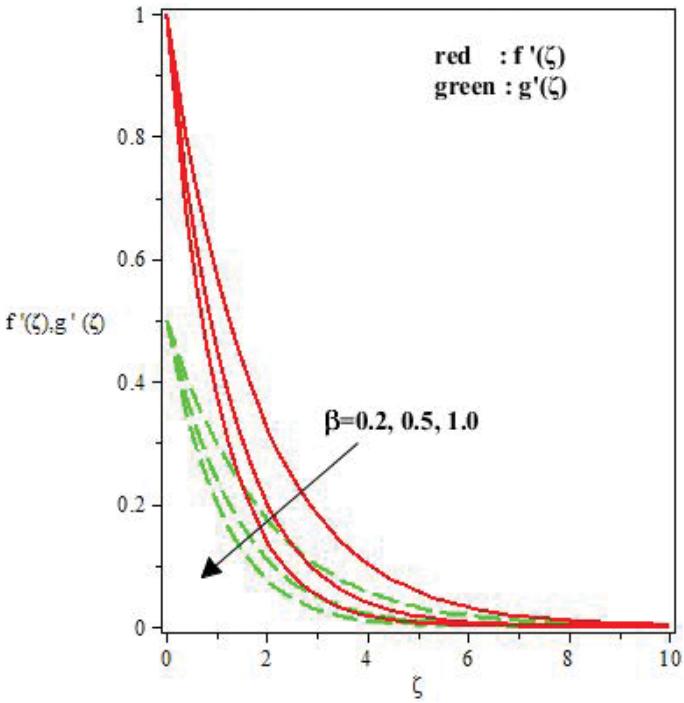

Figure 7. Influence of β on velocity fields.

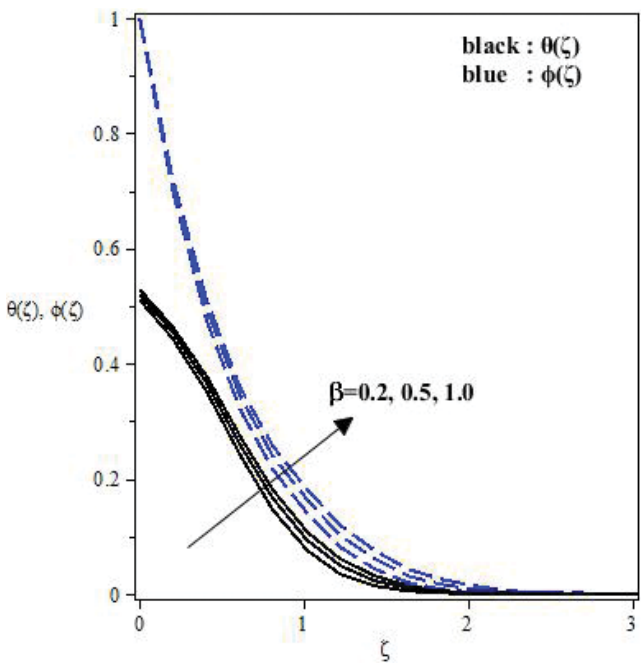

Figure 8. Influence of β on temperature and concentration fields.

http://dx.doi.org/10.5772/intechopen.74170

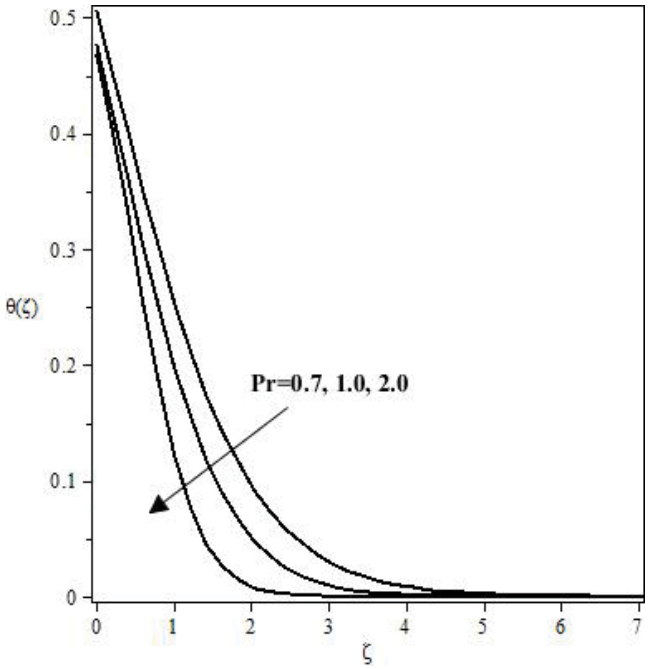

Figure 9. Influence of Pr on temperature fields.

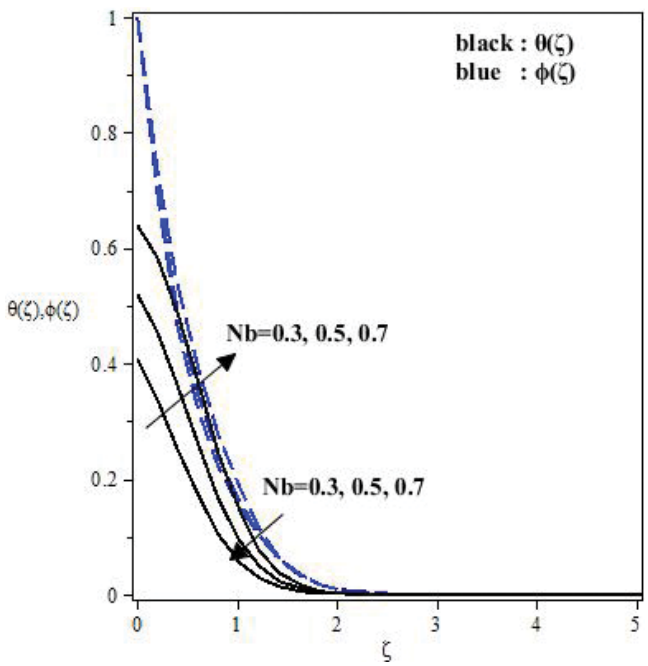

Figure 10. Influence of *Nb* on temperature and concentration fields.

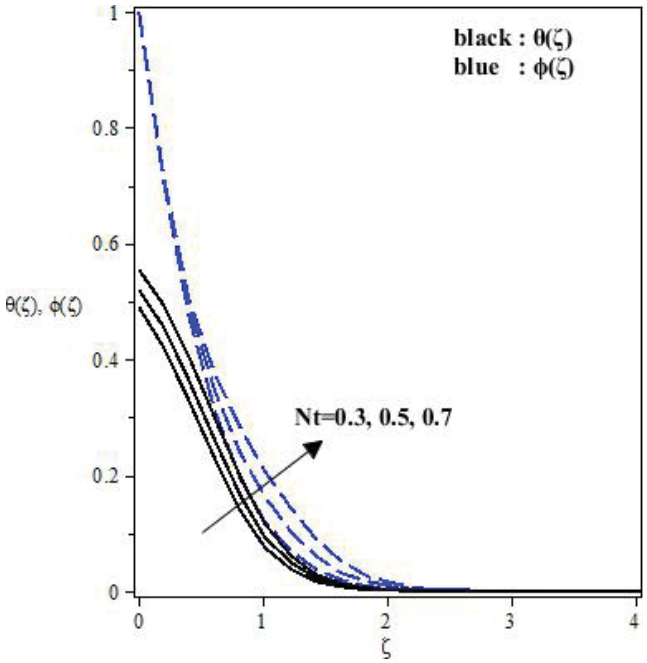

Figure 11. Influence of *Nt* on temperature and concentration fields.

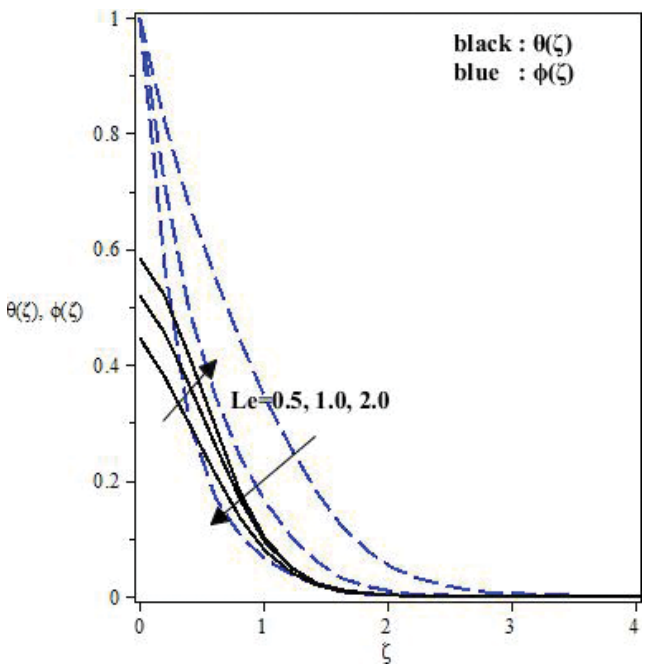

Figure 12. Influence of *Le* on temperature and concentration fields.

http://dx.doi.org/10.5772/intechopen.74170

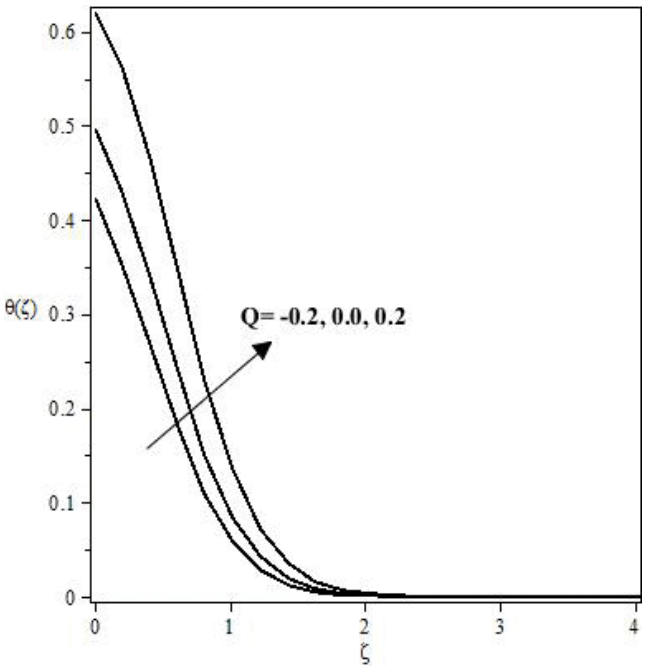

Figure 13. Influence of *Q* on temperature field.

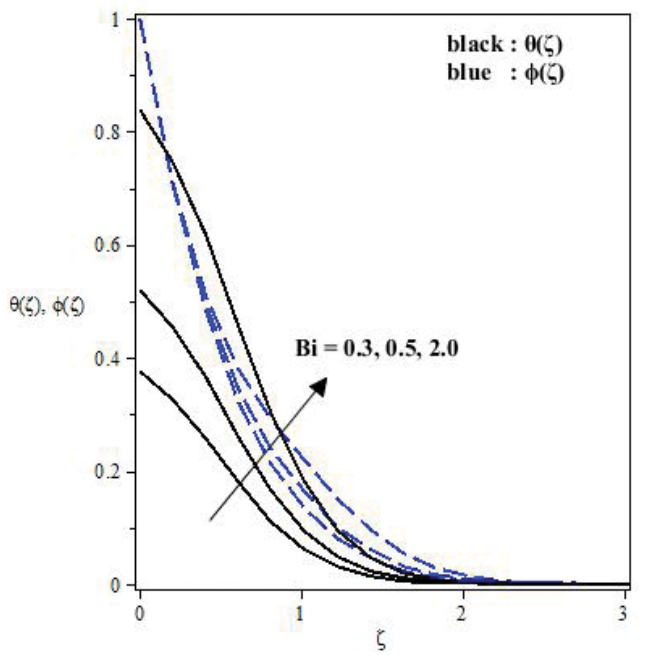

Figure 14. Influence of *Bi* on temperature and concentration fields.

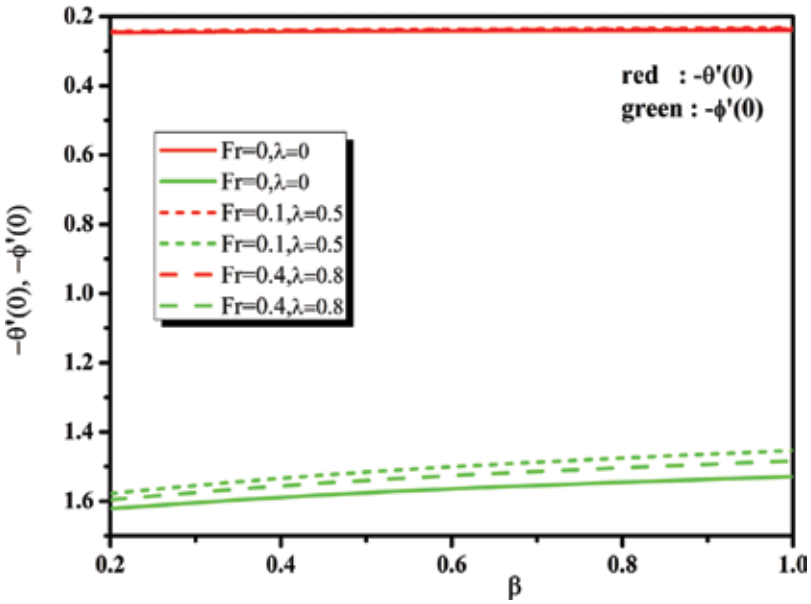

Figure 15. Variation of $-\theta'(0)$ and $-\phi'(0)$ with β for different values of Fr, λ.

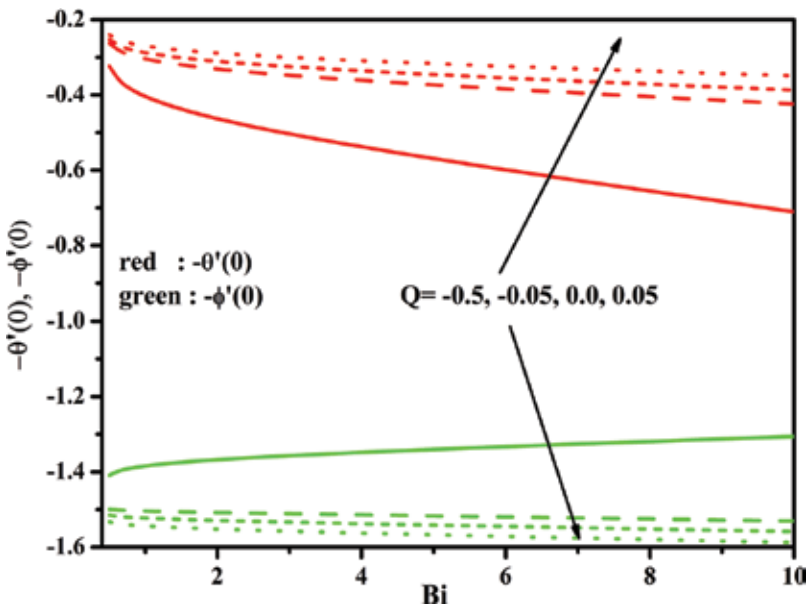

Figure 16. Variation of $-\theta'(0)$ and $-\phi'(0)$ with Bi for different values of Q.

http://dx.doi.org/10.5772/intechopen.74170

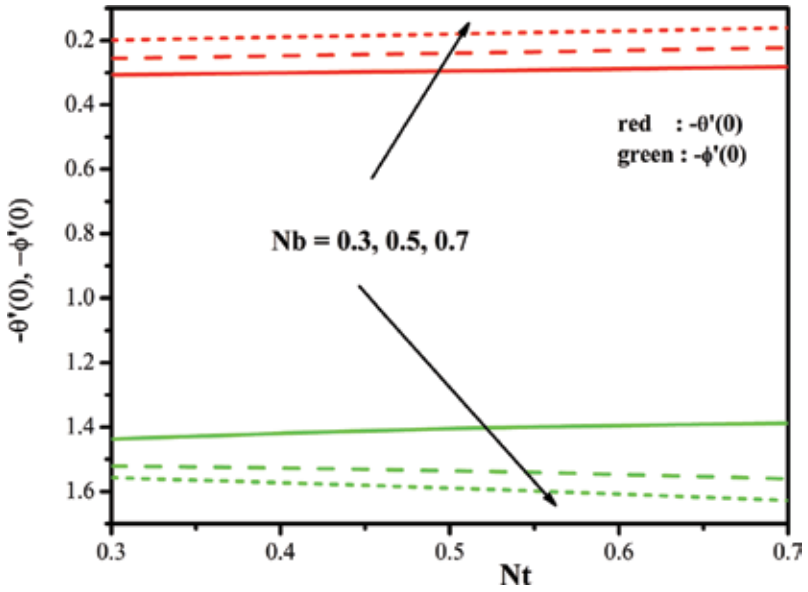

Figure 17. Variation of $-\theta'(0)$ and $-\phi'(0)$ with Nt for different values of Nb.

$\alpha = 1$, sheet will extended along the two bearings with a similar proportion (axisymmetric case), and third and last case identify with extending proportion parameter α other than 0 or 1; at that point, the flow conduct along both directions will be extraordinary.

Attributes of Forchheimer parameter (Fr) on $f'(\varsigma)$, $g'(\varsigma)$ is plotted in **Figure 3**. Obviously, $f'(\varsigma)$, $g'(\varsigma)$ is a diminishing capacity of Fr. **Figure 4** features the impact of Fr on $\theta(\varsigma)$, $\phi(\varsigma)$. Of course $\theta(\varsigma)$, $\phi(\varsigma)$ and related thickness of boundary layer are higher when Fr increments. **Figure 5** illustrates the varieties in $f'(\varsigma)$, $g'(\varsigma)$ for particular estimations of λ. Both $f'(\varsigma)$, $g'(\varsigma)$ and related layer thickness decay for larger λ. Physically, nearness of permeable media is to upgrade the protection from smooth movement which makes decay in fluid speed and thickness of energy boundary layer. **Figure 6** depicts the impact of λ on $\theta(\varsigma)$, $\phi(\varsigma)$. It is discovered that bigger λ causes an addition in $\theta(\varsigma)$, $\phi(\varsigma)$.

Figure 7 showed the impacts of non-Newtonian Casson fluid parameter (β) on velocity profiles $f'(\varsigma)$, $g'(\varsigma)$. It is seen that with the influence of β infers an abatement in the yield worry of the Casson fluid. This successfully encourages flow of the fluid, i.e., quickens the boundary layer flow near the extending surface, as appeared in **Figure 7**. In addition, it is found that with substantial estimations of β, the fluid is nearer to the Newtonian fluid. Truth be told, expanding estimations of the Casson fluid parameter β upgrade both temperature and nanoparticle division which is shown in **Figure 8**.

The variety in dimensionless temperature profile $\theta(\varsigma)$ with expanding estimations of generalized Prandtl number Pr is appeared through **Figure 9**. The temperature profile diminishes

with an expansion in the estimations of Prandtl number Pr, as Prandtl number is the proportion of energy diffusivity to thermal diffusivity. So, an expanding estimation of Prandtl number Pr infers a moderate rate of thermal dissemination which thus lessens the thermal boundary layer thickness. It can be directly seen that Prandtl number has more noticeable impact on Newtonian liquid when contrasted with non-Newtonian liquid.

Figure 10 displays the temperature $\theta(\varsigma)$ and the nanoparticle division $\phi(\varsigma)$ for variable estimations of Brownian movement *Nb*. The fluid velocity is found to increment with expanding *Nb*, while in nanoparticle fraction decreases as *Nb* expansion which consequently improves the nanoparticle's concentration at the sheet. This might be because of the way the Brownian movement parameter diminishes the mass exchange of a nanofluid. The diagram of thermophoresis parameter *Nt* on the temperature $\theta(\varsigma)$ and the nanoparticle part $\phi(\varsigma)$ profiles is portrayed in **Figure 11**. From these plots, it is seen that the impact of expanding estimations of *Nt* is to build the temperature and nanoparticle fraction.

Figure 12 shows the impact of Lewis number *Le* on temperature $\theta(\varsigma)$ and the nanoparticle portion $\phi(\varsigma)$ profiles. It is take note of that the temperature of the liquid increments however nanoparticle portion of the fluid diminishes with increment in *Le*. Physically truth that the bigger estimations of Lewis number makes the mass diffusivity littler, subsequently it diminishes the fixation field. The impacts of heat source/sink parameter *Q* can be found in **Figure 13**. For $Q > 0$ (heat source), it can be seen that the thermal boundary layer produces the vitality, and this causes the temperature in the thermal boundary layer increments with increment in *Q*. Though $Q < 0$ (heat sink) prompts diminish in the thermal boundary layer. $Q = 0$ speaks to the nonattendance of heat source/sink.

Impacts of the Biot number (*Bi*) on temperature are shown in **Figure 14**. Physically, the Biot number is communicated as the convection at the surface of the body to the conduction inside the surface of the body. At the point when thermal angle is connected at first glance, the proportion representing the temperature inside a body fluctuates significantly, while the body heats or cools over a period. Regularly, for uniform temperature field inside the surface, we consider $Bi << 1$. In any case, $Bi >> 1$ portrays that temperature field inside the surface is not uniform. In **Figure 14**, we have examined the impacts of Biot number *Bi* on the temperature and nanoparticle portion profiles in two ways. The first one is the situation.

when $Bi < 1$. It is seen from **Figure 14** that for the littlest estimations of the Biot number $Bi < 1$, the variety of temperature inside the body is slight and can sensibly be approximated as being uniform. While in the second case, $Bi > 1$ delineates that the temperature inside the body is not performing a uniform conduct (see **Figure 14**).

The impact of physical parameter on nearby Nusselt $-\theta'(0)$ and Sherwood number $-\phi'(0)$ is displayed in **Figure 15**. We can see through **Figure 15** that non-Darcy-Forchheimer connection creates the low heat and mass at the divider when contrasted with the Darcy-Forchheimer connection. Thus, it is seen with an expansion of the two reasons for speeding up in the λ and Fr. From **Figure 16**, the expanding estimations of the heat source/sink parameter (Q) improve the local Nusselt number $-\theta'(0)$ and decrease the local Sherwood number $-\phi'(0)$ with Bi . A similar conduct is likewise found for the variety in *Nt* and *Nb* which is portrayed in **Figure 17**.

4. Conclusions

Three-dimensional flow of Casson nanoliquid within the sight of Darcy-Forchheimer connection, uniform warmth source/sink, and convective type boundary condition is considered. Numerical plan prompts the arrangements of physical marvel. From this investigation, we analyzed that the expanding Casson parameter compares to bring down velocity and higher temperature fields. The nearness of Fr and λ caused a lessening in velocity and increasing speed on temperature and nanoparticle portion. The bigger Biot number improved the temperature and nanoparticle division. Additionally, for vast estimations of Biot number, there are no noteworthy changes in $-\theta'(0)$ and $-\phi'(0)$, which are available in **Table 3**. In heat exchange issues, heat sink parameter controls the relative thickening of the force and the thermal boundary layers.

Bi	$-\theta'(0)$	$-\phi'(0)$
0.1	0.084997	1.521377
0.5	0.239615	1.532624
2	0.324388	1.568759
5	0.343057	1.582440
10	0.349174	1.587619
50	0.353999	1.591990
100	0.354597	1.592550
500	0.355075	1.593001
1000	0.355134	1.593057
5000	0.355182	1.593102
10,000	0.355188	1.593108
100,000	0.355193	1.593113
1,000,000	0.355194	1.593113
5,000,000	0.355194	1.593114

Table 3. Computational values of local Nusselt number and local Sherwood number for several values of Bi.

Author details

Gosikere Kenchappa Ramesh

Address all correspondence to: gkrmaths@gmail.com

Department of Mathematics, School of Engineering, Presidency University, Bengaluru, Karnataka, India

References

[1] Crane LJ. Flow past a stretching plate. Zeitschrift für angewandte Mathematik und Physik. 1970;**21**(4):645-647. DOI. org/10.1007/BF01587695

[2] Grubka LG, Bobba KM. Heat transfer characteristics of a continuous stretching surface with variable temperature. Journal of Heat Transfer. 1985;**107**(1):248-250. DOI: 10.1115/1.3247387

[3] Ali ME. Heat transfer characteristics of a continuous stretching surface. Heat and Mass Transfer. 1994;**29**(4);227-234. DOI.org/10.1007/BF01539754

[4] Gupta PS, Gupta AS. Heat and mass transfer on a stretching sheet with suction or blowing. Canadian Journal of Chemical Engineering. 1977;**55**:744746. DOI: 10.1002/cjce.5450550619

[5] Gireesha BJ, Ramesh GK, Subhas Abel M, Bagewadi CS. Boundary layer flow and heat transfer of a dusty fluid flow over a stretching sheet with non-uniform heat source/sink. International Journal of Multiphase Flow. 2011;**37**(8):977-982. DOI.org/10.1016/J.Ijmultiphaseflow.2011.03.014

[6] Ramesh GK, Gireesha BJ. Flow over a stretching sheet in a dusty fluid with radiation effect. ASME Journal of Heat transfer. 2013;**135**(10):102702(1-6). DOI: 10.1115/1.4024587

[7] Bataller RC. Radiation effects for the Blasius and Sakiadis flows with a convective surface boundary condition. Applied Mathematics and Computation. 2008;**206**:832-840. DOI.ORG/10.1016/J.AMC.2008.10.001

[8] Gorla RSR, Sidawi I. Free convection on a vertical stretching surface with suction and blowing. Applied Science Research. 1994;**52**:247-257. DOI.org/10.1007/BF00853952

[9] Ochoa MV. Analysis of drilling fluid rhelogy and tool joint effects to reduce errors in hydraulics calculations [thesis]. Texas A&M University; 2006

[10] Nadeem S, Rizwan Ul Haq, Lee C. MHD flow of a Casson fluid over an exponentially shrinking sheet. Scientia Iranica B. 2012;**19**(6):1550-1553. DOI.ORG/10.1016/J.SCIENT.2012.10.021

[11] Mukhopadhyay S. Casson fluid flow and heat transfer over a nonlinearly stretching. Chinese Physics B. 2013;**22**(7):074701. DOI.ORG/10.1088/1674-1056/22/7/074701

[12] Hayat T, Shehzad SA, Alsaedi A, Alhothuali MS. Mixed convection stagnation point flow of casson fluid with convective boundary conditions. Chinese Physical Letter. 2012;**29**(11);114704. DOI.org/10.1088/0256-307x/29/11/114704

[13] Ramesh GK, Ganesh Kumar K, Shehzad SA, Gireesha BJ. Enhancement of radiation on hydromagnetic Casson fluid flow towards a stretched cylinder with suspension of liquid-particles. Canadian Journal of Physics. 2018;**96**(1);18-24. DOI.ORG/10.1139/CJP-2017-0307

[14] Maity S, Singh SK, Kumar AV. Unsteady three dimensional flow of Casson liquid film over a porous stretching sheet in the presence of uniform transverse magnetic field and suction/injection. Journal of Magnetism and Magnetic Material. 2016;**419**:292-300. DOI. ORG/10.1016/J.JMMM.2016.06.004

[15] Nadeem S, Haq RU, Akbar NS, Khan ZH. MHD three-dimensional Casson fluid flow past a porous linearly stretching sheet. Alexandria Engineering Journal. 2013;**52**:577-582. DOI. ORG/10.1016/J.AEJ.2013.08.005

[16] Ahmad K, Nazar R. Magnetohydrodynamic three dimensional flow and heat transfer over a stretching surface in a viscoelastic fluid. Journal of Science and Technology. 2011; **3**(1):33-46

[17] Ramesh GK, Gireesha BJ, Shehzad SA, Abbasi FM. Analysis of heat transfer phenomenon in magnetohydrodynamic Casson fluid flow through Cattaneo-Christov heat diffusion theory. Communications in Theoretical Physics. 2017;**68**:91-95. DOI.ORG/10.1088/ 0253-6102/68/1/91

[18] Mustafa M, Hayat T, Pop I, Aziz A. Unsteady boundary layer flow of a Casson fluid due to an impulsively started moving flat plate. Heat Transfer-Asian Research. 2011;**40**(6): 563-576. DOI: 10.1002/htj.20358

[19] Buongiorno J. Convective transport in nanofluids. ASME Journal of Heat transfer. 2006; **128**:240-250. DOI: 10.1115/1.2150834

[20] Ahn HS, Kim MH. A review on critical heat flux enhancement with nanofluids and surface modification. Journal of Heat Transfer. 2012;**134**:024001. DOI: 10.1115/1.4005065

[21] Makinde OD, Aziz A. Boundary layer flow of a nanofluid past a stretching sheet with a convective boundary condition. International Journal of Thermal Science. 2011;**50**: 1326-1332. DOI.ORG/10.1016/J.IJTHERMALSCI.2011.02.019

[22] Hsiao KL. Nanofluid flow with multimedia physical features for conjugate mixed convection and radiation. Computers and Fluids. 2014;**104**:1-8. DOI.ORG/10.1016/J. COMPFLUID.2014.08.001

[23] Kuznetsov AV, Nield DA. Natural convective boundary layer flow of a nanofluid past a vertical plate: A revised model. International Journal of Thermal Science. 2014;**77**: 126-129. DOI.ORG/10.1016/J.IJTHERMALSCI.2013.10.007

[24] Hayat T, Muhammad T, Alsaedi A, Alhuthali MS. Magnetohydrodynamic three dimensional flow of viscoelastic nanofluid in the presence of nonlinear thermal radiation. Journal of Magnetism and Magnetic Materials. 2015;**385**:222-229. DOI.ORG/10.1016/J. JMMM.2015.02.046

[25] Ramesh GK, Roopa GS, Gireesha BJ, Shehzad SA, Abbasi FM. An electro-magnetohydrodynamic flow Maxwell nanoliquid past a Riga plate: A numerical study. Journal of the Brazilian Society of Mechanical Sciences and Engineering. 2017;**39**(11):4547-4554. DOI.org/10.1007/s40430-017-0900-z

[26] Ramesh GK, Prasannakumara BC, Gireesha BJ, Shehzad SA, Abbasi FM. Three dimensional flow of Maxwell nanofluid past a bidirectional porous stretching surface with thermal radiation. Thermal Science and Engineering Progress. 2017;**1**:6-14. DOI.ORG/10.1016/J.TSEP.2017.02.006

[27] Ramesh GK, Gireesha BJ. Influence of heat source/sink on a Maxwell fluid over a stretching surface with convective boundary condition in the presence of nanoparticles. Ain Shams Engineering Journal. 2014;**5**:991-998. DOI.ORG/10.1016/J.ASEJ.2014.04.003

[28] Forchheimer P. Wasserbewegung durch boden. Zeitschrift des Vereins deutscher Ingenieure. 1901;**45**:1782-1788

[29] Muskat M. The Flow of Homogeneous Fluids Through Porous Media. New York: McGraw Hill; 1937

[30] Pal D, Mondal H. Hydromagnetic convective diffusion of species in Darcy-Forchheimer porous medium with non-uniform heat source/sink and variable viscosity. International Communication in Heat and Mass Transfer. 2012;**39**:913-917. DOI.ORG/10.1016/J.ICHEATMASSTRANSFER.2012.05.012

[31] Hayat T, Muhammad T, Al-Mezal S, Liao SJ. Darcy-Forchheimer flow with variable thermal conductivity and Cattaneo-Christov heat flux. International Journal of Numerical Methods for Heat and Fluid Flow. 2016;**26**:2355-2369. DOI.ORG/10.1108/HFF-08-2015-0333

[32] Vishnu Ganesh N, Abdul Hakeem AK, Ganga B. Darcy–Forchheimer flow of hydromagnetic nanofluid over a stretching/shrinking sheet in a thermally stratified porous medium with second order slip, viscous and Ohmic dissipations effects. Ain Shams Engineering Journal. 2016. DOI.ORG/10.1016/J.ASEJ.2016.04.019 (In press)

[33] AdilSadiq M, Hayat T. Darcy–Forchheimer flow of magneto Maxwell liquid bounded by convectively heated sheet. Results in Physics. 2016;**6**:884-890. DOI.ORG/10.1016/J.RINP.2016.10.019

[34] Ishak A, Nazar R, Pop I. Magnetohydrodynamic (MHD) flow and heat transfer due to a stretching cylinder. Energy Conversion and Management. 2008;**49**:3265-3269. DOI.ORG/10.1016/J.ENCONMAN.2007.11.013

[35] Pal D, Mondal H. Influence of chemical reaction and thermal radiation on mixed convection heat and mass transfer over a stretching sheet in Darcian porous medium with Soret and Dufour effects. Energy Conversion and Management. 2012;**62**:102-108. DOI.ORG/10.1016/J.ENCONMAN.2012.03.017

Section 2

Mass Transfer in Multiphase Flow

Chapter 4

Modelling of Bubbly Flow in Bubble Column Reactors with an Improved Breakup Kernel Accounting for Bubble Shape Variations

Weibin Shi, Jie Yang, Guang Li, Yuan Zong and Xiaogang Yang

Additional information is available at the end of the chapter

http://dx.doi.org/10.5772/intechopen.76448

Abstract

Bubble shapes have been assumed to be spherical in the currently available breakup models such as the one developed by Luo and Svendsen (1996). This particular breakup model has been widely accepted and implemented into CFD modelling of gas-liquid two-phase flows. However, simulation results obtained based on this model usually yield unreliable predictions about the breakage of very small bubbles. The incorporation of bubble shape variation into breakup models has rarely been documented in the study but the bubble shape plays an important role when considering the interactions with the surrounding turbulent eddies in turbulent bubbly flows, especially when the effects of bubble deformation, distortion and bubble internal pressure change are considered during the events of eddy-bubble collision. Thus, the assumption of spherical bubbles seems to be no longer appropriate in reflecting this phenomenon. This study proposes and implements an improved bubble breakup model, which accounts for the variation of bubble shapes when solving the population balance equations for CFD simulation of gas-liquid two-phase flows in bubble columns.

Keywords: bubble column CFD simulation, breakup model, bubble shape variations, interfacial area, mass transfer coefficient

1. Introduction

Previous CFD studies have employed the assumption of a unified bubble diameter, which can generate reliable predictions if the bubble size distribution is very narrow. However, numerical modelling of gas-liquid two-phase flow behaviors should also take into account scenarios

where wide bubble size distributions and eddy/bubble-bubble interactions exist. These are very influential factors in the calculation of the gas-liquid interfacial area, which in turn affects the prediction of the mass and heat transfer between the two phases. By solving the population balance equations (PBEs) during the numerical simulation, the bubble size distribution can be derived directly, while the behaviour of the eddy/bubble-bubble interactions can be reflected within coalescence and breakup models.

For the process of bubble breakup, Coulaloglou and Tavlarides [1] assumed that the breakup process would only occur if the energy from turbulent eddies acting on the fluid particle was more than the surface energy it contains. Prince and Blanch [2] acknowledged that bubble breakup is caused by eddy-bubble collision and proposed that bubble breakup can only be induced by eddies with approximately the same characteristic length. For instance, eddies at a much larger length scale transports the bubbles without causing any breakups. Luo and Svendsen [3] described the bubble breakup process by considering both the length scale and the amount of energy contained in the arriving eddies. The minimum length scale of eddies that are responsible for the breakup process is equivalent to 11.4 times the Kolmogorov scale. The critical probability of bubble breakup is related to the ratio of surface energy increase of bubbles after breakup to the mean turbulent kinetic energy of the colliding eddy. Therefore, very small eddies do not contain sufficient energy to cause the bubble breakup process. Lehr et al. [4] proposed a slightly different breakup mechanism from Luo and Svendsen [3] by considering the minimum length scale of eddies to be determined by the size of the smaller bubble after breakup. They also specified that the breakup process is dependent on the inertial force of the arriving eddy and the interfacial force of the bubble. Based on the results of Luo and Svendsen [3] and Lehr et al. [4], Wang et al. [5] proposed an energy constraint and capillary constraint criteria for the breakup model. The energy constraint requires the eddy energy to be greater than or equal to the increase of surface energy of bubbles after the breakage has occurred. The capillary constraint requires the dynamic pressure of the eddy to exceed the capillary pressure of the bubble. The use of these two breakup criteria has restricted the occurrence of breakage that generates unphysically small daughter bubbles and demonstrated more reliable results than that of Luo and Svendsen [3]. Similar ideas to those of Wang et al. [5] have also been adopted by Zhao and Ge [6], Andersson and Andersson [7] and Liao et al. [8]. A more concise breakup constraint of energy density increase was proposed by Han et al. [9]. The constraint of energy density increase involves only one term, which is the energy density itself, to represent what was originally expressed by two terms: capillary pressure and surface energy. It was shown that the energy density increase during the entire breakup process should not exceed the energy density of the parent bubble.

Incorporation of a bubble shape variation into the breakup model has rarely been documented in the open literature. Therefore, the aim of this study is to consider the influence of bubble shape variation on the bubble breakage process in bubble column flows. A breakage model accounting for the variation of bubble shapes, coupled with the breakage criterion of energy density increase, is proposed here.

http://dx.doi.org/10.5772/intechopen.76448

2. Mathematical modelling

2.1. Bubble size distribution

The bubble size distribution is determined by employing the population balance model with a consideration of bubble coalescence and breakup. Bubbles are divided into several size groups with different diameters specified by the parameter $d_{eq,i}$ and an equivalent phase with the Sauter mean diameter to represent the bubble classes. In this study, 16 bubble classes with diameters ranging from 1 to 32 mm are applied based on the geometric discretization method where $V_i = 2V_{i-1}$. The population balance equation is expressed by Eq. (1)

$$\frac{\partial n_i}{\partial t} + \nabla \cdot \left(\vec{v}_i \cdot n_i\right) = S_i \tag{1}$$

where n_i is the number density for i-th group, $\vec{v_i}$ is the mass average velocity vector and S_i is the source term.

The source term for the i-th group, S_i, can be thought of as the birth and death of bubbles due to coalescence and breakup, respectively. The expression for this particular term is given by Eq. (2)

$$\begin{aligned} S_i &= B_{coalescence,\,i} - D_{coalescence,\;\;i} + B_{breakup,\,i} - D_{breakup,\,i} \\ &= \sum_{d_{eq,j}=d_{eq,\min}}^{d_{eq,i}/2} \Omega_C\left(d_{eq,j} : d_{eq,i} - d_{eq,j}\right) - \sum_{d_{eq,j}}^{d_{eq,\max}-\,d_{eq,i}} \Omega_C\left(d_{eq,j} : d_{eq,i}\right) + \sum_{d_j=d_i}^{d_{\max}} \Omega_B\left(d_{eq,j} : d_{eq,i}\right) - \Omega_B\left(d_{eq,i}\right) \end{aligned} \tag{2}$$

The local gas volume fraction can be calculated using Eq. (3),

$$\alpha_g f_i = n_i V_i \tag{3}$$

where f_i is the i-th class fraction of the total volume fraction and V_i is the volume for the i-th class.

To describe the coalescence between two bubbles, the coalescence kernel proposed by Luo [10] was utilized in this study. As this is not the main concern of this work, further details of the coalescence kernel can be found in Luo's paper.

The breakup model proposed in this study is based on the work of Luo and Svendsen [3]. Several improvements have been introduced in this study to produce a more realistic breakup model. In Luo and Svendsen's model, the shape of breakage bubbles was assumed to be spherical. However, the experimental studies and statistical results, such as Grace et al. [11] and Tomiyama [12], have found that bubbles exist in various shapes and the dynamics of bubble motion strongly depend on the shape of the bubbles. For example, **Figure 1** shows the

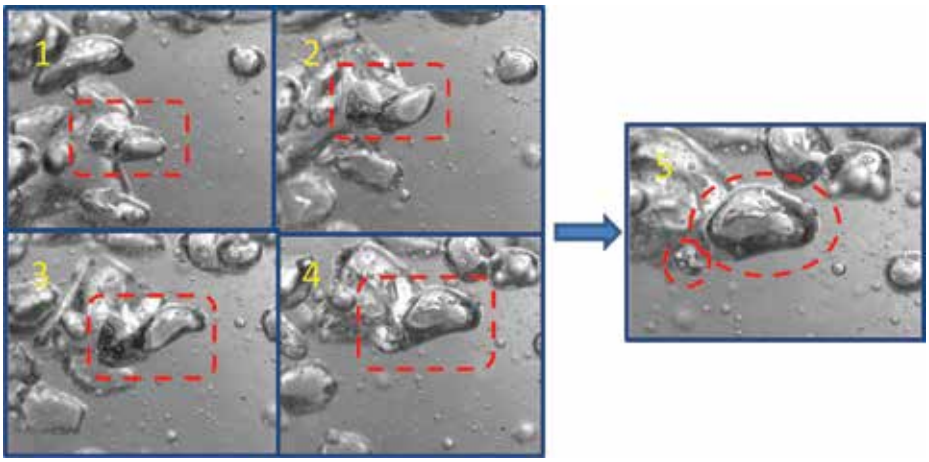

Figure 1. Time sequence photos of the breakup of a rising bubble in a 150-mm diameter cylindrical bubble column (Ug = 0.02 m/s; total duration: 0.0366 s).

experimentally recorded breakup process of a spherical-cap bubble found in an operating bubble column used in an ongoing research project funded by the Natural Science Foundation of China (NSFC). The spherical-cap bubble is colliding with a bombarding eddy that was generated as a consequence of shedding eddy from the preceding bubbles. The spherical-cap bubble then becomes deformed and distorted and finally breaks into two ellipsoidal bubbles. This phenomenon may lead to two major implications. Firstly, the shed eddies that interact with subsequently formed bubbles are mainly induced by the presence of preceding bubbles. These shed eddies dissipate mainly due to the viscous influence and they will decay downstream in a slightly short distance. Thus, these eddies will have the size the same order as the preceding bubbles. This kind of bubble-induced turbulence may exhibit different dynamic behaviour as can be distinguished from the typical Kolmogorov −5/3 law on the turbulence kinetic energy spectrum. It should be pointed here with caution that more fundamental investigations are required to reveal the interactions between the eddy generated by bubble-induced turbulence and the bubbles, and the impact of this interaction on the bubble breakage process. Secondly, although the bubble shape has been assumed to be spherical in the previous studies for the simplification of models, the variation of bubble shapes could potentially become a critical factor for better prediction of the bubbly flow characteristics of the gas phase in CFD simulations, because the type of geometrical shape has a strong impact on the surface energy of bubbles and interfacial area.

From experimental observations, bubble shapes can be classified into different types. Thus, the effects of different bubble shapes are taken into account in this study. However, due to the uncertainty of the spatial orientation of the bubbles during their movement, the determination of the contact angle of the bombarding eddy is very difficult but this needs to be tackled as the contact angle will directly affect the projection/sweep area of the eddy-bubble collision tube. On the contrary, if the bubble that is about to breakup is assumed to be spherical, the projection/sweep area of the collision tube will be consistent no matter which direction of the bombarding eddy comes from. Instead of using the original bubble size $d_{eq,i}$ to construct the

collision tube, a nominal diameter, d_V, that approximately represents the size of the projected area of the bubble, is defined in a bounded range given by expression (4),

$$c \le d_V \le a \tag{4}$$

where c and a are the length of the short axis and long axis, respectively. The new imaginary collision tube is presented in **Figure 2**.

The breakup rate for one individual parent bubble that forms into two daughter bubbles can be calculated using Eq. (5),

$$\Omega_B = \int_{\lambda_{\min}}^{d} \omega_B^T p_B \; d\lambda \tag{5}$$

where ω_B^T is the collision probability density, which can be estimated from Luo and Swendsen [3], as defined by Eq. (6)

$$\omega_B^T(\xi) = 0.923(1-\alpha_g)\left(\varepsilon d_{eq,i}\right)^{1/3} n_i \frac{\left(d_{V,s}/d_{eq,i}+\xi\right)\left(d_{V,l}/d_{eq,i}+\xi\right)}{d_{eq,i}^2 \xi^{11/3}} \tag{6}$$

Here, $\xi = \lambda / d_{eq,i}$ is the non-dimensional size of eddies that may contribute to the breakage of bubbles with size d_i. The breakage probability function p_B used by Luo and Svendsen [3] is given by Eq. (7),

$$p_B = \exp\left(-\frac{e_s}{\bar{e}}\right) \tag{7}$$

where $\bar{e}$ is the mean turbulent kinetic energy for eddies of size λ and e_s is the increase in surface energy of bubbles after breakage. The mean turbulent kinetic energy can be determined by Eq. (8)

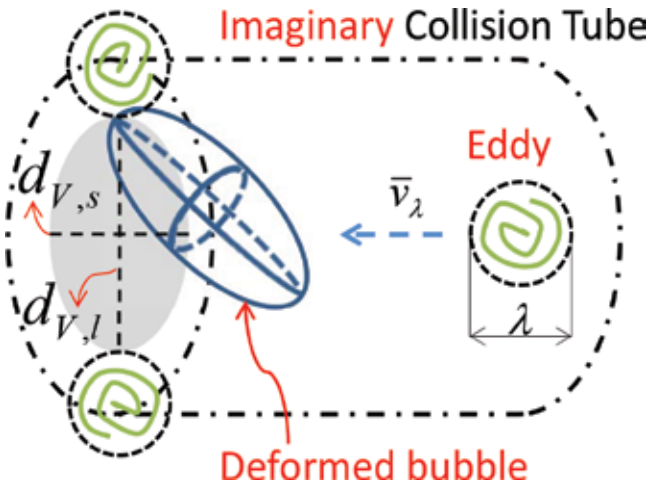

Figure 2. Diagram showing an eddy entering a collision tube and moving through it with a mean velocity.

$$\frac{\bar{e} = \rho_l \frac{\pi}{6} \lambda^3 \overline{u}_\lambda^2}{2 = \frac{\pi\beta}{12} \rho_l \left(\varepsilon d_{eq,i}\right)^{2/3} d_{eq,i}^3 \xi^{11/3}} \tag{8}$$

By assuming the bubbles before and after breakage have deformed shapes with an equivalent diameter, when the parent bubble of size $d_{eq,i}$ breaks into two bubbles of size $d_{eq,j}$ and $(d_{eq,i}{}^3\text{-}d_{eq,j}{}^3)^{1/3}$, the increase in surface energy can be estimated using Eq. (9),

$$e_s\left(d_{eq,i}, d_{eq,j}\right) = \sigma \cdot \pi d_{eq,i}^2 \left[f_V^{2/3} + \left(1 - f_V\right)^{2/3} - 1\right] \tag{9}$$

where the breakage volume fraction is given by $f_V = d_{eq,j}^3 / d_{eq,i}^3$. Since the effects of different shapes of bubbles are now taken into account, Eq. (9) can be rewritten in a general form in terms of the surface area of the bubbles, S, as defined by Eq. (10)

$$e_s = \sigma \cdot \left(S_{j,1} + S_{j,2} - S_i\right) \tag{10}$$

Although there have been some recent developments on the instability of bubble shapes, such as the studies by Cano-Lozano et al. [13], Zhou and Dusek [14] and Tripathi et al. [15], there is no consensuses on concise definitions on bubble shapes and bubble shape model. Therefore, a more commonly accepted statistical model of bubble shapes by Tomiyama [12] has been employed in this study. In addition, the lift model described by Tomiyama [12] has been adopted as it has been well implemented by different commercial CFD packages. According to the criteria proposed by Tomiyama [12] and Tomiyama et al. [16], there are three main types of bubble shapes that should be considered in the bubble columns of this study. These shapes include spherical, ellipsoidal and spherical-capped bubbles. These three types of bubble shapes may also be considered for modelling gas-liquid two-phase flow or gas-liquid-solid three-phase flow in bubble columns with similar scales that operate at similar conditions to what is applied in this work. The details of these three types of bubble shapes and their potential breakage scenarios are depicted in **Figure 3**.

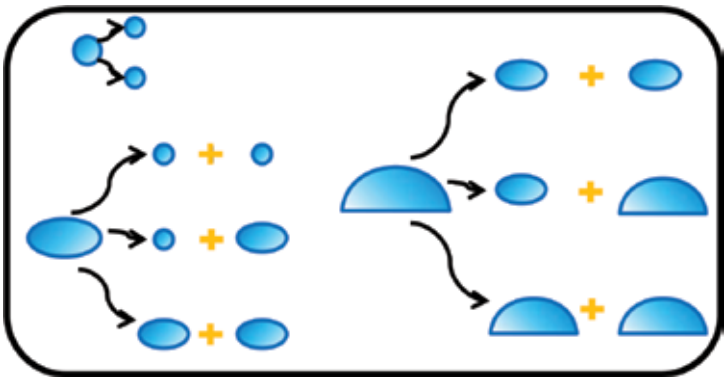

Figure 3. Classification of the three types of bubble shapes and the possible breakage scenarios.

For an air-water system under atmospheric pressure and room temperature conditions, the size boundary to categorize between spherical and ellipsoidal bubbles represented by $d_{eq,1}$ is roughly 1.16 mm for the pure system and approximately 1.36 mm for a slightly contaminated system. It is very important to point out that the volumes of ellipsoidal bubbles and spherical-cap bubbles should be equal to the volumes of their equivalent spherical bubbles with diameter d_{eq}. For bubbles with ellipsoidal shapes, by assuming an oblate type of ellipsoid, the surface area can be calculated using Eq. (11),

$$S_{ellipsoid} = \frac{\pi}{2} d_{eq}^2 E^{1/3} \left(1 + \frac{1}{2E\sqrt{E^2-1}} \ln\left(2E^2 - 1 + 2E\sqrt{E^2-1} \right) \right) \tag{11}$$

where the aspect ratio E can be expressed using the empirical correlation described by Wellek et al. [17], which is given by Eq. (12)

$$E = a/b = 1 + 0.163 Eo^{0.757} \tag{12}$$

Here, Eo is the Eötvös number as defined by Eq. (13)

$$Eo = \frac{g\left(\rho_l - \rho_g\right) d_{eq}^2}{\sigma} \tag{13}$$

The size boundary to divide between ellipsoidal and spherical-cap bubbles represented by d_C is estimated using Eq. (14),

$$d_C = \sqrt{{}^{40\sigma}/_{g\left(\rho_L - \rho_g\right)}} \tag{14}$$

where d_c is determined to be 17.3 mm for the air-water system. For a single spherical-cap bubble, the wake angle θ_W is assumed to be 50° based on the work of Tomiyama [12]. As the volume of the spherical-cap bubble is equivalent to the volume of the spherical bubble, Eq. (15) can be formulated as follows:

$$R_S^3 = \frac{\pi d_{eq}^3 / 6}{\left(1 - \cos\theta_W\right)^2 - \left(1 - \cos\theta_W\right)^3 / 3} \tag{15}$$

The curved surface area for the front edge can be calculated from the following relationship given by Eq. (16):

$$S_{Cap} = 2\pi R^2 (1 - \cos\theta_W) \tag{16}$$

The experimental observations of Davenport et al. [18] and Landel et al. [19] have clearly indicated that the rear surface of a single spherical-cap bubble follows a constantly oscillating lenticular shape, resulting from external perturbations acting on the rear surface. This lenticular shaped rear surface can be considered to be essentially flat, and the surface energy increase required to breakup the surface can be neglected based on the consideration that when any

arriving eddies bombard the flat surface, the energy resulting from the surface tension force action will be far smaller than the kinetic energy exuded by the turbulent eddies. It should be noted with caution that these are rough approximations, and more complicated crown bubble systems are not considered in this work. The influence of the variation of bubble shapes on the increase in surface energy is further illustrated in **Figure 7**.

The breakup model proposed by Luo and Svendsen [3] only considered the surface energy requirement for breakup events but it should be noted that bubble breakage may also be subjected to the pressure head difference of the bubble and its surrounding eddies, especially when the breakage volume fraction is small. Therefore, on the basis of the interaction force balance proposed by Lehr et al. [4], the pressure energy requirement also needs to be considered as a competitive breakup mechanism. This can be imposed as a constraint. The same idea has been adopted by Zhao and Ge [6], Liao et al. [8] and Guo et al. [20]. The pressure energy requirement can be expressed using Eq. (17),

$$e_P = \frac{\sigma}{\min\left(R_{C,j}, R_{C,k}\right)} \cdot \frac{\pi\left(\min\left(d_{eq,j}, d_{eq,k}\right)\right)^3}{6} \tag{17}$$

where $R_{C,j}$ and $R_{C,k}$ are the equivalent radius of curvature of daughter bubbles. The theoretical prediction of the surface energy and pressure energy requirement is shown in **Figure 6**.

As pointed out by Han et al. [21], from a volume-based energy perspective, the surface energy density of the parent bubble should always exceed the maximum value of the energy density increase during the entire breakup process. This is an important breakup criterion that has been adopted in this study and concurrently relates the size of the parent bubble to the sizes of the daughter bubbles. This restricts the generation of very small bubbles from the breakup process because the energy densities of the daughter bubbles will tend towards infinity when their sizes tend to zero. The energy density criterion can be expressed by Eq. (18) if it is coupled with the variation of bubble shapes

$$6\sigma S_i \Big/ \pi d_{eq,i}^3 \geq 6\sigma \cdot \max\left(S_j / \pi d_{eq,j}^3, S_k / \pi d_{eq,k}^3\right) - 6\sigma S_i \Big/ \pi d_{eq,i}^3 \tag{18}$$

The breakup frequency can be obtained by substituting Eqs. (6)–(17) into Eq. (5), which results in Eq. (19),

$$\Omega_B = \begin{cases} 0.923\left(1-\alpha_g\right) n_i \left(\varepsilon / d_{eq,i}^2\right)^{1/3} \cdot \int_{\xi_{\min}}^1 \dfrac{\left(d_{V,s}/d_{eq,i}+\xi\right)\left(d_{V,l}/d_{eq,i}+\xi\right)}{\xi^{11/3}} \exp\left(-\dfrac{12\sigma\left(S_j+S_k-S_i\right)}{\pi\beta\rho_l\varepsilon^{2/3}\xi^{11/3}d_{eq,i}^{11/3}}\right) d\xi, \\ \qquad when \quad \dfrac{6\sigma\left(S_j+S_k-S_i\right)}{\pi d_{eq,i}^3} \geq \dfrac{\sigma}{\min\left(Rc_j, Rc_k\right)} \\ 0.923\left(1-\alpha_g\right) n_i \left(\varepsilon / d_{eq,i}^2\right)^{1/3} \cdot \int_{\xi_{\min}}^1 \dfrac{\left(d_{V,s}/d_{eq,i}+\xi\right)\left(d_{V,l}/d_{eq,i}+\xi\right)}{\xi^{11/3}} \exp\left(-\dfrac{2\sigma\left(\min\left(d_{eq,j}, d_{eq,k}\right)\right)^3}{\min\left(Rc_j, Rc_k\right)\beta\rho_l\varepsilon^{2/3}\xi^{11/3}d_{eq,i}^{11/3}}\right) d\xi, \\ \qquad when \quad \dfrac{6\sigma\left(S_j+S_k-S_i\right)}{\pi d_{eq,i}^3} < \dfrac{\sigma}{\min\left(Rc_j, Rc_k\right)} \end{cases} \tag{19}$$

where $\xi_{\min}$ is the minimum breakage volume fraction that is able to satisfy the energy density criterion shown in Eq. (18).

2.2. Governing Eqs

A three-dimensional (3D) transient CFD model is employed in this work to simulate the local hydrodynamics of the gas-liquid two-phase bubble column. An Eulerian-Eulerian approach is adopted in order to describe the flow behaviors for both phases, that is, water as the continuous phase and air as the dispersed phase.

The mass and momentum balance equations are given by Eqs. (20) and (21), respectively,

$$\frac{\partial}{\partial t}(\rho_k \alpha_k) + \nabla \cdot (\rho_k \alpha_k \boldsymbol{u}_k) = \mathbf{0} \tag{20}$$

$$\frac{\partial}{\partial t}(\rho_k \alpha_k \boldsymbol{u}_k) + \nabla \cdot (\rho_k \alpha_k \boldsymbol{u}_k \boldsymbol{u}_k) = -\alpha_k \nabla p + \nabla \cdot \boldsymbol{\tau}_k + \alpha_k \rho_k \boldsymbol{g} + \boldsymbol{F}_k \tag{21}$$

where ρ_k, α_k, $\boldsymbol{u}_k$, $\boldsymbol{\tau}_k$ and $\boldsymbol{F}_k$ represent the density, volume fraction, velocity vector, viscous stress tensor and the interphase momentum exchange term for the k (liquid or gas) phase, respectively. The sum of the volume fractions for both phases is equal to 1.

A modified $k\tilde{}\varepsilon$ turbulence model with the consideration of bubble-induced turbulence by Sato and Sekoguchi [22] is used for turbulence closure. The turbulent kinetic energy k_l and dissipation rate ε_l are computed using Eqs. (22) and (23),

$$\frac{\partial}{\partial t}(\rho_i \alpha_i k_i) + \nabla \cdot (\rho_i \alpha_i k_i \boldsymbol{u}_i) = \nabla \cdot \left[\alpha_i \left(\mu_i + \frac{\mu_{eff,i}}{\sigma_k} \right) \nabla k_i \right] + \alpha_i (G_{k,i} - \rho_i \varepsilon_i) \tag{22}$$

$$\frac{\partial}{\partial t}(\rho_i \alpha_i \varepsilon_i) + \nabla \cdot (\rho_i \alpha_i \varepsilon_i \boldsymbol{u}_i) = \nabla \cdot \left[\alpha_i \left(\mu_i + \frac{\mu_{eff,i}}{\sigma_\varepsilon} \right) \nabla \varepsilon_i \right] + \alpha_i \frac{\varepsilon_i}{k_i} (C_{1\varepsilon} G_{k,i} - C_{2\varepsilon} \rho_i \varepsilon_i) \tag{23}$$

where $G_{k,l}$ is the production of turbulent kinetic energy and $\mu_{t,l}$ is the turbulent viscosity. In this work, the standard $k\tilde{}\varepsilon$ model constants used are $C_\mu = 0.09$, $C_{1\varepsilon} = 1.44$, $C_{2\varepsilon} = 1.92$, $\sigma_k = 1.0$, $\sigma_\varepsilon = 1.3$.

The effective viscosity is composed of the contributions of turbulent viscosity and an extra term considering the effect of bubble-induced turbulence and is defined by Eq. (24)

$$\mu_{eff,l} = \rho_l C_\mu \frac{k_l^2}{\varepsilon_l} + \rho_l C_{\mu,BIT} \alpha_g d_b |\boldsymbol{u}_g - \boldsymbol{u}_l| \tag{24}$$

The Sato coefficient $C_{\mu,BIT} = 0.6$ is adopted according to the study [22].

2.3. Interphase momentum transfer

In this study, drag force, lift force and added mass force are considered as the main interactions between the continuous liquid phase and the dispersed gas phase. The drag force is calculated using Eq. (25),

$$\boldsymbol{F}_D = \frac{3}{4} \frac{C_D}{d_{eq}} \rho_l \alpha_g |\boldsymbol{u}_g - \boldsymbol{u}_l| (\boldsymbol{u}_g - \boldsymbol{u}_l) \tag{25}$$

where C_D is the drag coefficient, which can be obtained from the model by Grace et al. [11]. The Grace model is well suited for gas-liquid flows in which the bubbles exhibit a range of shapes, such as sphere, ellipsoid and spherical-cap. However, instead of comparing the values of drag coefficients in the original Grace model, the drag coefficient can be applied directly into the present model as the variation of bubble shapes has been taken into account. The drag coefficients for the different shapes of bubbles are calculated using Eqs. (26)–(28),

$$C_{D,\,sphere} = \begin{cases} 24/\mathrm{Re}_b & \mathrm{Re}_b < 0.01 \\ 24\left(1 + 0.15\mathrm{Re}_b^{0.687}\right)/\mathrm{Re}_b & \mathrm{Re}_b \geq 0.01 \end{cases} \tag{26}$$

$$C_{D,\,cap} = \frac{8}{3} \tag{27}$$

$$C_{D,\,ellipse} = \frac{4}{3}\frac{g d_{eq}}{U_t^2}\frac{\left(\rho_l - \rho_g\right)}{\rho_l} \tag{28}$$

where Re_b is the bubble Reynolds number given by $\mathrm{Re}_b = \frac{\rho_l \left|\boldsymbol{u}_g - \boldsymbol{u}_l\right| d_{eq}}{\mu_l}$ and U_t is the terminal velocity calculated using Eq. (29),

$$U_t = \frac{\mu_l}{\rho_l d} Mo^{-0.149}(J - 0.857) \tag{29}$$

Here, Mo is the Morton number defined by $Mo = \frac{\mu_l^4 g\left(\rho_l - \rho_g\right)}{\rho_l^2 \sigma^3}$ and J is determined by the piecewise function calculated using the empirical expression (30)

$$J = \begin{cases} 0.94H^{0.757} & 2 < H < 59.3 \\ 3.42H^{0.441} & H > 59.3 \end{cases} \tag{30}$$

H in expression (30) is defined by Eq. (31),

$$H = \frac{4}{3} EoMo^{-0.149}\left(\frac{\mu_l}{\mu_{ref}}\right)^{-0.14} \tag{31}$$

where Eo is the Eötvös number and $\mu_{ref} = 0.0009\ \ kg/(m \cdot s)$.

The lift force acting perpendicular to the direction of relative motion of the two phases can be calculated by using Eq. (32)

$$\boldsymbol{F}_{Lift} = C_L \rho_l \alpha_g \left(\boldsymbol{u}_g - \boldsymbol{u}_l\right) \times (\nabla \times \boldsymbol{u}_l) \tag{32}$$

where C_L is the lift coefficient and is estimated by the Tomiyama lift force correlation [12], as described by the following empirical relation (33),

$$C_L = \begin{cases} \min\left[0.288\tanh(0.121\mathrm{Re}_b), f\left(Eo'\right)\right] & Eo' \le 4 \\ f\left(Eo'\right) & 4 < Eo' < 10 \\ -0.29 & Eo' > 10 \end{cases} \tag{33}$$

where $f\left(Eo'\right) = 0.00105Eo'^3 - 0.0159Eo'^2 - 0.0204Eo' + 0.474$. Eo' is the modified Eötvös number based on the maximum horizontal dimension of the deformable bubble, d_h, as defined and given, respectively, by Eqs. (34) and (35)

$$Eo' = \frac{g\left(\rho_l - \rho_g\right)d_h^2}{\sigma} \tag{34}$$

$$d_h = d\left(1 + 0.163Eo^{0.757}\right)^{1/3} \tag{35}$$

The virtual mass force is also significant when the gas phase density is smaller than the liquid phase density. The estimation of the virtual mass force due to the deformation of bubbles is one of the unresolved issues that require further investigation. With the caution, the virtual mass force is still calculated using Eq. (36),

$$\boldsymbol{F}_{VM} = C_{VM}\rho_l\alpha_g\left(\frac{d\boldsymbol{u}_l}{dt} - \frac{d\boldsymbol{u}_g}{dt}\right) \tag{36}$$

where C_{VM} is the virtual mass coefficient defined as 0.5 in this study.

2.4. Numerical modelling

To validate the influence of variations in bubble shapes considered in the breakup model, numerical simulations have been carried out for the air-water bubble columns used by Kulkarni et al. [23] and Camarasa et al. [24] denoted by Case 1 and Case 2, respectively, in **Table 1**.

The mesh setup is illustrated in **Figure 4**. Grid 2 consists of $20(r) \times 40(\theta) \times 100(z)$ nodes in the radial, circumferential and axial directions, respectively. The grid independence was tested in a coarser Grid 1 of $16(r) \times 32(\theta) \times 80(z)$ nodes and a refined Grid 3 of $26(r) \times 48(\theta) \times 126(z)$ nodes, in which case the total number of cells is doubled gradually. The grid independence test for these three setups has yielded similar results quantitatively, even though the overall trend of overprediction occurred for all three grids, as shown in **Figure 5**. Grid 2 was chosen and used in subsequent simulations to investigate the effects of the improved breakup model.

	Diameter (m)	Height (m)	Superficial velocity (m/s)	Static liquid height (m)
Case 1	0.15	0.8	0.0382	0.65
Case 2	0.1	2	0.0606	0.9

Table 1. Details of the experimental setup.

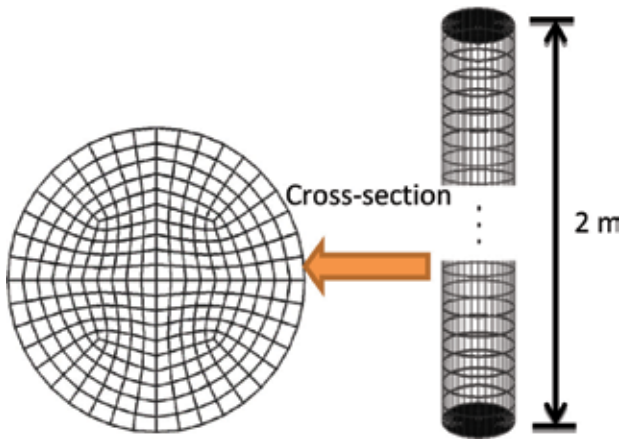

Figure 4. Horizontal cross section and front view of the mesh setup for the main body of the bubble column.

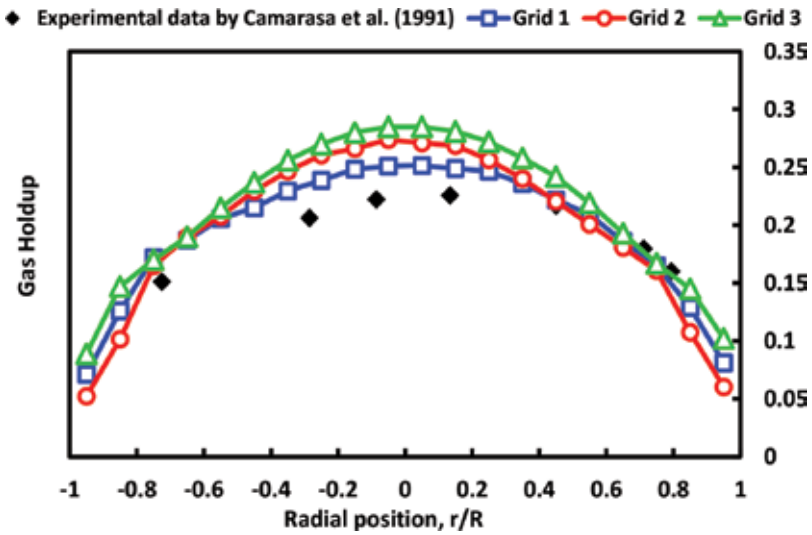

Figure 5. Comparison of the simulated gas holdup profile to the data reported in Camarasa et al. [24] with three different grid configurations.

ANSYS Fluent 3D pressure-based solver is employed in CFD-PBM modelling. The time step is set to be 0.001 s for all simulations, which is considered to be sufficient for illustrating the time-averaged characteristics of the flow fields by carrying out the data-sampling statistics for typically 120 s after the quasi-steady state has been achieved. The improved breakup model is integrated into the simulations by using the user define function (UDF). At the inlet boundary, the volume fraction of gas phase is set to be 1. The treatment of the inlet velocity is different from using a constant superficial gas velocity, but a normally distributed velocity profile is applied by using the model proposed by Shi et al. [25], which can accurately reflect the experimental conditions employed in the study by Camarasa et al. [24]. Further information

about the reasons, theoretical basis and the effects of using the inlet model can be found in their published work. The outlet boundary is set to be a pressure outlet at the top. No-slip conditions are applied for both the liquid and gas phases at the bubble column wall.

3. Results and discussion

3.1. Effect of deformed bubble shape variations on the pressure and surface energy required for bubble breakage

To illustrate the influence of pressure energy control breakup, theoretical predictions of the surface energy and the pressure energy requirements for the breakage of ellipsoidal and spherical-capped bubble are shown, respectively, in **Figure 6**. It can be clearly seen from **Figure 6** that the energy requirement for ellipsoid bubble shifts from pressure energy to surface energy with an increase in the breakup volume fraction. This may be attributed to a higher dynamic pressure being required inside a smaller bubble for resisting the surrounding eddy pressure in order to sustain its own existence. However, the spherical bubble requires most of the surface energy for its breakage. This may mainly be due to the contribution of the large front surface of spherical-capped bubbles.

The surface energy requirement for bubble breakage in **Figure 6** has taken into account the bubble shape variations. To further illustrate the significance of considering the variation of bubble shapes, a theoretical comparison of the increase in surface energy for the breakage of the original spherical bubbles versus various shapes of bubbles has been shown in **Figure 7**.

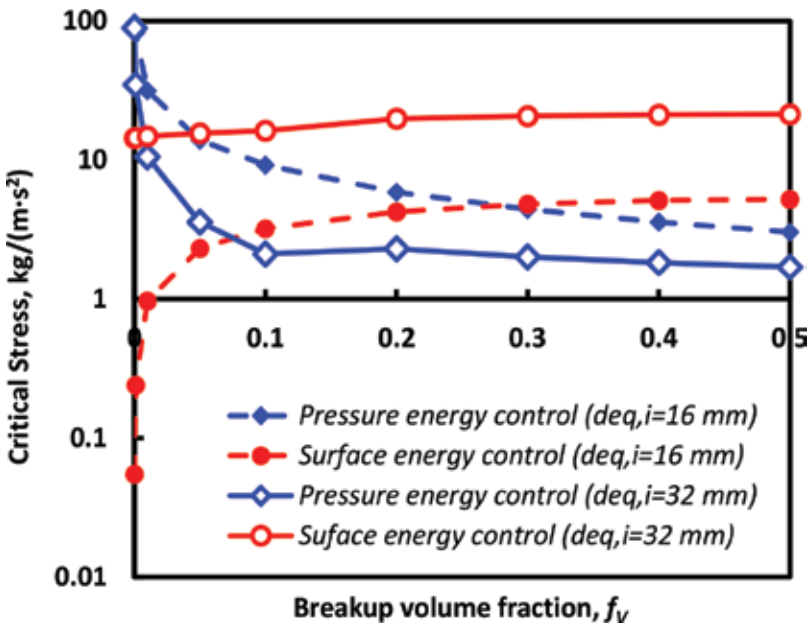

Figure 6. Two competitive control mechanisms of the breakage of ellipsoidal bubbles ($d_{eq,i}$ = 16 mm) and spherical-capped bubbles ($d_{eq,i}$ = 32 mm).

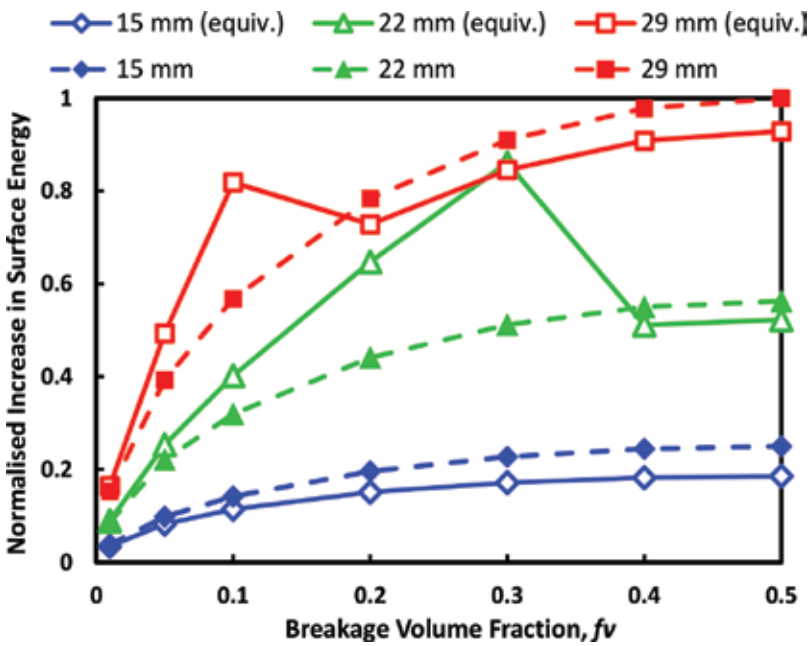

Figure 7. Normalized increase in the surface energy for the breakage of original spherical bubbles and various shapes of bubbles.

The generation of spherical bubbles due to eddy collision with large ellipsoidal or spherical-capped bubble is not covered, as the breakage volume fraction will be far smaller than 0.05. The generation of small spherical bubbles occurs more frequently due to the interaction of the shed eddies with the bubble skirt. This phenomenon was concisely described and explained by numerical modelling work carried out by Fu and Ishii [26]. It is shown in **Figure 7** that the maximum increase in surface energy for ellipsoidal bubbles and spherical-capped bubbles is different. As binary breakage is assumed, a large ellipsoidal bubble breaks into two smaller ellipsoidal bubbles in most cases. The maximum increase in surface energy is demonstrated when equal-size breakage occurs, which suggests that the parent ellipsoidal bubble has been through a large deformation process itself. However, the spherical-capped bubble can break into different combinations of daughter bubble types, including one ellipsoidal and one spherical-capped bubble, two ellipsoidal bubbles, or two spherical-capped bubbles. The maximum increase in surface energy for the breakage of a spherical-capped parent bubble is found with the largest volume fraction of ellipsoidal daughter bubble. This result coincides with the existing experimental observations: the ellipsoidal bubble has a more stable structure that is able to resist bombarding eddies from both the front and the rear, whereas the spherical-capped bubble can only resist eddies hitting from the front but is easily and rapidly ruptured by eddies hitting from the rear.

Figure 8 compares the time-averaged gas holdup predicted by the original breakup model and the improved breakup model. It can be found that the improved breakup model has achieved results very similar to the experimental data at the core region of the column

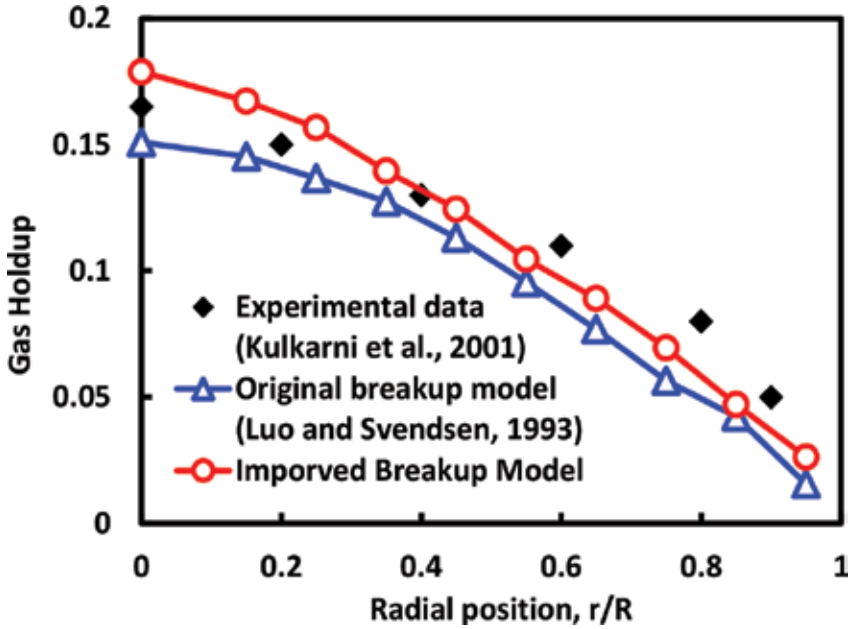

Figure 8. Comparison of the original breakup model and the improved breakup model for the prediction of the gas holdup profile in the radial direction for Case 1.

(r/R < 0.6), while underestimation is shown near the column wall for both the original breakup model and the improved breakup model. Since the standard $k\tilde{}\varepsilon$ turbulence model is still applied in this study, the underestimation of gas holdup may be due to the slight poor prediction of the turbulence dissipation rate. The issue of underestimation on the gas holdup distribution has also been addressed by Chen et al. [27], in which case the breakup rate was artificially increased by a factor of 10 to obtain a "better" agreement with the experimental data.

Figure 9 shows the radial distribution of the time-averaged turbulence dissipation rate for Case 1. The turbulence dissipation rate distribution predicted by the standard $k\tilde{}\varepsilon$ model is smaller than the result obtained by the RNG $k\tilde{}\varepsilon$ model. This is because the RNG $k\tilde{}\varepsilon$ model has a specific contribution from the local strain rate as the correction to the turbulence dissipation rate. The tendency of the standard $k\tilde{}\varepsilon$ model to underestimate the turbulence dissipation rate can also be seen in the studies carried out by Laborde-Boutet et al. [28], Chen [29] and Jakobsen et al. [30]. As a result, the standard $k\tilde{}\varepsilon$ model is insufficient to properly estimate the turbulence dissipation rate in the regions with rapidly strained flows, which most likely corresponds to the near wall region in the bubble columns. It can be seen from Eq. (19) that the breakup rate $\Omega_B\tilde{}\varepsilon^{1/3} \cdot \exp\left(-\varepsilon^{-2/3}\right)$, which is at least equivalent to the dissipation rate ε of the order of −1/3. Therefore, the equilibrium state of bubble coalescence and breakup phenomena cannot be reasonably addressed with an inaccurate estimation of the turbulence dissipation rate and inevitably affect the predictions of gas holdup. Also, as the predicted coalescence rate is about one order of magnitude higher than the predicted breakup rate, the bubble coalescence and

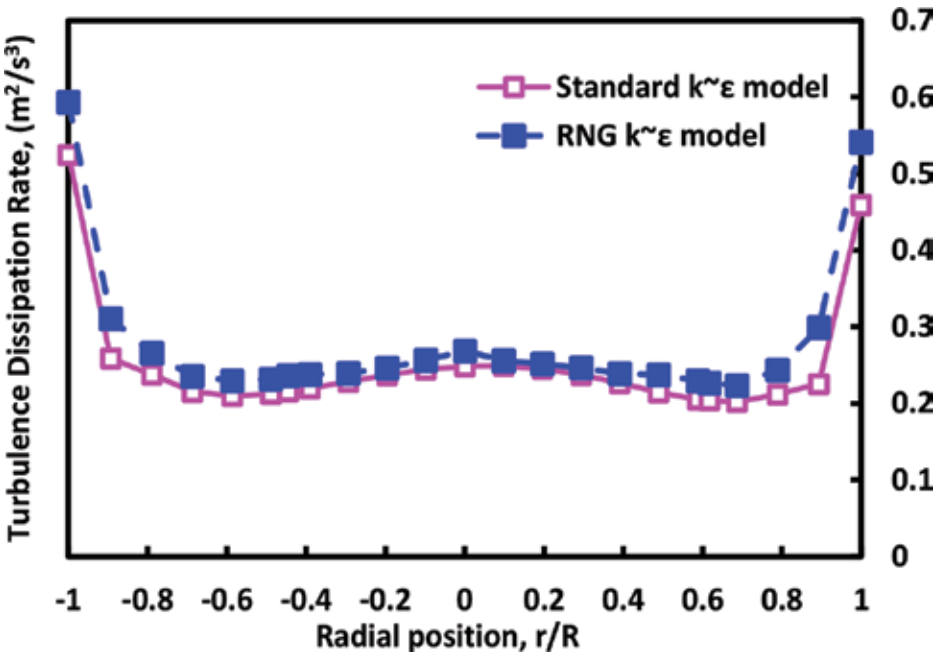

Figure 9. Radial distribution of time-averaged turbulence dissipation rate for Case 1.

breakup phenomena cannot be reasonably addressed under this scenario and will inevitably affect the predictions of gas holdup. In addition, as pointed out by Jakobsen et al. [30], despite the accuracy of calculating the local turbulence dissipation rate from the $k\tilde{}\varepsilon$ turbulence model, this turbulence dissipation rate merely represents a fit of a turbulence length scale to single-phase pipe flow data. Therefore, the contribution of turbulence eddies that are induced by the bubbles has not being included. More importantly, the mechanism of bubble breakage caused by the interactions of bubble-induced turbulence eddies with the subsequent bubbles, which may be dominant in the core region of the bubble column, cannot be revealed through the breakage kernels that are very sensitive to the turbulence dissipation rate.

Figure 10 shows the radial distribution of time-averaged gas holdup at different cross sections in the axial direction. The results are obtained by using the improved breakup model. It can be seen clearly from **Figure 10** that the predicted time-averaged gas holdup in the fully developed region (H/D > 5) has achieved self-preserving characteristics regardless of the axial positions. It appears that the inlet conditions have a weak influence on this self-preserving nature in the bubble columns, which is a result concurring with some previous experimental findings [31, 32].

Figure 11 presents the unit volume-based interfacial area in the bulk region for each bubble class. Due to the large differences in size from the smallest to the largest bubble class, the y-axis is shown in a $\log_{10}$ scale. Interfacial area is a key parameter that largely affects the prediction of heat and mass transfer between gas and liquid phase in the bubble columns. Although the differences in the simulated interfacial area between the improved breakup model and the original breakup

http://dx.doi.org/10.5772/intechopen.76448

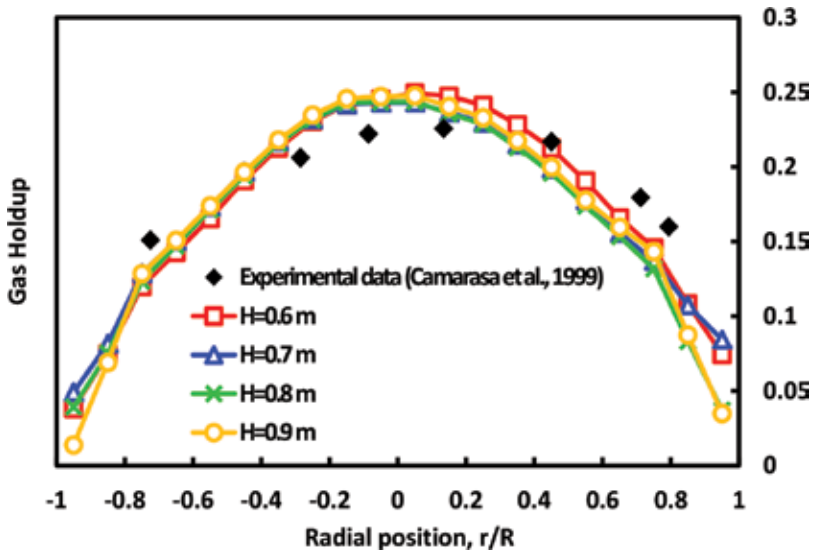

Figure 10. Radial distribution of time-averaged gas holdup at different axial positions.

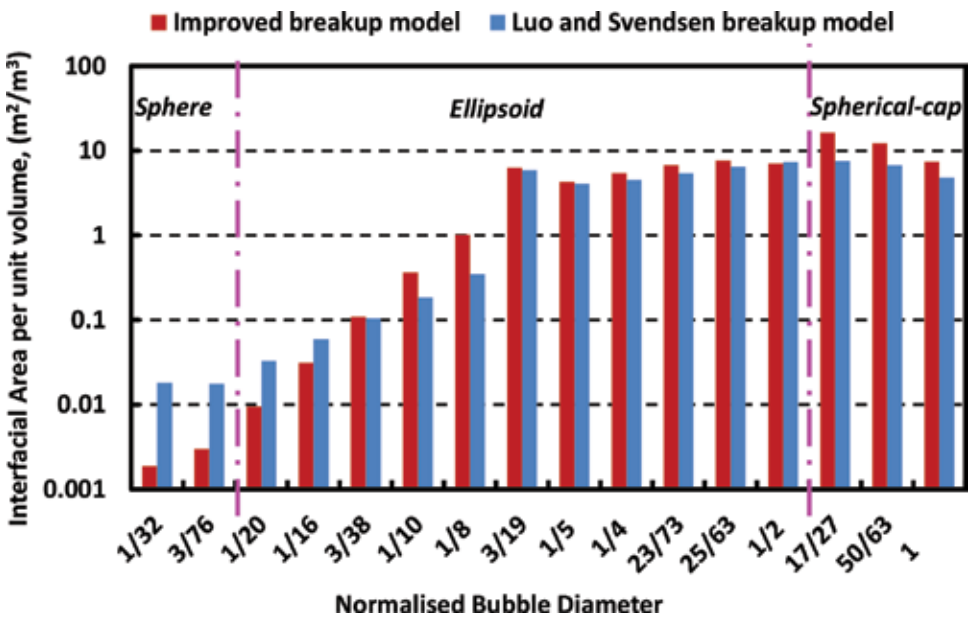

Figure 11. Comparison of the simulated interfacial area in the bubble column for Case 2.

model are not significant when the bubble size is relatively small, the influence of the bubble shapes is gradually reflected when the shape of the bubbles transforms from ellipsoid to spherical-cap, resulting in much larger interfacial areas for spherical-capped bubbles.

3.2. Effect of deformed bubble shape variations on the interfacial mass transfer across bubble surfaces

The interfacial area obtained by the improved breakup model is based on the statistical model of bubble shapes. The results will be slightly different when a more realistic model, which considers the dynamic deformations that occur during bubble motions, is implanted into the simulations. Indeed, the current results have implied that assuming all bubbles to be of a spherical shape may lead to significant underestimation of the interfacial area and hence affect the predictions of the heat and mass transfer rate when chemical reactions are considered in the bubble column reactors. To further address this issue, the volumetric mass transfer coefficient, k_La, estimated based on the improved breakup model for each bubble class is presented in **Figure 12**.

The convective mass transfer film coefficient can be defined by Eq. (37)

$$k_L = \frac{\overline{D}}{d} Sh \tag{37}$$

where $\overline{D}$ is mass diffusivity, d is the bubble diameter and Sh is the Sherwood number. The Sherwood number represents the ratio of the convective mass transfer to the rate of diffusive mass transfer. It can be determined by using the Frossling equation described by Eq. (38)

$$Sh = 2 + 0.552 \mathrm{Re}^{\frac{1}{2}} Sc^{\frac{1}{3}} \tag{38}$$

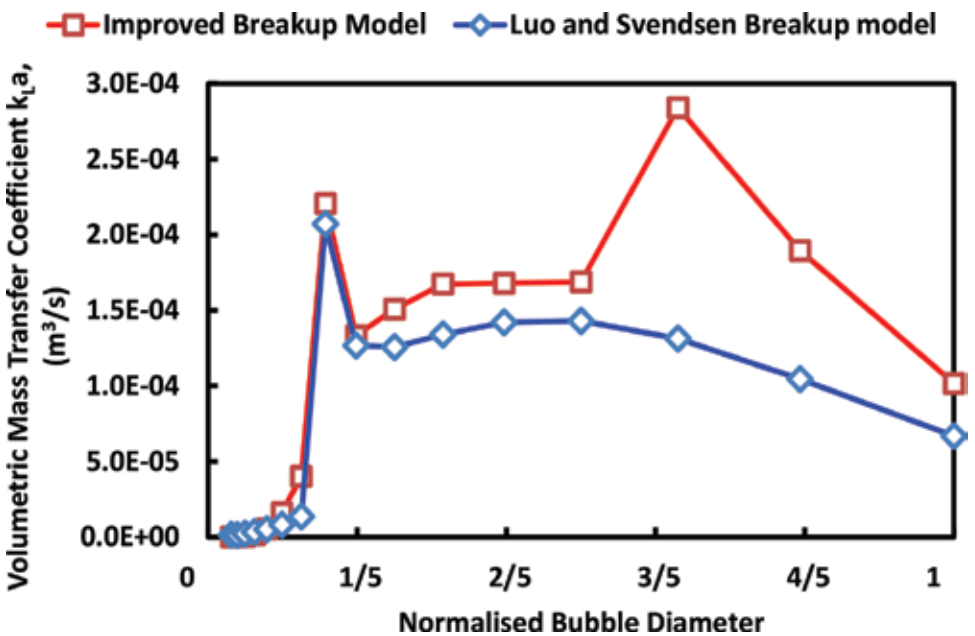

Figure 12. Comparison of the volumetric mass transfer coefficient for each bubble class.

Re in Eq. (38) is the bubble Reynolds number and *Sc* is the Schmidt number. The Schmidt number is the ratio of momentum diffusivity to mass diffusivity, defined by Eq. (39)

$$Sc = \frac{\upsilon}{\overline{\overline{D}}} \tag{39}$$

According to the analogy between heat and mass transport phenomena, a similar method can be applied to calculate the Nusselt number by simply replacing the Schmidt number with the Prandtl number. By doing so, the ratio of convective heat transfer to conductive heat transfer can be characterized.

It is observed that the volumetric mass transfer coefficient is greatly increased due to the contribution of ellipsoidal and spherical-capped bubbles. However, the peak value obtained based on the improved breakup model may be attributed to the predicted number density of the corresponding bubble class. As illustrated in **Figure 7**, the improved breakup model requires a higher increase in surface energy at the boundary of ellipsoidal and spherical-capped bubbles, which makes the smallest spherical-capped bubbles more difficult to break. The results for this particular bubble class may not be a good reflection of the physical phenomenon in reality, but the overall enhancement of the mass transfer coefficient is still very significant. The predictions on the overall mass transfer coefficient are shown in **Figure 13**. **Figure 14** presents the local mass transfer coefficient at different cross sections along the height of the bubble column. It can be seen from **Figure 14** that the mass transfer rate estimations based on Luo and Svendsen model and the improved breakup model are obviously very different. The results based on the Luo and Svendsen model may imply that the mass transfer is mainly associated with the regions where the larger Sauter mean bubble diameter has been predicted. The results based on the improved breakup model suggest that the mass transfer is

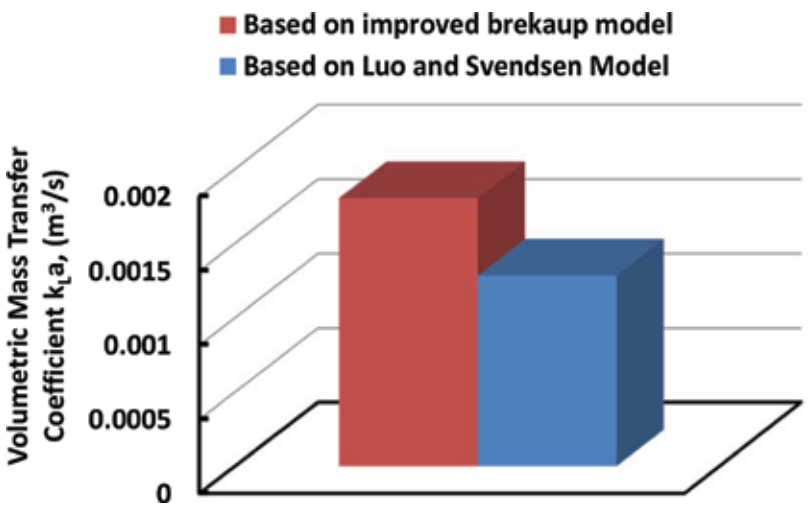

Figure 13. Volumetric mass transfer coefficient predicted using both the improved breakup model and Luo and Svendsen model [3].

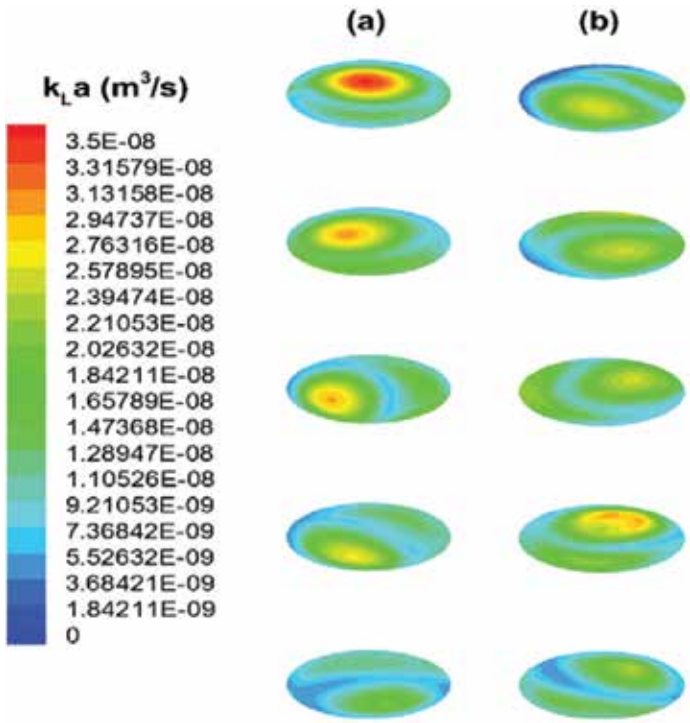

Figure 14. Distribution of estimated volumetric mass transfer coefficient at different cross sections in the bubble column for Case 2. (a) Luo and Svendsen model; (b) improved breakup model. (from top to bottom: H = 0.6, 0.5, 0.4, 0.3 and 0.2 m.).

more uniformly distributed, in which case the enhanced overall mass transfer estimation comes from the statistical sum of the contributions of each bubble class.

4. Conclusion

In this study, an improved breakup model has been proposed based on the breakup model by Luo and Svendsen [3]. This improved breakup model takes into account the variation of bubble shapes in bubble columns, which include spherical, ellipsoid and spherical-cap shaped bubbles. In addition, the model considers the pressure energy controlled breakup coupled with modified breakage criteria. The simulation results demonstrate an overall agreement with the experimental data reported in the open literature. The difference between the surface energy and the pressure energy requirements for forming various daughter bubbles has been illustrated. The energy density constraint has been applied to prevent overestimating the breakage rate of small bubbles. This study on the dynamic behaviour of various bubble shapes could potentially lead to a more comprehensive understanding of the mass and heat transfer characteristics of multiphase flows in the bubble column.

Acknowledgements

This work was supported by the National Natural Science Foundation of China (Grant no. 91534118). Weibin Shi would also like to acknowledge the Ph.D. scholarship of the International Doctoral Innovation Centre (IDIC) of University of Nottingham Ningbo China and the support of EPSRC (Grant no. EP/G037345/1).

This chapter is an extension of a conference paper that was presented at the 13th International Conference on Heat Transfer, Fluid Mechanics and Thermodynamics (HEFAT2017) and was nominated for invitation into the HEFAT2017 Special Issue of Heat Transfer Engineering based on its designation as a high-quality paper of relevance to the modelling of fluids based systems.

Nomenclature

a	long half axis length of a ellipse, m
c	short half axis length of a ellipse, m
C_D	effective drag coefficient for a bubble around a swarm, dimensionless
D	bubble column diameter, m
$\overline{D}$	mass diffusivity, m^2/s
d	bubble diameter, m
d_{eq}	equivalent bubble diameter, m
d_V	length of virtual axis, m
Eo	Eötvös number, dimensionless
$\bar{e}$	mean turbulence kinetic energy, $kg{\cdot}m^2/s^2$
e_s	increase in surface energy, $kg{\cdot}m^2/s^2$
F_D	drag force, N/m^3
F_{Lift}	lift force, N/m^3
F_{VM}	virtual mass force, N/m^3
f_V	breakage volume fraction, dimensionless
g	gravity acceleration, m/s^2
H	distance from the bottom surface, m
k	turbulence kinetic energy, m^2/s^2
k_L	convective mass transfer film coefficient, m/s

Mo	Morton number, dimensionless
n	number density per unit volume, m^{-3}
t	time, s
Rc	radius of curvature, m
Re	Reynolds number, dimensionless
S	surface area, m^2
Sh	Sherwood number, dimensionless
Sc	Schmidt number, dimensionless
U	superficial velocity, m/s
U_t	terminal velocity, m/s
$\bar{u}_\lambda$	mean velocity of turbulence eddies, m/s
u	velocity vector, m/s
V	volume, m^3

Greek letters

α	phase volume fraction, gas holdup
ε	turbulence dissipation rate, m^2/s^3
λ	characteristic length scale of eddy, m
μ	molecular dynamic viscosity, Pa·s
μ_{eff}	effective turbulence dynamic viscosity, Pa·s
υ	kinematic viscosity, m^2/s
ρ	fluid density, kg/m^3
σ	surface tension, N/m
τ	shear stress, Pa

Subscripts

b	bubble
g	gas
i	i-th class bubble
j/k	daughter bubble
l	liquid

Author details

Weibin Shi[1], Jie Yang[2], Guang Li[1], Yuan Zong[3] and Xiaogang Yang[1]*

*Address all correspondence to: xiaogang.yang@nottingham.edu.cn

1 Department of Mechanical, Materials and Manufacturing Engineering, The University of Nottingham Ningbo China, Ningbo, PR China

2 School of Mathematical Sciences, The University of Nottingham Ningbo China, Ningbo, PR China

3 State Key Laboratory of Chemical Engineering, East China University of Science and Technology, Shanghai, PR China

References

[1] Coulaloglou CA, Tavlarides LL. Description of interaction processes in agitated liquid-liquid dispersions. Chemical Engineering Science. 1977;**32**(11):1289-1297

[2] Prince MJ, Blanch HW. Bubble coalescence and break-up in air-Sparged bubble-columns. AICHE Journal. 1990;**36**(10):1485-1499

[3] Luo H, Svendsen HF. Theoretical model for drop and bubble breakup in turbulent dispersions. AICHE Journal. 1996;**42**(5):1225-1233

[4] Lehr F, Millies M, Mewes D. Bubble-size distributions and flow fields in bubble columns. AICHE Journal. 2002;**48**(11):2426-2443

[5] Wang TF, Wang JF, Jin Y. A novel theoretical breakup kernel function for bubbles/droplets in a turbulent flow. Chemical Engineering Science. 2003;**58**(20):4629-4637

[6] Zhao H, Ge W. A theoretical bubble breakup model for slurry beds or three-phase fluidized beds under high pressure. Chemical Engineering Science. 2007;**62**(1–2):109-115

[7] Andersson R, Andersson B. Modeling the breakup of fluid particles in turbulent flows. AICHE Journal. 2006;**52**(6):2031-2038

[8] Liao YX, Rzehak R, Lucas D, Krepper E. Baseline closure model for dispersed bubbly flow: Bubble coalescence and breakup. Chemical Engineering Science. 2015;**122**:336-349

[9] Han LC, Luo HA, Liu YJ. A theoretical model for droplet breakup in turbulent dispersions. Chemical Engineering Science. 2011;**66**(4):766-776

[10] Luo H. Coalescence, Breakup and Liuqid Circulation in Bubble Column Reactors. PhD thesis from the Norwegian Institute of Technology: Trondheim, Norway; 1993

[11] Grace JR, Clift R, Weber ME. Bubbles, Drops, and Particles. Academic Press; 1978

[12] Tomiyama A. Struggle with computational bubble dynamics. Multiphase Science and Technology. 1998;**10, 1998**(4):369-405

[13] Cano-Lozano JC, Bohorquez P, Martinez-Bazan C. Wake instability of a fixed axisymmetric bubble of realistic shape. International Journal of Multiphase Flow. 2013;**51**:11-21

[14] Zhou W, Dusek J. Marginal stability curve of a deformable bubble. International Journal of Multiphase Flow. 2017;**89**:218-227

[15] Tripathi MK, Sahu KC, Govindarajan R. Dynamics of an initially spherical bubble rising in quiescent liquid. Nature Communications. 2015;**6**

[16] Tomiyama A, Miyoshi K, Tamai H, Zun I, Sakafuchi T. A bubble tracking method for the prediction of spatial-evolution of bubble flow in a vertical pipe. In: 3rd International Conference on Multiphase Flow (ICMF 98); 1998: Lyon, France

[17] Wellek RM, Agrawal AK, Skelland AH. Shape of Liquid Drops Moving in Liquid Media. Aiche Journal. 1966;**12**(5):854

[18] Davenport WG, Bradshaw AV, Richardson FD. Behaviour of spherical cap bubbles in liquid metals. Journal of the Iron and Steel Institute. 1967;**205**:1034

[19] Landel JR, Cossu C, Caulfield CP. Spherical cap bubbles with a toroidal bubbly wake. Physics of Fluids. 2008;**20**(12):122101

[20] Guo XF, Zhou Q, Li J, Chen CX. Implementation of an improved bubble breakup model for TFM-PBM simulations of gas-liquid flows in bubble columns. Chemical Engineering Science. 2016;**152**:255-266

[21] Han LC, Gong SG, Li YQ, Gao NN, Fu J, Luo H, Liu ZH. Influence of energy spectrum distribution on drop breakage in turbulent flows. Chemical Engineering Science. 2014;**117**: 55-70

[22] Sato Y, Sekoguchi K. Liquid velocity distribution in two-phase bubble flow. International Journal of Multiphase Flow. 1975;**2**(1):79-95

[23] Kulkarni AA, Joshi JB, Kumar VR, Kulkarni BD. Application of multiresolution analysis for simultaneous measurement of gas and liquid velocities and fractional gas hold-up in bubble column using LDA. Chemical Engineering Science. 2001;**56**(17):5037-5048

[24] Camarasa E, Vial C, Poncin S, Wild G, Midoux N, Bouillard J. Influence of coalescence behaviour of the liquid and of gas sparging on hydrodynamics and bubble characteristics in a bubble column. Chemical Engineering and Processing. 1999;**38**(4–6):329-344

[25] Shi W, Yang N, Yang X. A kinetic inlet model for CFD simulation of large-scale bubble columns. Chemical Engineering Science. 2017;**158**:108-116

[26] Fu XY, Ishii M. Two-group interfacial area transport in vertical air-water flow I. Mechanistic model. Nuclear Engineering and Design. 2003;**219**(2):143-168

[27] Chen P, Dudukovic MP, Sanyal J. Three-dimensional simulation of bubble column flows with bubble coalescence and breakup. AICHE Journal. 2005;**51**(3):696-712

[28] Laborde-Boutet C, Larachi F, Dromard N, Delsart O, Schweich D. CFD simulation of bubble column flows: Investigations on turbulence models in RANS approach. Chemical Engineering Science. 2009;**64**(21):4399-4413

[29] Chen P. Modeling the fluid dynamics of bubble column flows. Ph.D. Thesis, in Sever Institute of Washington University: StLouis, USA; 2004

[30] Jakobsen HA, Lindborg H, Dorao CA. Modeling of bubble column reactors: Progress and limitations. Industrial & Engineering Chemistry Research. 2005;**44**(14):5107-5151

[31] Kumar SB, Moslemian D, Dudukovic MP. Gas-holdup measurements in bubble columns using computed tomography. AICHE Journal. 1997;**43**(6):1414-1425

[32] Thorat BN, Shevade AV, Bhilegaonkar KN, Aglawe RH, Veera UP, Thakre SS, Pandit AB, Sawant SB, Joshi JB. Effect of sparger design and height to diameter ratio on fractional gas hold-up in bubble columns. Chemical Engineering Research and Design. 1998;**76**(A7):823-834

Chapter 5

Discussions of Effects of Surface Tension on Water Vapor Absorbed by Triethylene Glycol Solution Films

Honda Wu (Hung-Ta Wu) and Tsair-Wang Chung

Additional information is available at the end of the chapter

http://dx.doi.org/10.5772/intechopen.76148

Abstract

The surface tension gradient can result from releasing a surfactant from the liquid film or feeding a vapor into the liquid film, and the interfacial disturbance will be induced by them. The flowing phenomena were termed "Marangoni effect," and the mass transfer performance was enhanced by the effect. The objective of this study was to apply the Marangoni effect, such as water vapors absorbed by the liquid film of triethylene glycol (TEG) solution, and to analysze mass transfer behaviors with and without surfactants' addition in the liquid film. The interfacial disturbance resulted from the surface tension gradient was considered in this study, and the mass transfer behaviors for packed-bed absorbers were discussed to elucidate the influence of the Marangoni effect on the absorbers. It was observed that the trends of mass transfer rates could be increased significantly as the surfactant is added into the absorption system. Experimental results showed that feeding a vapor or adding a surfactant with lower surface tension and/or higher volatility in the liquid will result in the surface tension gradient on the gas-liquid interface. The induced flowing disturbance will lead to an increment of mass transfer rate for a gas-liquid contact system.

Keywords: solution film, TEG solution, absorption, Marangoni, surface tension

1. Introduction

The fluid disturbance resulting from the surface tension gradient in the interface of the gas-liquid contact systems is usually called the Marangoni effect or surface tension effect. For the liquid thin film, the gas solutes are easier to dissolve into the thinner liquid film than the thicker liquid film [1], and the concentration in the thinner part would be higher than that

in the thicker part. Therefore, the surface tension gradient is formed in the interface. The Marangoni positive and negative systems can be defined by changes of the gas-liquid contacting area. The interfacial convection resulting from the Marangoni effect is usually called the Marangoni convection. The interfacial instability resulting from the surface tension is normal to the liquid surface, and it is always called the Marangoni instability. The surface tensions for absorption solutions could be measured by a surface tension meter (CBVP-A3, Kyowa Interface Co. Ltd.). The surface tension meter was based on the method for a Wilhelmy plate, as shown in **Figure 1**. A Wilhelmy plate is a thin plate, usually in the order of a few square centimeters in area, used to measure equilibrium surface or interfacial tension at a gas-liquid or liquid-liquid interface. The top of the plate was connected to a spring, and the spring was connected to a force sensor. The equilibrium state is reached instantaneously between the surface tension acting on the plate and the spring force pulling up the plate as the plate comes in contact with the liquid surface. According to the Wilhelmy equation, shown in Eq. (1), embedded in the surface tension meter, the surface tension for a liquid solution would be calculated and displayed on the panel.

$$\gamma = \frac{F}{l\cos\theta} \tag{1}$$

where γ is surface tension, F is elastic force, l is the wetted perimeter, and θ is the contact angle between the liquid phase and the plate.

Mentioned earlier, the flow of interfacial fluid could be provoked by the Marangoni effect. The methods for inducing surface tension gradient include the design of electric field with

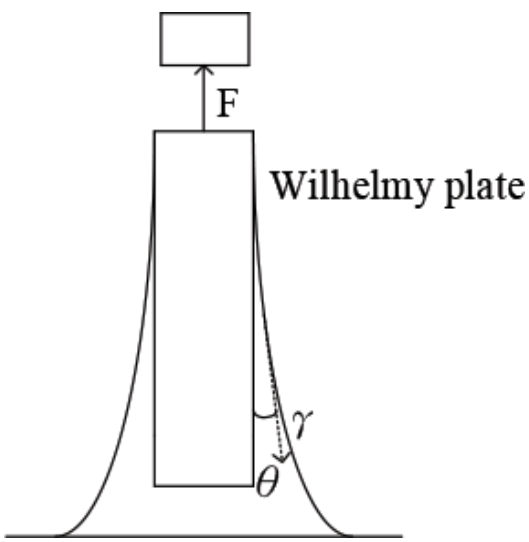

Figure 1. Schematic diagram for surface tension of the liquid solution exerted the plate.

ionic compounds, concentration difference, temperature difference and surfactant addition to the liquid solution. Therefore, the interfacial disturbance could be produced by solutes transferring across phases. Some studies described the relationship between the Marangoni effect and transport phenomena, which are introduced as follows.

The working electrodes were set in the experimental cell to detect the potential energy [2]. The concentration of the ferrocenyl surfactant was decreased with the decreased potential energy and then the surfactant became the surface active matter. The experimental results showed that the velocity of Marangoni flow decreased with the decreased desorption rate of the ferrocenyl surfactant. The concentration gradient of the desorbed ion resulted from the potential energy, and the surface tension gradient was formed by the concentration gradient. Therefore, the fluid disturbance was provoked in the surface layer of the liquid solution. In addition, the concept of the solutal Marangoni effect was always used to describe the fluid flow in the liquid surface by vaporizing the volatile materials. For example, see Ref. [3]. The mixture of ethanol/water, heptane/decane, hexane/decane, and octane/decane was used to show that the liquid film climbs from a macroscopic reservoir as the volatile component with lower surface tension in the system. On the other hand, the studies about the thermal Marangoni effect focused on the convective phenomena for the bulk liquid layer with heating in the bottom. Since the heat source was from the bottom, the liquid density decreased along with the depth of the liquid solution. Therefore, the upward convection occurred due to the temperature gradient. Furthermore, the temperature of the upward fluid was still higher than the ambient liquid in the surface, and then the surface tension gradient was formed to make the outward flow radial. The local outward flow could be observed all over the liquid surface, and it was the so-called cellular-type flow. The small disturbance analysis was adopted to deduce that the surface tension gradient resulted from the change of temperature, which was large enough to produce the cellular-type flow in the liquid convective cell that was heated from the bottom [4].

In order to enhance the mass transfer performance for water vapor absorption by the solution in the absorption-refrigeration system, some surface additives were added to the liquid surface to activate the interfacial disturbance. N-hexanol, n-heptanol, n-octanol, 2-ethyl-hexanol, or n-nonanol was used as a surfactant to enhance the performance for water vapor absorption by the aqueous LiCl solution [5]. The experimental results showed that the interfacial disturbance occurred and the absorption capacity was enhanced in the concentration of n-octanol from 10 to 25 ppm. For the aqueous LiBr solution, adding the surfactants, except n-hexanol, induced the interfacial disturbance. The concentrations of other surfactants were controlled at 25 ppm. Besides, the absorption capacities for CO_2 absorbed by water were increased as methanol, ethanol, n-propanol, n-butanol, and n-propanol added onto the liquid surface [6]. However, the interfacial disturbance could not be observed as n-hexanol and Triton X-100 were added on the surface of water. Based on the thickness of the liquid layer, the Marangoni number was also calculated to assess the critical point for the interfacial disturbance resulting from the spreading liquid.

In addition to adding surfactants on the liquid phase, there are also some studies adding surface additives to the gas phase to discuss the effect of surface active materials on mass transfer

performance and the relationship between mass transfer performance and interfacial disturbance. By measuring the surface tension of liquid solution, the surface tension of liquid solution affected by the vapor of 2-ethyl-1-hexanol (2EH) in the gas phase was demonstrated [7]. The experimental results showed that the effect of surface additives on surface tension was larger for adding in the gas phase than in the liquid phase. Subsequently, the dynamic theory for the absorption and desorption of 2EH on the surface of the LiBr aqueous solution was discussed [8]. The simulated results showed that the higher the vapor pressure of 2EH in the gas phase, the better the mass transfer performance for absorbing H_2O by the LiBr aqueous solution. Therefore, the mass transfer performance could be enhanced by the interfacial disturbance resulting from adding surface additives in the liquid and gas phases while the operating variables were controlled well. Discussions of the interfacial behaviors resulted from adding surfactants to the gas phase, which were limited in the literature, and the related data were rare. Mentioned earlier, the surface tension was affected by adding surfactant to the liquid and gas phases, leading to the influenced mass transfer performance by the interfacial disturbance resulting from the surface tension gradient. Therefore, the surfactant was added in the gas and liquid phases to discuss the effect of surfactant on mass transfer performance. Besides, the mass transfer performance with and without surfactant addition to the working solution in the packed-bed absorber was also compared. Not only was the relationship between mass transfer process and interfacial phenomena described but also the enhancement of mass transfer performance for the absorption system was demonstrated in this study.

2. Solution film in the mass transfer equipment

Table 1 shows some literature related to mass transfer equipment with continuous liquid phase. These mass transfer equipment include packed-bed absorber, packed-bed or tray distillation column, falling film absorber, concentric absorption system, and bubble absorber. Except for bubble absorber [9, 10], a continuous liquid phase was presented as a solution film in the mass transfer equipment for all others. As mentioned by Wu [11], the Marangoni effect could be triggered in mass transfer systems with continuous liquid phases. Therefore, mass transfer behaviors that occurred in the solution film are discussed in this article.

In order to discuss the spontaneous Marangoni effect in the absorption process, an absorber packed closely with cylindrical packing was designed [11]. The solution flow rate was controlled under the state of laminar flow. Since the surface tension of water vapor is larger than that of TEG solution, the spontaneous Marangoni effect is triggered by absorbing water vapor in the solution film. Although the mass transfer performance could be enhanced by adding a promoter in capturing CO_2 by potassium carbonate (KCO_3), the pressure drop and holdup increased in the packed absorption column. For example, see Ref. [12]. Glycine was added to K_2CO_3 solution film to examine the enhancement of the CO_2 absorption. In addition to adding surface additives, the Marangoni instability could also be produced by the temperature dependence of the surface tension, such as nonlinear model of the instability in gas absorption was developed [13] to discuss the performance for carbon dioxide absorbed by water. Recently, the structured packings with different thickness and channel angles were designed [14] to study effect of packings and surface additives on the performance of water vapor absorbed by LiCl film.

Mass transfer equipment	Mass transfer material	Behaviors for solution film	References
Bubble absorber	NH_3/water	Surface tension of solution is suddenly dropped when the surfactant is added	[9]
	CO_2/water	Surface tension gradient was resulted in the presence of surface active substances	[10]
Packed-bed absorber	H_2O/TEG	The area for the surface of packing material covered by TEG solution was greater for the higher concentration	[11]
	CO_2/K_2CO_3	Reduction in the surface tension of the solvent by adding glycine	[12]
	CO_2/water	Marangoni instability caused by the temperature dependence of the surface tension	[13]
	Water/LiCl	Effective interfacial area affected by channel angle	[14]
Distillation column	n-Heptane/methylcyclohexane	The smaller packing and the lower liquid flow rates promote the surface refreshment	[15]
	Methanol/water, methanol/isopropanol and water/acetic acid	The effective interfacial area is the same for the positive and neutral Marangoni systems at low vapor rates	[16]
	Methanol-water, methanol-2-propanol and n-heptane-toluene	Froth stabilization in positives systems resulted in the increased interfacial area	[17]
	Methanol/isopropanol and methanol/water	The positive Marangoni effect causes stable film on the packing	[18]
Falling film absorber	H_2O/LiBr	Surface tension of LiBr was decreased by adding 2-ethyl-1-hexanol (2EH)	[19]
	H_2O/LiBr	Uneven distribution of surface tension at interface was induced by 2EH	[20]
	CO_2/MEA	Cellular convection was provoked by minute changes in surface tension	[21]
	CO_2/MEA solution CO_2/NaOH solution	Cellular convection was observed by adsorption of CO_2 in MEA solution	[22]
Concentric absorption system	CO_2/water	The Marangoni convection was induced by additive and hindered by surfactant	[23]
	H_2O/LiCl	The interfacial disturbance was induced by adding ethanol	[24]

Table 1. Some literature related to mass transfer equipment with continuous liquid phase.

Based on the concept of Marangoni effect acting on the thin liquid film, the system n-heptane/methylcyclohexane was used [15] to discuss the effect of positive and negative driving force on different packings. The criteria for determining the positive or negative driving force for the packed-bed distillation column were based on the packings; however, the criteria for determining the positive or negative Marangoni effect was decided by the mixture. The systems included methanol/water, methanol/isopropanol, and water/acetic acid, which were used to discuss the effective interfacial area for the positive, negative, and neutral Marangoni systems [16]; the systems included methanol-water, methanol-2-propanol, and n-heptane-toluene [17] to elucidate the relationship between froth stabilization and interfacial area; the systems included methanol/isopropanol and methanol/water [18] to describe the solution film affected by the Marangoni effect.

In addition to the packed-bed absorber, the falling film or wetted wall column was also applied for the absorption process widely. 2EH was used as an additive in the vertical falling film to discuss heat and mass transfer enhanced by the Marangoni convection [19, 20]. Furthermore, the flat copper plate and the copper plate covered with a copper wire screen were also tested to observe the Marangoni convection resulting from adding 2EH to the solution film [20]. In contrast with water vapor absorbed by aqueous lithium bromide solution, carbon dioxide absorbed by aqueous monoethanolamine (MEA) solution could be regarded as a chemical absorption process. Since the surface tension of the absorbent solution was changed by a chemical absorption process, the Marangoni effect was always accompanied with this process. For example, see Refs. [21, 22]. CO_2 absorbed by the MEA solution was conducted, and the mass transfer enhancement and the cellular convection were discussed and observed.

Whatever gradient in surface tension resulted from spontaneous or artificial absorption process, it is difficult to observe by naked eye or scientific apparatus. Since the induced Marangoni convection and Marangoni instability were microscopic phenomena, they could be recorded or observed by scientific or special apparatus. On the basis of the difficult observation, some experimental systems were designed to demonstrate the mass transfer performance enhanced by the Marangoni effect, such as the concentric absorption system. Generally speaking, the surface additive with lower surface tension was injected by a capillary tube into the center of the absorption cell. For example, see Ref. [23]. Methanol, ethanol, propanol, and acetone were used as surface additives, respectively, to discuss absorption of CO_2 by water and surfactant solution in the presence and absence of Marangoni effect. Not only the liquid additive in the liquid surface but also vapor additive in the absorption system were carried out to analyze enhancement of mass transfer performance by the Marangoni effect for water vapor absorbed by LiCl solution [24].

The concept of packed-bed absorber was also the solution film that flowed over packing materials so that a series of experiments were performed to discuss absorption of water vapor by TEG solution and to elucidate the relationship between interfacial disturbance and mass transfer behaviors. TEG solution was used as a working solution to absorb water vapor in the packed-bed absorber, as shown in **Figure 2**, and the packing materials were 5/8-inch polypropylene flexi rings. The system can handle air flow rates from 1.35 to 1.58 kg/m^2 s and liquid flow rates from 0.6 to 0.9 kg/m^2 s. The flow meters and flow controller used in this study

http://dx.doi.org/10.5772/intechopen.76148

were calibrated by standard procedures. The absorbent solution was brought into the packed bed by the liquid pump and distributed over the packed bed by the nozzle. The liquid flow rates were controlled by rotameter. The air flow rates were adjusted by 0.5 HP blower and transistor inverters. The liquid film, flowed on the packing, contacted the gas phase in the packed-bed absorber and absorbed water vapor successfully. After a series of experimental tests (3–4 runs) were completed, the absorption system was heated to raise the temperature of the TEG solution. Once the heated solution contacted with the process air, the water molecules in the absorbent solution were stripped from the TEG solution. The regenerated TEG solution could be reused in the next series of experimental tests. Besides, a Rotronic IDL 20 K hygrometer with two humidity probes, which can measure the humidity from 0 to 100% RH

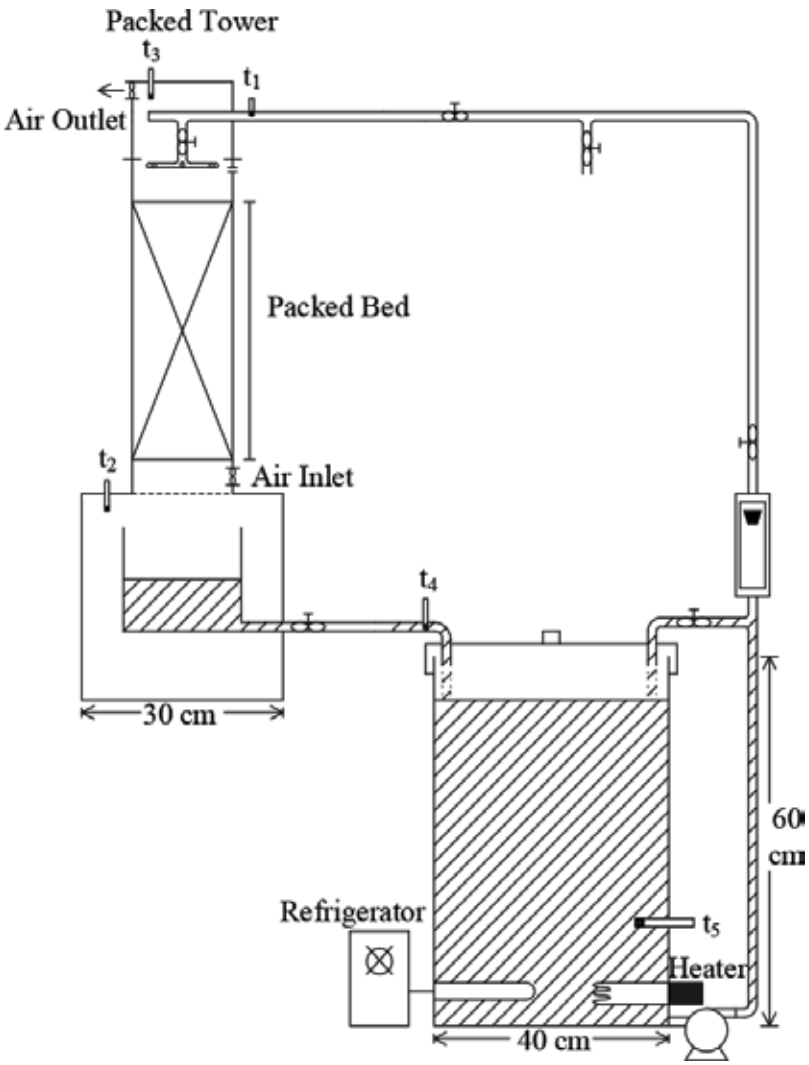

Figure 2. Experimental apparatus of this study.

at −20 to 60°C, was used in this study. The concentration of the TEG solution was measured by a refractometer. The cross-section area of the packed bed and air tunnel was 15*15 cm^2, and the height of packing was 45 cm. The absorption capacity could be calculated by the inlet and outlet humidity to discuss effect of operating variables on mass transfer performance.

The water vapors were absorbed by 93 wt.% TEG solution and 93 wt.% TEG solution with 5 wt.% ethanol, respectively. Therefore, effect of operating variables on mass transfer performance was discussed, and absorption capacities with and without surface additives added to the TEG solution were compared. On the other hand, the ethanol vapor was injected in the gas phase to discuss mass transfer difference between the additive adding in the liquid and gas phases.

3. Discussions for mass transfer

3.1. Mass transfer results for solution film in the equipment

A series of experiments presented in this article were water vapor absorbed by the TEG solution films in the packed-bed absorber. Therefore, some results related to solution film in the mass transfer equipment were described as follows.

For packed-bed absorber, the effective interfacial area is increased for the positive Marangoni effect. Absorption of water by LiCl solution [14] found that the surface area was larger for a 30° channel angle and 6 mm thickness packing material. Therefore, the maximum heat and mass transfer performance were 0.4 for COP and 85% for dehumidification efficiency. Since the foam resulted from addition of surface additive would hinder mass transfer process, addition of surface additive into the LiCl solution did not helpful. For absorption of water vapor by TEG solution [11], results showed that the mass transfer performance was larger for concentration of TEG solution greater than 92 wt.%. Since the surface tension of water vapor was higher than that of TEG solution, the surface tension of TEG solution is increased during the absorption process. The coverage of the higher concentration of TEG solution on the packing surface was wider than the lower concentration due to the difference in surface tension. The coverage of TEG solution on the packing surface resulted from increment in surface tension, which could be termed as a positive Marangoni effect for the absorption system.

For the gradient in surface tension, the Marangoni effect in the packed-bed distillation column was divided into a positive and a negative system. Transportation of a component with lower surface tension from a liquid phase to a gas phase may increase surface tension in the surface of the transferred spot. Since the surface tension for the transferred spot is higher than the surrounding liquid, the surrounding liquid is drawn to the transferred spot. The flow phenomenon driven by this process may spread over the packing well in the packed-bed distillation column and increase mass transfer performance. Therefore, the system, making a more effective area on the packing, is termed "positive system." On the contrary, transportation of a component with high surface tension from a liquid phase to a gas phase may decrease surface tension in the surface of the transferred spot. Since the surface tension for the transferred spot is lower than the surrounding liquid, the induced stress is directed from the transferred spot to the surrounding liquid. The flow phenomenon may lead the packing surface to be contrasted.

Since the mass transfer performance would decrease with the decreased effective area, such a system is termed "negative system." Therefore, the surface refreshment was affected by the smaller packing and the lower liquid flow rates more significantly [15]. Three systems include organic and aqueous systems, Marangoni positive (methanol/water), neutral (methanol/isopropanol), and negative (water/acetic acid) systems, which were used to develop a mass transfer model for a distillation column packed with the structured packing [16]. The results showed that the effective area was larger for the positive system than that of the negative system due to the more stable liquid film. Besides, the experimental results also demonstrated that the better liquid distribution or more stable liquid film on the packing surfaces resulted from the positive effect, methanol/water, to increase mass transfer performance [18]. In addition to the packed distillation column, the interfacial area for the positive system in a tray distillation column also increased with the stabilized froth [17].

2EH was used as an additive to enhance absorption of water vapor by the LiBr solution film in the falling film system [19, 20]. Enhancement of heat transfer could be caused significantly by small amounts of additives during absorption process, and the enhanced degree was decided from the additive concentration and Reynolds number [19]. Besides, 2EH was also used as an additive in the system of the vertical falling film, and flat copper plate and the copper plate covered with a copper wire screen were tested by LiBr solutions with and without 2EH [20]. The experimental results showed that twice the heat transfer was enhanced by adding 2EH in LiBr-water films on the bare copper surface and approximately 2.5 and 3.5 times the mass transfer was enhanced by adding 2EH in LiBr-water films on the bare copper surface in adiabatic and water-cooled absorption, respectively. The Marangoni effect resulted from chemical absorption, which was applied for absorption of CO_2 by aqueous MEA solution in the falling film systems [21, 22]. A model was assumed that the cellular convection was driven by the gradient in surface tension, which was induced by infinitesimally small perturbations of concentration [21]. The numerical results demonstrated that the minimum gas-liquid contact time was necessary for the convection to occur, and the time turned out to be below 0.01 s. In order to measure the mass transfer rate affected by the Marangoni effect in a microreactor and to compare this rate with the value for the analogous process without Marangoni effect, a falling film microreactor (FFMR) with 29 microchannels was designed and investigated for the gas-liquid mass transfer process [22]. The appearance of the Marangoni effect in a falling film microreactor was observed, which was accompanied with absorption enhancement when increasing amine concentrations under the condition of lower partial pressures of CO_2. The experimental results also showed that a 3–6-fold increase in the absorption rate is observed for MEA concentrations in the range from 2 to 2.5 M.

For the concentric absorption system, methanol, ethanol, propanol, and acetone were added, respectively, to the water surface to induce interfacial disturbance [23]. The results showed that absorption of CO_2 was enhanced by the interfacial disturbance. Sodium lauryl sulfate (SLS) and cetyltrimethylammonium bromide (CTMAB) were used as a surfactant, respectively, to test the performance of carbon dioxide absorbed by water. Enhancement of mass transfer performance for carbon dioxide absorbed by water was demonstrated for water surface adding 20–100 wt.% aqueous solution of methanol, ethanol, and 2-propanol. Increment of mass transfer performance with the increased surfactant concentration was also observed. In addition, the ethanol vapor and the ethanol droplets from capillary were added, respectively, to the

absorption system [24]. Since the Marangoni effect was more pronounced for the concentration of LiCl greater than 40 wt.%, the experimental results showed that the removal efficiencies were increased significantly beyond 40 wt.%. Absorption enhancement was better for ethanol vapor than for ethanol droplets, which was also demonstrated.

3.2. Influences of operating variables for the presented study

As shown in **Figure 3**, the removal of H_2O by the TEG solution was decreased with the increased liquid temperature. Since the driving force for H_2O absorbed by the desiccant solution is determined by the depression of water vapor pressure, the water vapor will be transferred from the bulk gas phase with the higher vapor pressure to the gas-liquid interface with the lower vapor pressure. The vapor pressure of desiccant solution was lower for the lower liquid temperature, and the depression of water vapor pressure would be larger for the lower liquid temperature. Therefore, the lower the liquid temperature, the higher the mass transfer performance. Similarly, the vapor pressure of the TEG solution was decreased with the increased concentration, and the depression of vapor pressure was larger for the higher TEG concentration. The larger depression of vapor pressure would lead to the larger driving force for H_2O absorbed by the TEG solution. Therefore, the removal amount of H_2O increased with the increased TEG concentration, as shown in **Figure 4**. **Figure 5** showed that the removal amount of H_2O by the TEG solution decreased when the air flow rate increased. Since the amount of treated H_2O was increased with the increased air flow rate, the mass transfer performance was lowered with the increased air flow rate. On the other hand, the higher air flow rate reduced the time for water vapor exposed to the liquid surface so as to reduce the

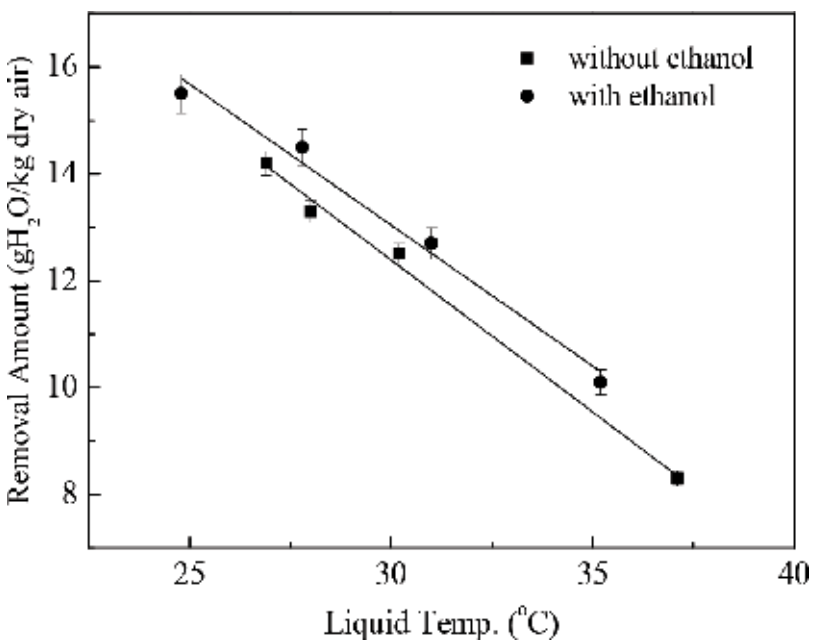

Figure 3. Effect of liquid temperature on removal amount.

exposure time and to decrease the absorption capacity. According to these points of view and the experimental results, the removal amount of H_2O by the TEG solution decreased with the larger air flow rate. In contrast, the removal amount of H_2O by the TEG solution was increased when the liquid flow rate was increased, as shown in **Figure 6**. Since the TEG solution was used as the working solution for absorption of water vapor in the gas phase, the higher mass transfer performance would be accompanied with the larger liquid flow rate. On the other hand, the larger liquid flow rate would promote the phenomenon of surface renewal. It could be thought that the absorption site increased in the packed-bed absorber and the mass transfer performance was increased. Therefore, **Figure 6** showed that the removal amount of H_2O was increased with the increased liquid flow rate. Since the explanations of the effect of operating variables on mass transfer performance for TEG solution with surfactants were similar as that for the TEG solution without surfactants, the descriptions for the mass transfer performance affected by operating variables were neglected under the condition of adding surfactants.

3.3. Influences of additives for the presented study

As shown from **Figures 3–6**, the removal amounts were always larger for the TEG solution with ethanol than without ethanol. The results can be explained by two points of views. Ethanol molecules would vaporize from the TEG thin film in the packed-bed absorber. The gradient in surface tension would result from the vaporization of ethanol, and the interfacial disturbance would be formed by the gradient in surface tension. The probability of water vapor contacted with the TEG solution film would increase with the formed interfacial disturbance. Therefore, the mass transfer performance would be enhanced by adding ethanol to the TEG solution. On

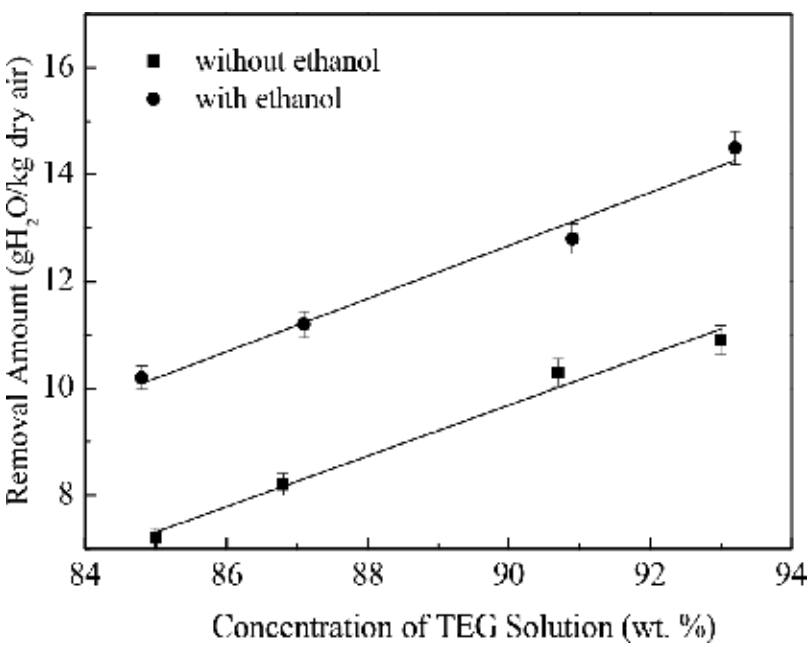

Figure 4. Effect of TEG concentrations on removal amount.

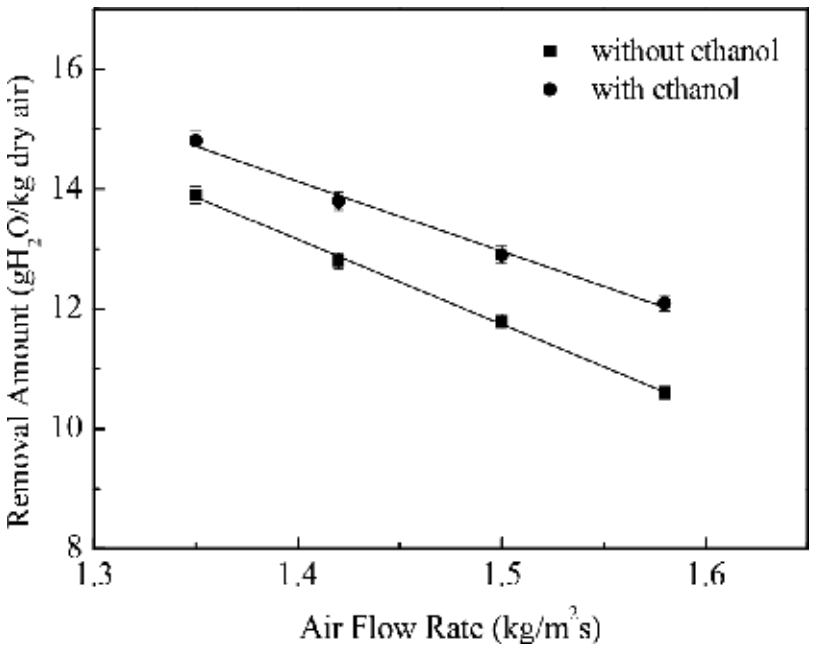

Figure 5. Effect of air flow rate on removal amount.

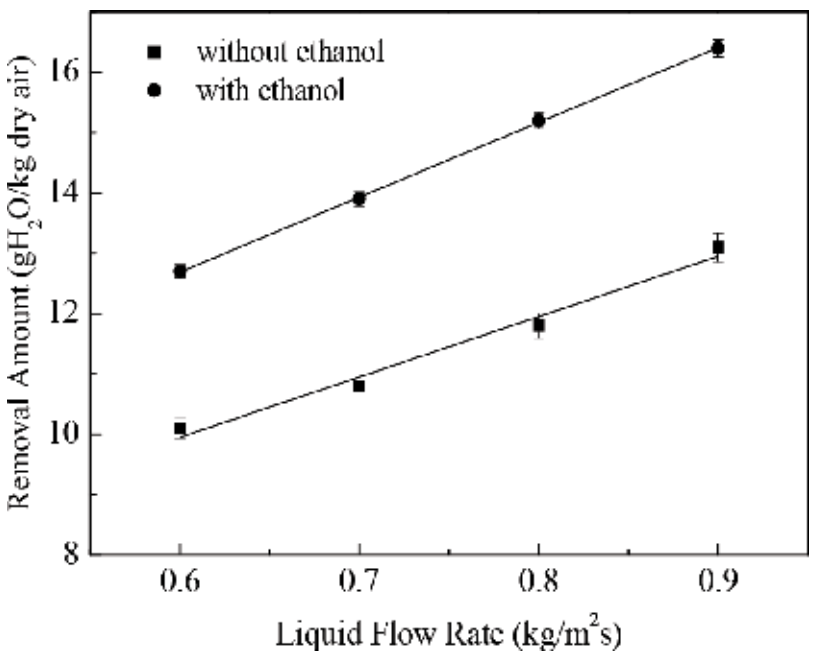

Figure 6. Effect of liquid flow rate on removal amount.

the other hand, the packing area was always not wetted completely in the absorption process. Vaporization of ethanol would be easier in the interface between the TEG-solution thin films and non-wetted packing surface, that is, the rate of vaporization of ethanol for the thinner liquid film would be larger than the thicker liquid film. Furthermore, the surface tension of the TEG solution was larger than ethanol so the surface tension of the thinner liquid film would be larger than the thicker liquid film. Therefore, the gradient in surface tension would be provoked by vaporization of ethanol, and the liquid film would be spread on the packing surface more widely. Therefore, the gas-liquid contacting area was increased and the mass transfer performance would be enhanced. Since the surface tension affected by temperature was not significant, the difference of the removal amounts with and without ethanol was smaller than other variables, as shown in **Figure 3**.

4. Conclusions

Since the interfacial fluid flow could be provoked by the surface tension gradient, the volatile matter was used as an additive in this study to discuss the effect of additive on mass transfer performance. Therefore, not only experimental mass transfer rates for water vapor absorption into the TEG solutions under different operating conditions were reported but also mass transfer performance with and without adding additives were also compared in this study. The removal amount of H_2O increased with the higher TEG concentration and liquid flow rate; however, the removal amount of H_2O decreased with the lower liquid temperature and air flow rate. Besides, the interfacial disturbance that resulted from addition of surface additive made the absorption ability of the TEG solution with ethanol higher than that without ethanol. According to the following deductions, the mass transfer performance was enhanced by adding ethanol to the TEG solution. The first is that the vaporizing ethanol would result in the surface tension gradient to form the interfacial disturbance, and the probability of gas-liquid contact is increased. The second is that the surface tension gradient would result from the vaporization of ethanol, and the formed surface tension gradient would prompt the TEG solution thin film to spread on the packing surface more widely. Therefore, the better removal amount of H_2O for the TEG solution with ethanol was demonstrated by the experimental results in this study.

Author details

Honda Wu (Hung-Ta Wu)[1]* and Tsair-Wang Chung[2]

*Address all correspondence to: hungta.wu@msa.hinet.net

1 Department of Fashion Styling and Design, Chungyu University of Film and Arts, Keelung, Taiwan, ROC

2 Department of Chemical Engineering, Chung Yuan Christian University, Taoyuan City, Taiwan, ROC

References

[1] Zarzycki R, Chacuk A. Absorption: Fundamental and Application. Oxford: Pergamon Press; 1993. DOI: 10.1002/apj.5500020219

[2] Bai G, Graham MD, Abbott NL. Role of desorption kinetics in determining Marangoni flows generating by using electrochemical methods and redox-active surfactants. Langmuir. 2005;**21**:2235-2241. DOI: 10.1021/la048238e

[3] Fanton X, Cazabat AM. Spreading and instabilities induced by a solute Marangoni effect. Langmuir. 1998;**14**:2554-2561. DOI: 10.1021/la971292t

[4] Pearson JRA. On convection cells induced by surface tension. Journal of Fluid Mechanics. 1958;**4**:489-500. DOI: 10.1017/S0022112058000616

[5] Daiguji H, Hihara E, Saito T. Mechanism of absorption enhancement by surfactant. International Journal of Heat and Mass Transfer. 1997;**40**(8):1743-1752. DOI: 10.1016/S0017-9310(96)00290-6

[6] Lu HH, Yang YM, Maa JR. On the induction criterion of the Marangoni convection at the gas/liquid interface. Industrial and Engineering Chemistry Research. 1997;**36**:474-482. DOI: 10.1021/ie960370p

[7] Kulankara S, Herold KE. Surface tension of aqueous lithium bromide with heat/mass transfer enhancement additives: The effect of additive vapor transport. International Journal of Refrigeration. 2002;**25**:383-389. DOI: 10.1016/S0140-7007(01)00013-5

[8] Koenig MS, Grossman G, Gommed K. The role of surfactant addition rate in heat and mass transfer enhancement in absorption heat pumps. International Journal of Refrigeration. 2003;**26**:129-139. DOI: 10.1016/S0140-7007(02)00012-9

[9] Kim JK, Jung JY, Kim JH, Kim MG, Kashiwagi T, Kang YT. The effect of chemical surfactants on the absorption performance during NH_3/H_2O bubble absorption process. International Journal of Refrigeration. 2006;**29**:170-177. DOI: 10.1016/j.ijrefrig. 2005.06.006

[10] Garcıa-Abuın A, Gomez-Dıaz D, Navaza JM, Sanjurjo B. Effect of surfactant nature upon absorption in a bubble column. Chemical Engineering Science. 2010;**65**:4484-4490. DOI: 10.1016/j.ces.2010.04.009

[11] Wu H. Effect of interfacial phenomena on mass transfer performance of an absorber packed closely with cylindrical packing. Chemical Engineering Journal. 2014;**240**:74-81. DOI: 10.1016/j.cej.2013.11.068

[12] Smith K, Lee A, Mumford K, Li S, Indrawan TN, Temple N, Anderson C, Hooper B, Kentisha S, Stevens G. Pilot plant results for a precipitating potassium carbonate solvent absorption process promoted with glycine for enhanced CO_2 capture. Fuel Processing Technology. 2015;**135**:60-65. DOI: 10.1016/j.fuproc.2014.10.013

[13] Skurygin EF, Poroyko TA. A simplified nonlinear model of the Marangoni instability in gas absorption. Journal of Physics: Conference Series. 2016;**710**:012036. DOI: 10.1088/1742-6596/710/1/012036

[14] Cihan E, Kavasogulları B, Demir H. Enhancement of performance of open liquid desiccant system with surface additive. Renewable Energy. 2017;**114**:1101-1112. DOI: 10.1016/j.renene.2017.08.002

[15] Patberg WB, Koers A, Steenge WDE, Drinkenburg AAH. Effectiveness of mass transfer in a packed distillation column in relation to surface tension gradients. Chemical Engineering Science. 1983;**38**(6):917-923. DOI: 10.1016/0009-2509(83)80013-X

[16] Xu ZP, Afacan A, Chuang KT. Predicting mass transfer in packed columns containing structured packings. Transactions of the Institution of Chemical Engineers. 2000;**78**:91-98. DOI: 10.1205/026387600526924

[17] Syeda SR, Afacan A, Chuang KT. Effect of surface tension gradient on froth stabilization and tray efficiency. Chemical Engineering Research and Design. 2004;**82**(A6):762-769. DOI: 10.1205/026387604774196046

[18] Wen X, Afacan A, Nandakumar K, Chuang KT. Development of a novel vertical-sheet structured packing. Chemical Engineering Research and Design. 2005;**83**(A5):515-526. DOI: 10.1205/cherd.03003

[19] Cheng WL, Kouichi H, Chen ZS, Akisawa A, Hu P, Kashiwagi T. Heat transfer enhancement by additive in vertical falling film absorption of H_2O/LiBr. Applied Thermal Engineering. 2004;**24**:281-298. DOI: 10.1016/j.applthermaleng.2003.08.013

[20] Kima DS, Infante Ferreira CA. Flow patterns and heat and mass transfer coefficients of low Reynolds number falling film flows on vertical plates: Effects of a wire screen and an additive. International Journal of Refrigeration. 2008;**32**:138-149. DOI: 10.1016/j.ijrefrig.2008.08.005

[21] Warmuziiiski K, Buzek J, Podkaiiski J. Marangoni instability during absorption reaction accompanied by chemical reaction. The Chemical Engineering Journal. 1995;**58**:151-160. DOI: 10.1016/0923-0467(94)02944-X

[22] Sobieszuk P, Pohorecki R, Cyganski P, Kraut M, Olschewski F. Marangoni effect in a falling film microreactor. Chemical Engineering Journal. 2010;**164**:10-15. DOI: 10.1016/j.cej.2010.07.053

[23] Vazquez G, Antorrena G, Navaza JM, Santos V. Absorption of CO_2 by water and surfactant solutions in the presence of induced Marangoni effect. Chemical Engineering Science. 1996;**51**(12):3317-3324. DOI: 10.1016/0009-2509(96)85979-3

[24] Yang NH, Chen YJ, Liao CC, Chung TW. Improved absorption in gs-liquid systems by the addition of a low surface tension component in the gas and/or liquid phase. Industrial and Engineering Chemistry Research. 2008;**47**:8823-8827. DOI: 10.1021/ie800316n

Chapter 6

Mass Transfer in Extractive Distillation when Using Ionic Liquids as Solvents

Esteban Quijada-Maldonado,
Wytze G. Meidersma and André B. de Haan

Additional information is available at the end of the chapter

http://dx.doi.org/10.5772/intechopen.76544

Abstract

Mass transfer efficiency study in extractive distillation with ionic liquids for the mixtures water-ethanol and toluene-methylcyclohexane has been carried out in this work. Ionic liquids for the separation of these mixtures overcome the performance of the common volatile organic solvents. However, these also showed higher viscosities. A rated-based analysis was performed in order to quantify the effect of the solvent viscosity and relative volatility on mass transfer efficiency. In addition to this, an experimental analysis of the mass transfer efficiency was carried out experimentally in an extractive distillation pilot plant. The results indicated that, high liquid viscosities of ionic liquids should not affect the mass transfer efficiency negatively if the produced relative volatilities are sufficiently higher than those produced by organic solvents. However, when the ionic liquid showed very high viscosities or this solvent was present in large concentrations inside the column, the mass transfer efficiency decreases no matter how high the relative volatility is.

Keywords: extractive distillation, ionic liquids, rate-based model, mass transfer efficiency

1. Introduction

Azeotropic and close boiling point mixtures cannot be separated by normal fractional distillation. Extractive distillation (ED) is an energy efficient technology that enables the separation of these complex mixtures by using a high boiling point solvent added at the top of the column. With this, the activity coefficients at the liquid phase are modified improving the

relative volatiles. As a result, high purity products are obtained at the top of the distillation column with low energy demand. **Figure 1** depicts a common extractive distillation process including the solvent recovery column.

An important parameter in the ED process is the solvent-to-feed ratio which is defined by the ratio of the solvent added to the column and the feed stream added to the column on mass basis:

$$S/F = \text{solvent feed stream/feed stream} \quad (1)$$

The common solvents used in industry are normally of organic nature such as ethyleneglycol for separating water and ethanol [1–3], phthalic anhydride [4], *N*-methyl-pyrrolidone (NMP) and sulfolane [5–7] for the separation of aromatic from aliphatic and 1,3 butadiene from C_4 hydrocarbons, 1,2 propanediol [8, 9], 1,4 butanediol [10] or dimethyl sulfoxide [11] for the dehydration of tetrahydrofuran among other separations. These organic solvents show several drawbacks. Since the solvent is added at the top of the column and the organic solvents are volatile, they reduce the product purity. Besides this, large amounts of solvent are required to achieve certain separation. Lately, a new class of solvents called ionic liquids have been proposed as a novel solvent for ED due to their properties such us negligible vapor pressure and high selectivity in separation processes. Therefore, a non-volatile solvent is added to the column producing free solvent products in the condenser. Lately, many works have been published regarding the separation of azeotropes and close boiling point mixtures using ionic liquids as solvent, most of them are related to vapor-liquid equilibrium evaluation of ionic liquids for improving relative volatilities [12–22]. Here, it has been demonstrated that, in general, ionic liquids can produce better relative volatilities than organic solvents [22–25]. This advantage results in less solvent needed to perform the separation which brings less operational cost, or an ED column with less separation stages or a decrease in capital cost with regard a conventional ED column operating with organic solvents [26].

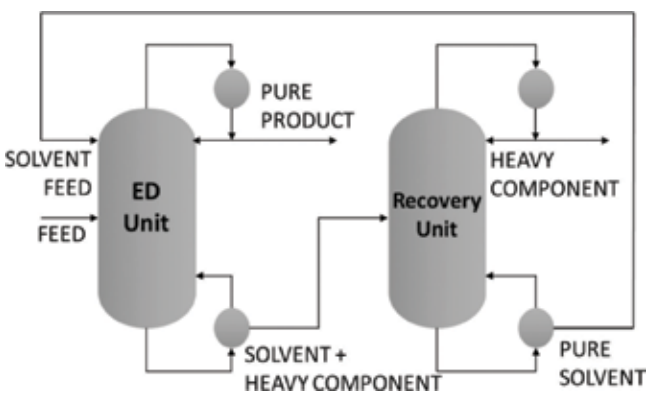

Figure 1. Scheme of a conventional extractive distillation unit and the solvent recovery step.

However, ionic liquids also show high viscosities. For example, one of the less viscous ionic liquids, 1-ethyl-3-metylimidazolium dicyanamide ([emim][DCA]), shows viscosities around 15 mPa·s at 298.15 K [27–30]. Nevertheless, ionic liquids containing halides as anion, such as chloride [I] or bromide [Br], exhibit much larger viscosities than the previous anion. For instance, the ionic liquid 1-octyl-3-methylimidazolium bromide ([omim][Br]) displays a viscosity of around 5000 mPa·s at 298.15 K [31] while 1-octyl-3-methylimidazolium chloride ([omim][Cl]) a value of 20.000 mPa·s at 298.15 K [32, 33]. These viscosity values could bring a decrease in mass transfer efficiency when using ionic liquids in extractive distillation.

Because of this, an ED column with more separation stages due to the mass transfer limitations will be required masking the above gained advantages provided by ionic liquids. However, a good point is that, the viscosity of ionic liquids drastically decreases with increasing the temperature [27] and since ED is a thermal separation process, the real mass transfer effects of ionic liquid on the separation need to be evaluated.

Therefore, the main aim of this work is to evaluate the decrease in mass transfer throughout the mass transfer efficiency concept when using ionic liquids in the extractive distillation of two important cases: separation of water ethanol and methylcyclohexane-toluene mixtures. The first represents the industrial case of dehydration of ethanol and the second the separation of aromatics from aliphatic in the petrochemical industry. On the other hand, the mass transfer efficiency will be evaluated using rate-based modeling or non-equilibrium stage modeling [34] since, on contrary of the equilibrium model, this one considers a real separation stage which is limited by the mass transfer. Therefore, the effect of the viscosity of ionic liquids of mass transfer efficiency would be quantified by this model. Finally, an experimental evaluation of the decrease in mass transfer efficiency is performed in an ED pilot plant equipped with structured packing.

2. Ionic selection for water: ethanol and toluene: methylcyclohenene separation

As it was mentioned above, ionic liquids show better performance than organic solvents in terms of vapor–liquid equilibrium. Therefore, the selection of the ionic liquids for a certain case study is based on the increase in relative volatility. The work of Ge et al. [23] shows an experimental selection of ionic liquids for water-ethanol separation. On the other hand, Gutierrez-Hernandez et al. [25] carried out a selection of ionic liquids for methylcyclohexane-toluene separation based on liquid-liquid extraction experiments. Nevertheless, the high viscosities of ionic liquids could limit the mass transfer in the ED column. **Table 1** contains experimentally determined relative volatilities and viscosities for both case studies.

It can be observed in **Table 1** that the selected ionic liquids for the separation of the water-ethanol mixture, 1-ethyl-3-methylimidazolium chloride ([emim][Cl) and 1-ethyl-3-methylimidazolium acetate ([emim][OAc]) showed higher produced relative volatilities than the conventional organic solvent ethylene glycol (EG). For the second case, the ionic liquid

	α		η/mPa s	
Solvent	S/F = 1	Ref.	T = 298.15 K	Ref.
Water-ethanol separation [35]				
[emim][Cl]	2.62	[23]	2597.69[a]	[36]
[emim][OAc]	2.24	[23]	132.9	[27]
[emim][DCA]	1.89	[23]	14.9	[27]
EG	1.83	Aspen®	16.6	[37]
Methylcyclohexane-toluene separation [38]				
	α		η/ mPa s	
	S/F = 5	Ref	T = 298.15 K	Ref.
[hmim][TCB]	9.4	[25]	47.8	[38]
NMP	2.8	Aspen®	1.9	Aspen®

[a]extrapolated value from experimental data.

Table 1. Relative volatilities at a solvent-to-feed (S/F) ratio (mass basis) for different solvents and pure solvent viscosities (η) at T = 298.15 for both case studies.

1-hexyl-3-methylimidazolium tetracyanoborate ([hmim][TCB]) produced much higher relative volatilities than organic solvent. This is an indication that, a column with less separation stages or a less usage of solvent is expected to achieve a good separation. However, ionic liquids also show higher viscosity values than traditional solvents. Therefore, the mass transfer efficiency is expected to decrease.

3. Rate-based mass transfer efficiency analysis

To evaluate the effect of viscosity on mass transfer in the extractive distillation process with ionic liquids, it is necessary to use the concept of mass transfer efficiency. The most used mass transfer efficiency model is the Murphree Tray Efficiency [39]. However, this calculation requires the vapor composition per tray and this would not reflect the decrease in mass transfer due to viscosity in the liquid phase. The concept of efficiency that represents the changes in liquid phase viscosity is the tray efficiency defined from the point efficiency assuming that there is no concentration gradient in the axial direction [34, 40], this is:

$$E_{OV} = 1 - \exp(-N_{OV}) \tag{2}$$

where E_{OV} is the tray efficiency and N_{OV} is the overall number of transfer units which is calculated from the number of transfer units in the vapor phase (N_V) and in the liquid phase (N_L) as follows:

$$\frac{1}{N_{OV}} = \frac{1}{N_V} + \frac{\Lambda}{N_L} \tag{3}$$

where Λ is the stripping factor calculated from an activity coefficient model [23]. When using packing as internal in an ED column the mass transfer efficiency can be determined using the concept of height equivalent to a theoretical plate:

$$HETP = H_{OV}\frac{\ln(\Lambda)}{\Lambda - 1} \tag{4}$$

where H_{OV} is overall height of transfer units calculated from transfer height id the vapor phase (H_V) and in the liquid phase (H_L) as follows:

$$H_{OV} = H_V + \Lambda H_L \tag{5}$$

Equations (2)–(5) describe the changes in efficiency with physical properties, vapor-liquid equilibrium and the column internals. These equations are used to compare the mass transfer efficiency performance of the different solvents studied in this work. The number of transfer units and the height of transfer units are calculated using the mass transfer correlations depending on the column internal. This work is focused on two internals to evaluate the changes in mass transfer efficiency with viscosity: sieve trays and structured packing. For the case of sieve trays, AIChE mass transfer correlation calculates the number of transfer units in the liquid phase [41]:

$$N_L = 19700\,(D_L)^{0.5}(0.4\,F_S + 0.17)\,t_L \tag{6}$$

where t_L is the liquid phase residence time, F_S the superficial factor, and D_L the Fick diffusion coefficient. This last transport property accounts for the decrease in mass transfer efficiency due to the high liquid phase viscosity and it is calculated using the Wilke-Chang correlation [42]:

$$D_{12} = 7.4x\,10^{-12}\frac{(\Phi\,M_{W,2})^{0.5}\,T}{\eta_2\,V_1^{0.6}} \tag{7}$$

where $M_{W,2}$ is the molecular weight if the solvent, Φ is the association factor, T is the temperature, V_1 is the molar volume of the solute at its normal boiling point and η_2 is the viscosity of the solvent. To use this diffusion coefficient in the above correlation, a mixing rule has to be previously applied for concentrated solutions [34]. For the case of structured packings, Rocha mass transfer correlation describes well the height of transfer units in the liquid phase [43]:

$$H_L = \frac{u_L}{2a\left[\frac{D_L\,u_{Le}}{\pi S C_E}\right]^{0.5}} \tag{8}$$

where u_L is the superficial liquid phase velocity, a is the interfacial area per volume, u_{Le} is the effective liquid phase velocity, S is the side dimension of corrugation and C_E is a constant for surface renewal.

4. Simulation setup

ASPEN Plus® radfrac with the Rate-Sep package enables the use of the rate-based model to evaluate the effect of the solvent on the mass transfer efficiency in the ED process. This model needs physical and transport properties of both pure component and ternary mixture which were taken elsewhere [27, 37, 44]. Column internals are other parameters that have to be defined. Sieve trays and Mellapak® 250Y are the selected internals for this study. **Table 2** summarized the features of these internals. These internals will be used to analyze the separation of water-ethanol.

It is worth to mention that, vapor flow regimes inside the ED column could also affect mass transfer efficiency. However, to avoid this effect, these flow regimes were set constant at a value of flooding of 70%.

Sieve Tray	
Parameter	**Value**
Number of stages (real stages including reboiler and condenser)	22
Feed tray	12
Solvent feed	2
Mellapak® 205Y structured packing	
Parameter	**Value**
Packing height (m)	6
Feed point (m)	3
Packing material	Stainless steel

Table 2. Used column internal characteristics in the simulations for 100 kg/h of mixture and 50% wt ethanol as a base flow and feeding concentration respectively [35].

5. Experiments with an extractive distillation pilot plant

In this work, the analysis of mass transfer efficiency will be carried out also experimentally for the mixture toluene-methylcyclohexane to corroborate the results obtained from Aspen Plus®. For this purpose, a pilot-scale ED pilot plant was constructed at Eindhoven University of Technology, The Netherlands equipped with Mellapack® 750Y structured packing and that operates in continuous mode. The column diameter is 0.049 m and the packing material is stainless steel. Finally, the packing height is 3.12 m. To validate the rate-based model with experimental data from the pilot plant, collector basins and thermocouples were placed within packing segments to collect liquid samples a measure the concentration of all the component in the column at defined height of the column. **Figure 2**, shows a scheme of the constructed ED pilot plant. The experimental operating conditions are described in **Table 3**.

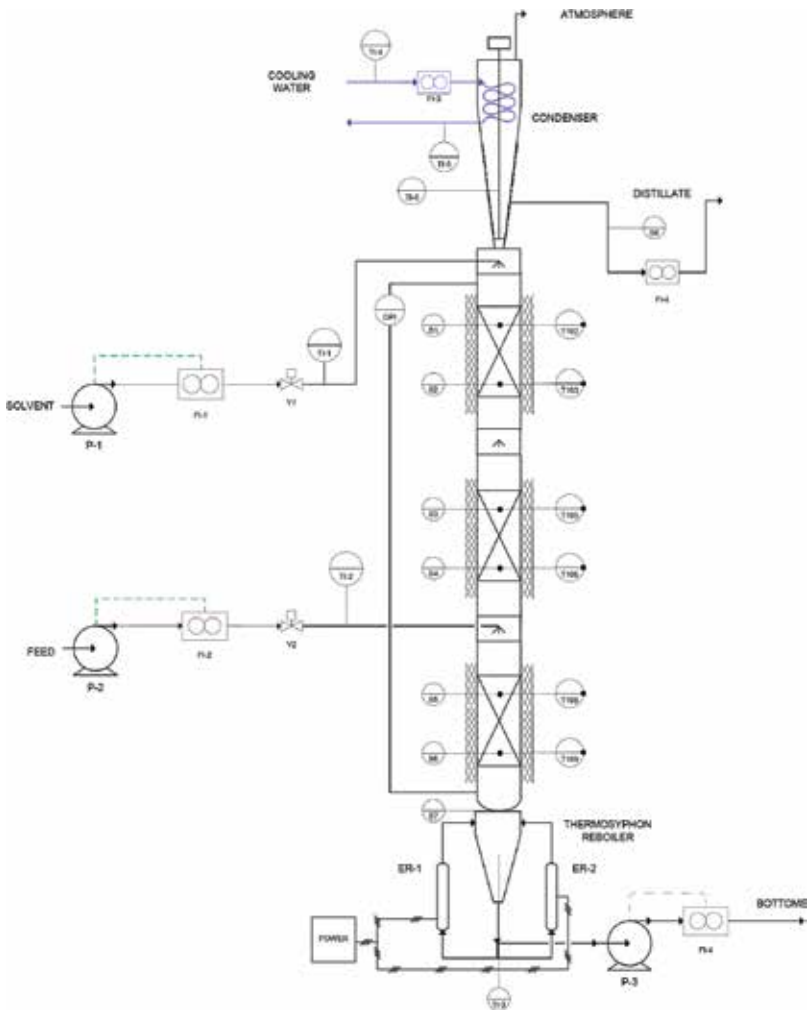

Figure 2. Scheme of the extractive distillation pilot plant at Eindhoven University of Technology [38].

Variable		Value	
Feed flow rate [kg h^{-1}]		2	
Toluene concentration at feed [wt%]		70	
Feed temperature [°C]		90	
Solvent temperature [°C]		100	
Solvent-to-feed ratio (mass)		5	
	Solvent	Reboiler duty [kW][a]	Distillate rate [kg h^{-1}]
	NMP	50%	0.3
	[emim][TCB]	50%	0.3

[a]100% = 2.04 [kW].

Table 3. Operating conditions [38].

6. Results and discussion

6.1. Mass transfer efficiency in sieve tray column

Figure 3 shows the generated relative volatility profile along the ED column that accounts for how good the separation is.

Before analysis these results, it has to be clarified that, the concentration of the solvent, either the organic solvent or the ionic liquids, is higher in the rectifying section than in the stripping section. It means from stage 2 to 12 in our ED column. This is because the solvent feed is at the top of the column and below the solvent is diluted by the feed stream at stage 12. Having mentioned this, it can be observed in **Figure 3** that the relative volatility profiles, in general, follow the same trend as **Table 1** where the ionic liquid [emim][Cl] showed the best values being the most promising solvent for water-ethanol, separation. In spite of these results, this ionic liquid would not be used in a real ED column due that it is a corrosive fluid [45] and the melting point is 87°C [46]. Anyhow, this ionic liquid will be kept for the analysis. Therefore, [emim][OAc] becomes the most promising ionic liquid which exhibits the second best relative volatilities. On the other hand, EG produces the lowest relative volatility values as indicated in **Table 1**.

Next, **Figure 4**, shows the viscosity profile at the liquid phase when using the different solvent. It is clearly seen that the increase in the liquid phase viscosity inside the ED column is directly influenced by the solvent viscosity. This explains why when using [emim][Cl] as the solvent the highest viscosity values are observed inside the column and the rest of the solvent follow the trend in **Table 1**. Therefore, the trend observed in this figure is as follows: [emim][Cl] > [emim][OAc] > [emim][DCA] > EG. In the stripping section the liquid viscosity drops for all four solvents as the solvent concentration is reduced by dilution with the feed stream.

As a summary, ionic liquids produced higher relative volatilities that the organic solvent, but higher viscosities as well. **Figure 5** shows the mass transfer efficiency profiles along the column for all solvents.

Figure 5 shows the tray efficiency profiles over the ED column calculated using Eq. (2). The rectifying section shows lower mass transfer efficiencies than the stripping section due to the effect of solvent viscosity. At S/F = 1, the mass transfer efficiency order is [emim][OAc] > [emim][DCA] > EG > [emim][Cl]. This order does not follow exactly the expected trend from **Figure 4**. Therefore, the viscosity is not the only important effect in calculating the mass transfer efficiency as observed in Eq. (2). Hence, the relative volatility values should play an important role as well. Ionic liquids are able to outperform the relative volatilities of the common organic solvents as it has previously mentioned. In **Table 1** it is observed that very good relative volatilities are produced by [emim][OAc]. This property enhances the mass transfer efficiency even though having relatively high viscosity. However, for then case of [emim][Cl], this ionic liquid shows the highest relative volatility and also it exhibits high viscosities. Here, due to the high viscosities this property is more important than

http://dx.doi.org/10.5772/intechopen.76544

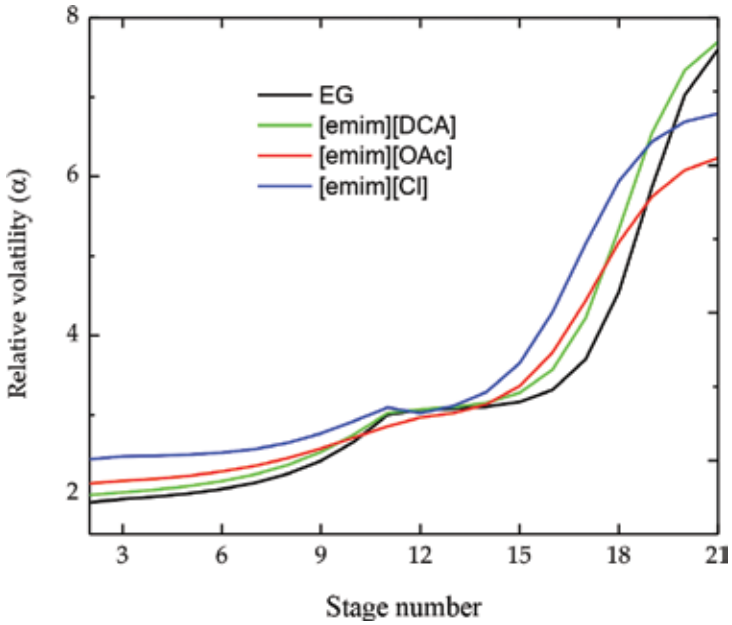

Figure 3. Relative volatility profiles along the extractive distillation column for S/F = 1.

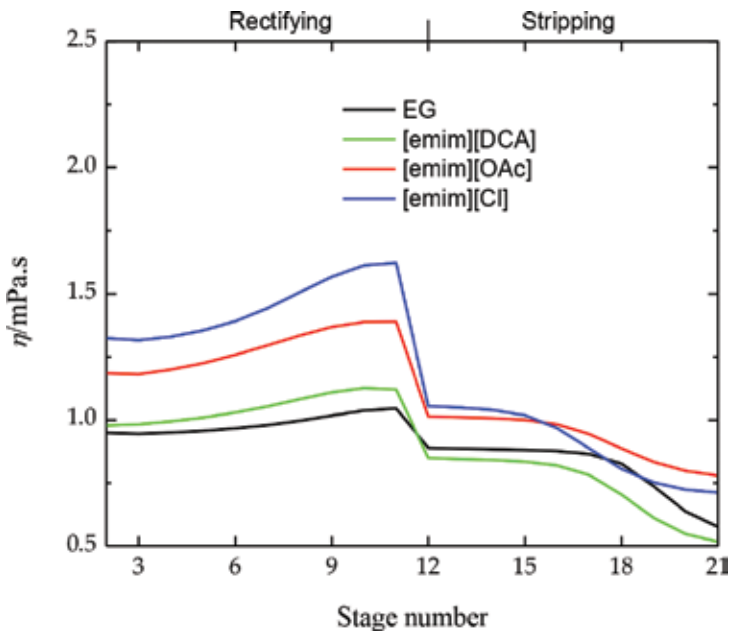

Figure 4. Viscosity profiles along the column for S/F = 1 formed when the different solvents are added to the column and D/F = 0.4 (mass basis) [35].

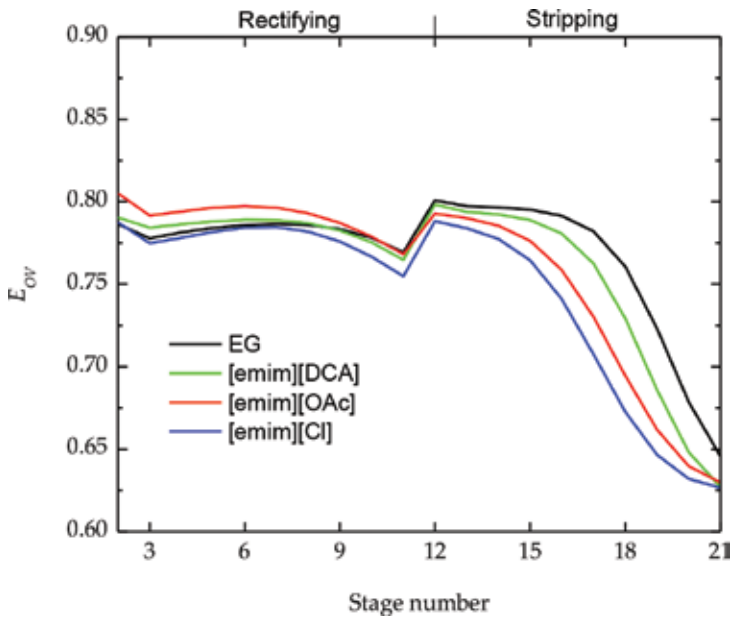

Figure 5. Tray efficiency profiles along the column for S/F = 1 calculated when the different solvents are added to the column and D/F = 0.4 (mass basis). The column is numbered from the top to the bottom [35].

relative volatility and becomes the limiting factor in mass transfer efficiency. Therefore, moderately high viscosities of ionic liquids in ED would not limit the mass transfer when combined with high values of relative volatility. However, the relative volatility does not enhance mass transfer efficiency sufficiently in the presence of a very viscous ionic liquid.

6.2. Mass transfer efficiency in Mellapack® 250Y structured packing

Figure 6 shows the generated Height Equivalent to a Theoretical Plate (HETP) profiles along the column for the same operating conditions as the sieve tray column.

For the structured packing, the values of mass transfer efficiency are represented the HETP, and here the lowest value means the most efficient case. The mass transfer efficiency order is [emim][OAc] > [emim][DCA] ≈ [emim][Cl] > EG in the rectifying section. The observation of these profiles does not produce different conclusions from sieve trays. However, two important points are observed here. Firstly, in contrast to sieve trays, more notorious difference in efficiency is shown here. This is explained by the fact that in packed columns the liquid and vapor flow are in countercurrent and the packing surface allows an intimate vapor-liquid contact. As a result, the packed distillation column operates closer to equilibrium than sieve trays, and thereby the effect of the relative volatility predominates over the increase in liquid phase viscosity. This is the reason why [emim][Cl] produces now better mass transfer efficiencies than EG on contrary to the case of the sieve tray column and this latter solvent presents the lowest mass transfer efficiency (highest *HETP*). It worth to mention that, the results obtained here were previously validated in a pilot plant where that developed rate-based model predicts the performance of the pilot plant within 10% error.

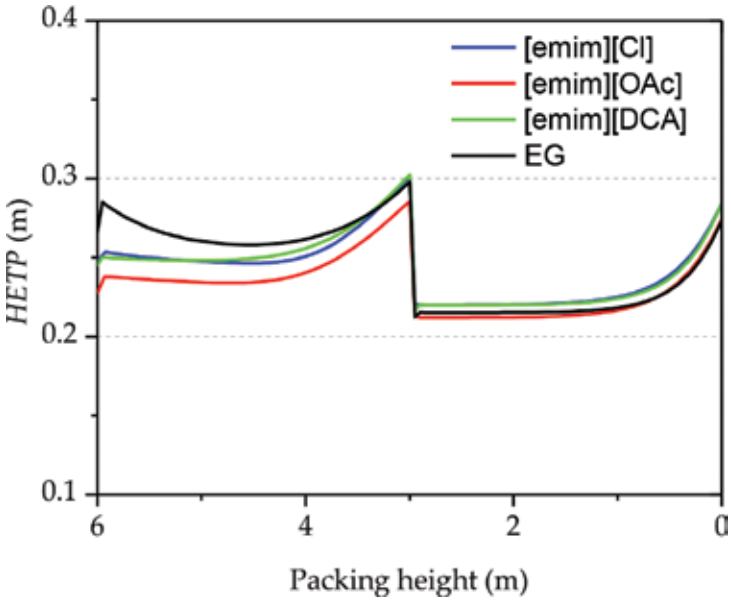

Figure 6. HETP profiles along the column for S/F = 1 (mass basis) calculated when the different solvents are added to the column and D/F = 0.4 (mass basis). The column is measured from the bottom (0 m) to the top (6 m) [35].

6.3. Experimental study of mass transfer efficiency in the system toluene-methylcyclohexane

The extractive distillation of toluene-methylcyclohexane is an interesting case because the ionic liquid [hmim]TCB] overcome by far the relative volatility of the conventional organic solvent NMP (see **Table 1**). In addition to this, the viscosity of the ionic liquid is not as high as [emim][OAc] for example. Therefore, one would not expect a decrease in mass transfer efficiency as it was concluded before. However, since this is a very nonpolar mixture and the ionic liquid is a solvent of a polar nature, phase split is expected when mixing. Nevertheless, the phase splitting can be solved by increasing the S/F ration at high values [25]. Due to this fact, there could be a decrease in mass transfer efficiency. **Figure 7** shows the ternary map indicating the one-phase region to operate.

As it can be observed in **Figure 7**, to reach the one-phase region, two conditions should be set: first, high concentration of [hmim][TCB] inside the column and high methylcyclohaxene distillate rates (or low reflux ratios) to keep its concentration as low as possible inside the column to avoid phase split. **Figure 8** shows the experimentally obtained liquid phase concentration profiles when NMP (**Figure 8a**) and [hmim][TCB] (**Figure 8b**) where the solvent, respectively.

It can be observed that, due to the high S/F ratios, high solvent concentration was developed inside the ED column for both cases NMP and [hmim][TCB]. However, when using the organic solvent, a little lower liquid phase solvent concentration is observed due to this solvent is volatile. High concentration will lead to high liquid phase viscosities. **Figure 9** shows the viscosity profiles inside the column and the Height Equivalent to a Theoretical Plate (HETP).

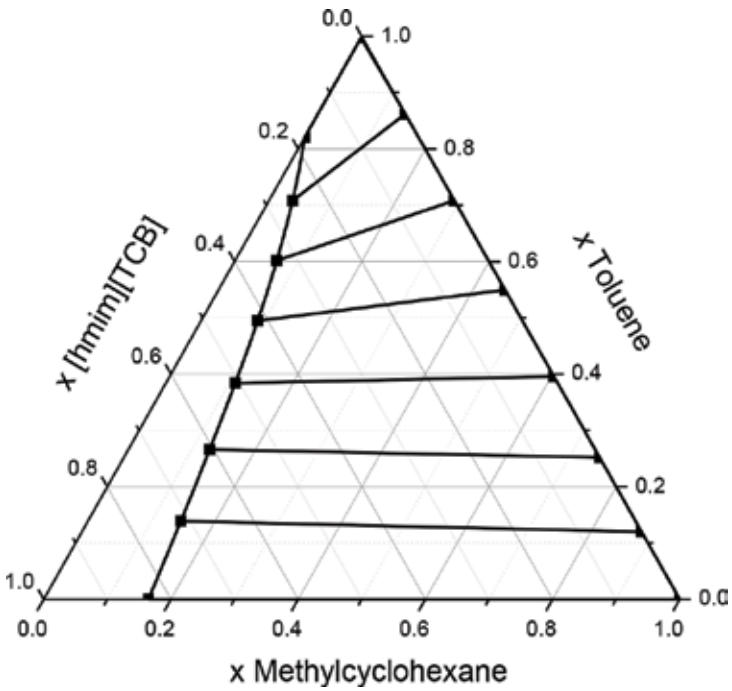

Figure 7. Ternary diagram for the system toluene-methylcylcohexane-[hmim][TCB] [38].

In **Figure 9a** it can be clearly observed the influence of the viscosity of [hmim][TCB] due to the high S/F ratios. While the separation of the toluene-methylcyclohexane mixture with NMP show low viscosities, [hmim][TCB] exhibit high values reaching the 4 [cP] in the rectifying section leading to a decrease in mass transfer efficiency as observed in **Figure 9b**. The impact of the liquid phase resistance on the mass transfer efficiency is significant even though the use of the first solvent produces much higher relative volatilities. The conclusions made in this

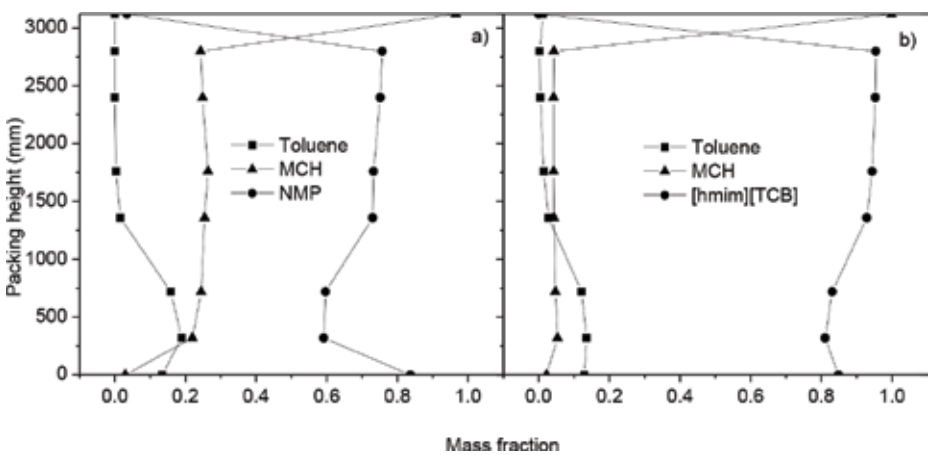

Figure 8. Concentration profiles (mass fractions) for the ED of toluene-MCH using (a) NMP and (b) [hmim][TCB] as solvents. For cases 1 and 2 [38].

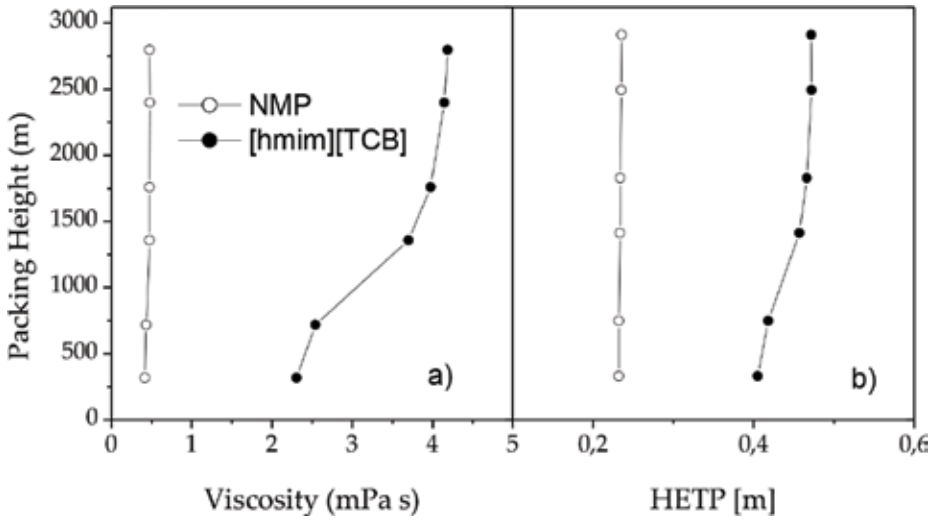

Figure 9. Liquid phase viscosity inside the ED column and HETP for the system toluene-methylcyclohexane using both solvent NMP and [hmim][TCB] [38].

work should be used in the selection of the ionic liquids for extractive distillation processes along with the studies on relative volatility.

7. Conclusions

In this study, the mass transfer efficiency of the extractive distillation with ionic liquids has been analyzed for the water ethanol mixtures using a developed rate-based model and in a pilot plant scale extractive distillation column.

The results from the rate-based indicated that the use of ionic liquids as solvents in ED is beneficial due to the increase in relative volatilities when compared to organic solvents.

The high viscosities of ionic liquids were reflected in the increase of que liquid phase viscosity inside the ED column. However, this viscosity did not decrease the mass transfer efficiency of the ED whereas the relative volatilities are high. On the other hand, when very high viscosities or high solvent to feed ratios are applied to the ED column, a decrease in mass transfer efficiency was observed even though having high relative volatilities.

Acknowledgements

Project Erasmus Mundus Chile, Project FONDECYT 11150417 and Project RC-130006-CILIS granted by Fondo de Innovación para la Competitividad, del Ministerio de Economía, Fomento y Turismo, Chile are kindly acknowledged for funding this book chapter.

Referenced tables and figures were taken from Computer & Chemical Engineering Journal and from Separation & Purification Technology Journal.

Author details

Esteban Quijada-Maldonado[1]*, Wytze G. Meidersma[2] and André B. de Haan[3]

*Address all correspondence to: esteban.quijada@usach.cl

1 University of Santiago de Chile, Santiago, Chile

2 Eindhoven University of Technology, Eindhoven, The Netherlands

3 Delft University of Technology, Delft, The Netherlands

References

[1] Meirelles A, Weiss S, Herfurth H. Ethanol dehydration by extractive distillation. Journal of Chemical Technology and Biotechnology. 1992;**53**:181-188. DOI: 10.1002/jctb.280530213

[2] Ravagnani MASS, Reis MHM, Filho RM, Wolf-Maciel MR. Anhydrous ethanol production by extractive distillation: A solvent case study. Process Safety and Environmental Protection. 2010;**88**:67-73. DOI: 10.1016/j.psep.2009.11.005

[3] Benyahia K, Benyounes H, Shen W. Energy evaluation of ethanol dehydration with glycol mixture as entrainer. Chemical Engineering and Technology. 2014;**37**:987-994. DOI: 10.1002/ceat.201300872

[4] Berg L. Separation of benzene and toluene from close boiling nonaromatics by extractive distillation. AICHE Journal. 1983;**29**:961-966. DOI: 10.1002/aic.690290614

[5] Wang Q, Zhang BJ, He C, He CC, Chen QL. Optimal design of a new aromatic extractive distillation process aided by a co-solvent mixture. Energy Procedia. 2017;**105**:4927-4934. DOI: 10.1016/j.egypro.2017.03.984

[6] Kim YH, Kim SY, Lee B. Simulation of 1,3-butadiene extractive distillation process using N-methyl-2-pyrrolidone solvent. Korean Journal of Chemical Engineering. 2012;**29**:1493-1499. DOI: 10.1007/s11814-012-0075-3

[7] Jalali F, Saffari R. Simulation and optimization in 1,3-butadiene process from C4-CUT using genetic algorithm. in: Marquardt W, Pantelides C, editors. Computer Aided Chemical Engineering. 16th European Symposium on Computer Aided Process Engineering and 9th International Symposium on Process Systems Engineering. 21st ed. Elsevier; 2006. pp. 901-906. DOI: 10.1016/S1570-7946(06)80160-4

[8] Xu S, Wang H. Separation of tetrahydrofuran-water azeotropic mixture by batch extractive distillation process. Chemical Engineering Research and Design. 2006;**84**:478-482. DOI: 10.1205/cherd05050

[9] Deorukhkar OA, Deogharkar BS, Mahajan YS. Purification of tetrahydrofuran from its aqueous azeotrope by extractive distillation: Pilot plant studies. Chemical Engineering and Processing: Process Intensification. 2016;**105**:79-91. DOI: 10.1016/j.cep.2016.04.006

[10] Xu S, Wang H. A new entrainer for separation of tetrahydrofuran-water azeotropic mixture by extractive distillation. Chemical Engineering and Processing: Process Intensification. 2006;**45**:954-958. DOI: 10.1016/j.cep.2006.02.001

[11] Zhang Z, Huang D, Peng M, Sun D, Li W. Entrainer selection for separating tetrahydrofuran/water azeotropic mixture by extractive distillation. Separation and Purification Technology. 2014;**122**:73-77. DOI: 10.1016/j.seppur.2013.10.051

[12] Fang J, Liu J, Li C, Liu Y. Isobaric vapor-liquid equilibrium for the acetonitrile + water system containing different ionic liquids at atmospheric pressure. Journal of Chemical & Engineering Data. 2013;**58**:1483-1489. DOI: 10.1021/je3009792

[13] Li X, Shen C, Li C. Effect of alkanolammonium formates ionic liquids on vapour liquid equilibria of binary systems containing water, methanol, and ethanol. The Journal of Chemical Thermodynamics. 2012;**53**:167-175. DOI: 10.1016/j.jct.2012.05.001

[14] Zhao J, Dong C, Li C, Meng H, Wang Z. Isobaric vapor-liquid equilibria for ethanol-water system containing different ionic liquids at atmospheric pressure. Fluid Phase Equilibria. 2006;**242**:147-153. DOI: 10.1016/j.fluid.2006.01.023

[15] Khan I, Batista MLS, Carvalho PJ, Santos LMNB, Gomes JRB, Coutinho JAP. Vapor-liquid equilibria of imidazolium ionic liquids with cyano containing anions with water and ethanol. The Journal of Physical Chemistry. B. 2015;**119**:10287-10303. DOI: 10.1021/acs.jpcb.5b03324

[16] Tsanas C, Tzani A, Papadopoulos A, Detsi A, Voutsas E. Ionic liquids as entrainers for the separation of the ethanol/water system. Fluid Phase Equilibria. 2014;**379**:148-156. DOI: 10.1016/j.fluid.2014.07.022

[17] Gjineci N, Boli E, Tzani A, Detsi A, Voutsas E. Separation of the ethanol/water azeotropic mixture using ionic liquids and deep eutectic solvents. Fluid Phase Equilibria. 2016;**424**:1-7. DOI: 10.1016/j.fluid.2015.07.048

[18] Shen C, Li X, Lu Y, Li C. Effect of ionic liquid 1-methylimidazolium chloride on the vapour liquid equilibrium of water, methanol, ethanol, and {water+ethanol} mixture. The Journal of Chemical Thermodynamics. 2011;**43**:1748-1753. DOI: 10.1016/j.jct.2011.06.002

[19] Li W, Li L, Zhang L, Li H, Zhang T. Isobaric vapor-liquid equilibrium for 2-butanone + ethanol + phosphate-based ionic liquids at 101.3-kPa. Fluid Phase Equilibria. 2018;**456**:57-64. DOI: 10.1016/j.fluid.2017.10.001

[20] Cumplido M, Lladosa E, Loras S, Pla-Franco J. Isobaric vapor-liquid equilibria for extractive distillation of 1-propanol+water mixture using thiocyanate-based ionic liquids. The Journal of Chemical Thermodynamics. 2017;**113**:219-228. DOI: 10.1016/j.jct.2017.06.014

[21] Chen X, Yang B, Abdeltawab AA, Al-Deyab SS, Yu G, Yong X. Isobaric vapor-liquid equilibrium for acetone + methanol + phosphate ionic liquids. Journal of Chemical & Engineering Data. 2015;**60**:612-620. DOI: 10.1021/je5007373

[22] Jongmans MTG, Schuur B, de Haan AB. Ionic liquid screening for ethylbenzene/styrene separation by extractive distillation. Industrial and Engineering Chemistry Research. 2011;**50**:10800-10810. DOI: 10.1021/ie2011627

[23] Ge Y, Zhang L, Yuan X, Geng W, Ji J. Selection of ionic liquids as entrainers for separation of (water+ethanol). The Journal of Chemical Thermodynamics. 2008;**40**:1248-1252. DOI: 10.1016/j.jct.2008.03.016

[24] Pereiro AB, Araujo JMM, Esperanza JMSS, Marrucho IM, Rebelo LPN. Ionic liquids in separations of azeotropic systems—A review. The Journal of Chemical Thermodynamics. 2012;**46**:2-28. DOI: 10.1016/j.jct.2011.05.026

[25] Gutierrez JP, Meindersma W, de Haan AB. Binary and ternary (liquid+liquid) equilibrium for {methylcyclohexane (1)+toluene (2)+1-hexyl-3-methylimidazolium tetracyanoborate (3)/1-butyl-3-methylimidazolium tetracyanoborate (3)}. The Journal of Chemical Thermodynamics. 2011;**43**:1672-1677. DOI: 10.1016/j.jct.2011.05.029

[26] Lei Z, Li C, Chen B. Extractive distillation: A review. Separation and Purification Reviews. 2003;**32**:121-213. DOI: 10.1081/SPM-120026627

[27] Quijada-Maldonado E, van der Boogaart S, Lijbers JH, Meindersma GW, de Haan AB. Experimental densities, dynamic viscosities and surface tensions of the ionic liquids series 1-ethyl-3-methylimidazolium acetate and dicyanamide and their binary and ternary mixtures with water and ethanol at T = (298.15 to 343.15K). The Journal of Chemical Thermodynamics. 2012;**51**:51-58. DOI: 10.1016/j.jct.2012.02.027

[28] Larriba M, Navarro P, Garcia J, Saffari R, Rodríguez F. Liquid-liquid extraction of toluene from heptane using [emim][DCA], [bmim][DCA], and [emim][TCM] ionic liquids. Industrial and Engineering Chemistry Research. 2013;**52**:2714-2720. DOI: 10.1021/ie303357s

[29] Freire MG, Teles AR, Rocha MAA, Schröder B, Neves CMSS, Carvalho PJ, Evtuguin DV, Santos LMNB, Coutinho JAP. Thermophysical characterization of ionic liquids able to dissolve biomass. Journal of Chemical & Engineering Data. 2011;**56**:4813-4822. DOI: 10.1021/je200790q

[30] Neves CMSS, Kurnia KA, Coutinho JAP, Marrucho IM, Lopes JNC, Freire MG, Rebelo LP. Systematic study of the thermophysical properties of imidazolium-based ionic liquids with cyano-functionalized anions. The Journal of Physical Chemistry. B. 2013;**117**:10271-10283. DOI: 10.1021/jp405913b

[31] Nanda R, Rai G, Kumar A. Interesting viscosity changes in the aqueous urea-ionic liquid system: Effect of alkyl chain length attached to the cationic ring of an ionic liquid. Journal of Solution Chemistry. 2015;**44**:742-753. DOI: 10.1007/s10953-015-0320-6

[32] Gomez E, Gonzalez B, Dominguez A, Tojo E, Tojo J. Dynamic viscosities of a series of 1-alkyl-3-methylimidazolium chloride ionic liquids and their binary mixtures with water at several temperatures. Journal of Chemical & Engineering Data. 2006;**51**:696-701. DOI: 10.1021/je050460d

[33] AlTuwaim MS, Alkhaldi KHAE, Al-Jimaz ALS, Mohammad AA. Temperature dependence of physicochemical properties of imidazolium-, pyroldinium-, and phosphonium-based ionic liquids. Journal of Chemical & Engineering Data. 2014;**59**:1955-1963. DOI: 10.1021/je500093z

[34] Taylor R, Krishna R. Multicomponent Mass Transfer. Toronto: Wiley; 1993. ISBN: 9780471574170

[35] Quijada-Maldonado E, Meindersma GW, de Haan AB. Ionic liquid effects on mass transfer efficiency in extractive distillation of water-ethanol mixtures. Computers & Chemical Engineering. 2014;**71**:210-219. DOI: 10.1016/j.compchemeng.2014.08.002

[36] Fendt S, Padmanabhan S, Blanch HW, Prausnitz JM. Viscosities of acetate or chloride-based ionic liquids and some of their mixtures with water or other common solvents. Journal of Chemical & Engineering Data. 2011;**56**:31-34. DOI: 10.1021/je1007235

[37] Quijada-Maldonado E, Meindersma GW, de Haan AB. Viscosity and density data for the ternary system water(1)-ethanol(2)-ethylene glycol(3) between 298.15K and 328.15K. The Journal of Chemical Thermodynamics. 2013;**57**:500-505. DOI: 10.1016/j.jct.2012.08.024

[38] Quijada-Maldonado E, Meindersma GW, de Haan AB. Pilot plant study on the extractive distillation of toluene-methylcyclohexane mixtures using NMP and the ionic liquid [hmim][TCB] as solvents. Separation and Purification Technology. 2016;**166**:196-204. DOI: 10.1016/j.seppur.2016.04.041

[39] Kister H. Distillation Design. New York: McGraw-Hill Education; 1992. ISBN: 9780070349094

[40] Lockett MJ. Distillation Tray Fundamentals. New York: Cambridge University Press; 1986. ISBN: 9780521321068

[41] AIChE. Bubble-Tray Design Manual: Prediction of Fractional Efficiency. New York: American Institute of Chemical Engineers; 1958

[42] Wilke CR, Chang P. Correlation of diffusion coefficients in dilute solutions. AICHE Journal. 1955;**1**:264-270. DOI: 10.1002/aic.690010222

[43] Rocha JA, Bravo JL, Fair JR. Distillation columns containing structured packings: A comprehensive model for their performance. 2. Mass-transfer model. Industrial and Engineering Chemistry Research. 1996;**35**:1660-1667. DOI: 10.1021/ie940406i

[44] Quijada-Maldonado E, Aelmans TAM, Meindersma GW, de Haan AB. Pilot plant validation of a rate-based extractive distillation model for water-ethanol separation with the ionic liquid [emim][DCA] as solvent. Chemical Engineering Journal. 2013;**223**:287-297. DOI: 10.1016/j.cej.2013.02.111

[45] Uerdingen M, Treber C, Balser M, Schmitt G, Werner C. Corrosion behaviour of ionic liquids. Green Chemistry. 2005;**7**:321-325. DOI: 10.1039/B419320M

[46] Dong K, Wang Q, Lu X, Zhou Q, Zhang S. Structure, interaction and hydrogen bond. In: Zhang S, Wang J, Lu X, Zhou Q, editors. Structures and Interactions of Ionic Liquids. Berlin, Heidelberg: Springer; 2014. pp. 1-38. DOI: 10.1007/978-3-642-38619-0_1

Thermal Management

Chapter 7

Effectiveness of a Helix Tube to Water Cool a Battery Module

Desmond Adair, Kairat Ismailov and
Zhumabay Bakenov

Additional information is available at the end of the chapter

http://dx.doi.org/10.5772/intechopen.74113

Abstract

This chapter presents an investigation of the effectiveness of water cooling a battery module using a heat-sink prototype in the form of a thin copper helix tube within an aluminium block. A thermal model for the module containing six single cells is developed and numerically solved by coupling the heat energy transport equation with the fluid governing equations. The rate of generation of heat from the cells is calculated using a 2D model of a single cell with the resulting heat flux used as a Neumann boundary condition for the energy equation within a computational fluid dynamics code. Particular attention is given to the battery module operating in extreme ambient temperature conditions. The cooling strategy used is shown to satisfy two of the main concerns when managing the thermal performance of a battery module, that is, a suitable operating temperature range is maintained, and there is reasonable uniformity of temperature across the battery module. This should increase the battery cell life cycle together with enhancement of the charge and discharge performances. Variation of parameters such as the velocity of water within the tube and the number of turns used for the helix were investigated.

Keywords: Li-ion battery, convective heat transfer, clean energy

1. Introduction

Due to their outstanding properties regarding high energy density, power density, high service life, low self-discharge and rare pollution, the use of lithium ion batteries for battery electric vehicles (BEVs) and hybrid electric vehicles (HEVs) shows excellent promise [1]. Battery charging and discharging are strongly coupled to the operating temperature with a higher temperature increasing the number of undesired reactions, that is, the decomposition of the

electrolyte, thickening of the solid electrolyte interface (SEI) film, and so on, which have the effect of degrading the battery capacity [2–4]. Lithium-ion battery cells are also highly sensitive to low temperatures. For example, at below $-10°C$, it has been shown that batteries' performance deteriorates considerably [5, 6]. Safety is also an issue in that at high temperatures, lithium-ion batteries are prone to uncontrollable temperature build-up (thermal runaway) [7]. In addition, a battery pack is usually composed of up to hundreds of single cells connected in series and/or in parallel to produce output voltage and power/energy capacity to achieve the BEVs' or HEVs' operating needs. This contributes to the accumulation of heat and uneven temperature distributions across the battery pack so degrading performance. To counteract these serious problems, it is necessary to cool a battery pack effectively and uniformly.

Important to the development of a realistic thermal model of a battery module is good knowledge of heat generation either from the battery module as a whole or from individual cells within the module. The battery heat generation rate can be estimated by direct measurement [8], by indirect measurement, for example by measuring equilibrium voltage [9], measuring internal electrical resistance [10] or using the electrochemical mechanism [11, 12]. For direct measurement, the results apply to only a few operating points, and for indirect measurements, accuracy is a problem as the heat generation rate is a nonlinear function of the state of charge (SOC), current and operating temperature [13]. Work on single cell thermal-electrochemical modelling has already been done [13–16], and it is the view here that an essential component for the modelling of battery modules and eventually battery packs is to start with accurate calculations of heat generation within a given single cell.

There are a number of ways of cooling battery modules with the major division being between air cooling and liquid cooling. There are advantages and disadvantages associated with each choice. For liquid cooling systems, a disadvantage is that they have the potential to leak, which could cause an electrical short. Also when liquid is used, maintenance and repair can be more costly and more complicated, and generally liquid cooled systems are more heavy and require more components. However, a design can be used, as in the present application where the battery module and liquid can be separated by aluminium. Air cooling systems are generally less effective at maintaining a uniform temperature within and between cells in a battery module, and they cannot carry as much heat away from the battery as quickly as a liquid-based system. Air convection (natural or forced) quite often is insufficient for effective heat dissipation from batteries under abuse conditions leading often to nonuniform temperature distributions within battery packs [17, 18]. Although air cooling systems are lighter, have a lower cost and generally a longer life, water cooling is favoured for this work due to its much superior cooling effect. There are many investigations of cooling systems reported in the literature with the majority of the work focusing on lumped parameter models [19]. The effectiveness of passive air cooling using phase change materials (PCMs) combined with forced cooling has been investigated [17], as has different single cell spacing arrangements [11, 20, 21]. It has been stated and demonstrated in the literature that indirect liquid cooling of battery packs (both passive and active) can prove an efficient method for dissipation or addition of heat [22–25].

This chapter presents an investigation of the thermal performance of indirect water cooling, using the proposed design prototype of a thin copper helix tube contained within an aluminium

http://dx.doi.org/10.5772/intechopen.74113

block, for a lithium ion battery module. A thermal model is developed for the battery module where electrochemical equations are solved to provide boundary conditions for a computational fluid dynamics code in which the energy and fluid flow conservation equations are solved. Variation of parameters such as the velocity of water within the tube and the number of turns used for the helix were investigated.

2. Mathematical model

2.1. Modelling within a single cell

The mathematical model for a single lithium-ion battery developed here is based on the work of Doyle et al. [26]. The battery cells used are cylindrical with a central mandrel, with thin layers of anode, cathode, current collector and separator rolling up on the mandrel and with protection provided by a battery can. The anode is made of graphite derivatives and the cathode material is a metallic oxide such as $LiFePO_4$ and LiM_2O_4. A schematic of a lithium ion cell is shown in **Figure 1**.

Generally, a lithium ion battery consists of the current collector, the positive electrode, the separator and the negative electrode. A lithiated organic solution fills the porous components and serves as the electrolyte. Several assumptions are needed, that is, the active electrode material is composed of spherical particles with uniform radius and the winding zone of the battery is a lumped model with homogeneous electrochemical properties. The material balance for the Li ions in an active solid material particle is governed by Fick's second law, here expressed in spherical coordinates

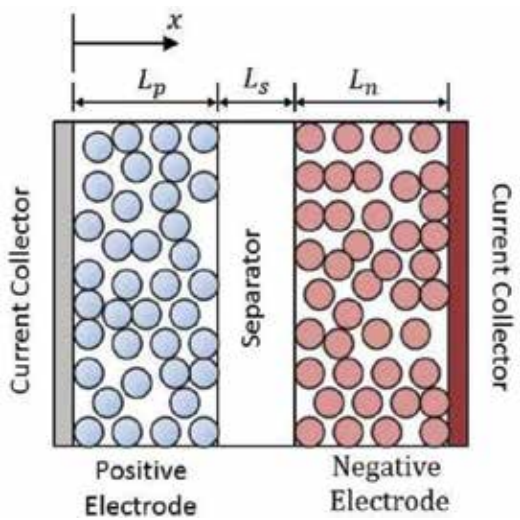

Figure 1. Schematic of a lithium ion battery.

$$\frac{\partial c_{s,i}}{\partial t} = D_{s,i}\frac{1}{r^2}\frac{\partial}{\partial r}\left(r^2\frac{\partial c_{s,i}}{\partial r}\right), \tag{1}$$

where $i = p, s$ and $i = n$ for the positive and negative electrodes, respectively. At the centre of the particle, there is no flux, and on the surface of the particle, the flux is equal to the consuming/producing rate of Li ions due to the chemical reaction occurring at the solid/liquid surface giving the boundary conditions

$$-D_{s,i}\frac{\partial c_{s,i}}{\partial r}\bigg|_{r=0} = 0, \quad -D_{s,i}\frac{\partial c_{s,i}}{\partial r}\bigg|_{r=r_s} = J, \tag{2}$$

where J is the flux of lithium ions away from the surface of the spherical particles. The mass conservation of Li in the electrode solution is given by the concentration solution theory and can be expressed as

$$\varepsilon'_i\frac{\partial c_i}{\partial t} = D_{eff,i}\frac{\partial^2 c_i}{\partial x^2} + \left(1 - t_+^0\right)a_i J_i, \tag{3}$$

where $i = p, s$ and n and a_i are the electrode surface area per unit volume of the electrode. In the separator, the pore wall flux J_s is equal to zero, and at the two ends of the cell in the x-direction, there is no mass flux

$$-D_{eff,p}\frac{\partial c_p}{\partial x}\bigg|_{x=0} = 0, \quad -D_{eff,n}\frac{\partial c_n}{\partial x}\bigg|_{x=L_p+L_s+L_n} = 0 \tag{4}$$

At the interfaces between the positive electrode/separator and separator/negative electrode, the concentration of the binary electrolyte and its flux is continuous

$$c_p\big|_{x=L_p^-} = c_s\big|_{x=L_p^+}, \qquad c_s\big|_{x=\left(L_p+L_s\right)^-} = c_n\big|_{x=\left(L_p+L_s\right)^+}, \tag{5}$$

$$-D_{eff,p}\frac{\partial c_p}{\partial x}\bigg|_{x=L_p^-} = -D_{eff,s}\frac{\partial c_s}{\partial x}\bigg|_{x=L_p^+} \tag{6}$$

$$-D_{eff,s}\frac{\partial c_s}{\partial x}\bigg|_{x=L_p^-} = -D_{eff,n}\frac{\partial c_n}{\partial x}\bigg|_{x=\left(L_p+L_s\right)^+} \tag{7}$$

The effective diffusion coefficient, D_{eff} of Li in the electrode can be represented as $D_{eff,i} = D_{\epsilon,i}\varepsilon_i^{brugg_i}$. The specific surface area for the electrode particles, a, is given by $a = 3\varepsilon_s/r_s$.

The charge balance in the solid phase is governed by Ohm's law

$$\sigma_{eff,i}\frac{\partial^2\phi_{s,i}}{\partial x^2} = a_i F J_i \tag{8}$$

where $i = p$ and n. Here σ_{eff} is the effective electric conductivity and is given by $\sigma_{eff} = \sigma\cdot\varepsilon_s$.

The boundary conditions are expressed as

$$-\sigma_{eff,p}\frac{\partial\phi_{s,p}}{\partial x}\bigg|_{x=0} = I_{app}, \quad -\sigma_{eff,p}\frac{\partial\phi_{s,p}}{\partial x}\bigg|_{x=L_p} = 0, \quad -\sigma_{eff,n}\frac{\partial\phi_{s,n}}{\partial x}\bigg|_{x=L_p+L_s} = 0 \tag{9}$$

The potential of the solid phase at the right end of the cell (**Figure 1**) is set to zero, $\phi_{s,n}\Big|_{x=L_p+L_s+L_n} = 0$ and the potential of the solid phase at $x = 0, \phi_{1,p}\Big|_{x=0}$ is equal to E_{cell}. The charge balance in the liquid phase is based on Ohm's law, and it is given by

$$-\frac{\partial}{\partial x}\left(\kappa_{eff,i}\frac{\partial\phi_{2,i}}{\partial x}\right) + \frac{2RT(1-t^+)}{F_d}\frac{\partial}{\partial x}\left(\kappa_{eff,i}\frac{\partial(\ln c_i)}{\partial x}\right) = \frac{F_d}{F_i}J_i \tag{10}$$

where $i = p, s$ and n, and, the specific conductivity of the electrolyte is a function of the concentration of the electrolyte in the liquid phase [27]

$$\kappa_{eff,i} = \kappa_i\varepsilon_i^{brugg_i} \tag{11}$$

At the two ends of the cell, there is no charge flux in the liquid phase

$$-\kappa_{eff,p}\frac{\partial\phi_{2,p}}{\partial x}\bigg|_{x=0} = 0, \quad -\kappa_{eff,n}\frac{\partial\phi_{2,n}}{\partial x}\bigg|_{x=L_p+L_s+L_n} = 0 \tag{12}$$

In the abovementioned equations, the pore wall flux, J_i is determined by the Butler-Volmer equation

$$J_i = k_i\left(c_{s,i,maz} - c_s|_{r=r_s}\right)^{\alpha_a}\cdot c_s|_{r=r_s}^{\alpha_c}\cdot c^{\alpha_a}\left\{\exp\left(\frac{\alpha_a F\eta_i}{RT}\right) - \exp\left(-\frac{\alpha_c F\eta_i}{RT}\right)\right\} \tag{13}$$

where η_i is the over-potential of battery electrodes and is given by

$$\eta_i = \phi_{s,i} - \phi_{2,i} - U_i \tag{14}$$

The open circuit voltage of the electrode materials U_i is determined by cell temperature and Li concentrations at the surface of the spherical particle. The energy balance is given by [15]

$$\rho C_p\frac{\partial T}{\partial t} = \nabla\cdot\nabla(k_T T) + Q_{rea} + Q_{rev} + Q_{ohm} \tag{15}$$

with the boundary conditions determined by Newton's cooling law

$$-\lambda\frac{\partial T}{\partial x}\bigg|_{x=0} = h(T_\infty - T), \quad -\lambda\frac{\partial T}{\partial x}\bigg|_{x=L_p+L_s+L_n} = h(T - T_\infty) \tag{16}$$

where h is the heat transfer coefficient, T_∞ is the ambient temperature, $\dot{Q}_{rea}$ is the total reaction heat generation rate, $\dot{Q}_{rev}$ is the total reversible heat generation rate, $\dot{Q}_{ohm}$ is the total ohmic heat generation rate. The heat fluxes are defined by

$$\dot{Q}_{rea} = aFJ_i\eta_i \tag{17}$$

$$\dot{Q}_{rev} = aFJ_iT\cdot\frac{dU_i}{dT} \tag{18}$$

$$\dot{Q}_{ohm} = \sigma_{eff}\left(\frac{\partial\phi_s}{\partial x}\right)^2 + \kappa_{eff}\left(\frac{\partial\phi_2}{\partial x}\right)^2 + \frac{2k_{eff}RT\left(1-t_+^0\right)}{F}\left(1+\frac{d\ln f_{\pm}}{d\ln c}\right)\frac{\partial\ln c}{\partial x}\frac{\partial\phi_2}{\partial x} + aFJ_i\Delta\phi_{SEI} \tag{19}$$

2.2. Modelling within the aluminium block

The battery module cooling system used here is a heat sink approach, where the lithium-ion battery cells are placed in an aluminium block and also surrounded by a copper helix coil through which water is pumped. The method employed is fundamentally to surround the cells with a conducting material, that is, a form of heat sink, and to remove or add heat using fluid. The cooling design is shown in **Figure 2**. The model solves in 3D, with fluid pumped through a central vertical tube and returned through the copper helix tube just within the aluminium block for efficient heat transfer and protection against damage.

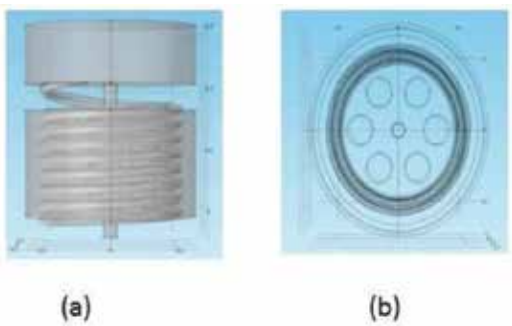

Figure 2. Copper helix coil within the aluminium block a. front and b. plan.

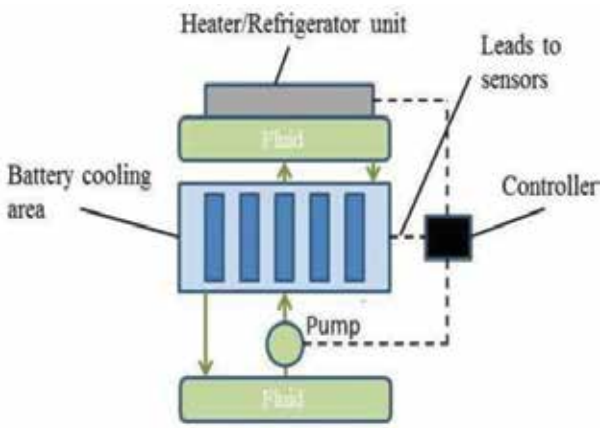

Figure 3. Schematic of thermal management system.

The fluid is conditioned using a heater/refrigerator unit placed on the top surface of the plenum chamber as shown in **Figure 3**. The aim of the overall thermal management system is to maintain a battery module at an optimum average temperature, as dictated by life and performance trade-off. Important is that an even temperature, perhaps with small variations, is maintained between the cells and within the module. However, when designing such a system, regard must also be paid to the fact that the battery module should be compact, lightweight, have low cost manufacture and maintenance, and have easy access for maintenance. The management system should also have low parasitic power, allow the module to operate under a wide range of climatic conditions and provide ventilation if the battery generates potentially hazardous gases.

The calculation domain has two subdomains, that is, a fluid region and a solid region.

2.2.1. Fluid section

For non-steady flow, the equations of continuity, momentum and energy can be expressed in the general conservation form

$$\frac{\partial}{\partial t}(\rho\varphi) + \frac{\partial}{\partial x_i}(\rho u_i \varphi) = \frac{\partial}{\partial x_i}\left(\Gamma_\varphi \frac{\partial \varphi}{\partial x_i}\right) + S_\varphi \tag{20}$$

where ρ is the liquid density, u_i is the velocity vector components, Γ_φ is the effective exchange coefficient of φ and S_φ is the source rate per unit volume. The source rate and the effective exchange coefficient corresponding to each variable φ solved in this study are given in **Table 1**. Included in **Table 1** are the transport equations for the standard k-ε turbulence model.

In **Table 1**, μ is the viscosity, σ is the Prandtl number for ε and $G_k = \mu\left(\partial u_i/\partial x_j + \partial u_j/\partial x_i\right)\left(\partial u_i/\partial x_j\right)$ the turbulence production rate. The values of the constants C_1 and C_2 are 1.44 and 1.92 respectively and for σ_k and σ_ε, 1.0 and 1.3 respectively [28]. The eddy viscosity term is

$$\mu_t = \rho C_\mu \frac{k^2}{\varepsilon} \tag{21}$$

where $C_\mu = 0.09$.

Equation	φ	S_φ	Γ_φ
Continuity	1	0	0
Momentum	U_i	$\frac{\partial p}{\partial x_i} + \rho_{ref} g_i$	$\rho(\mu + \mu_t)$
Enthalpy	h	$\frac{Dp}{Dt}$ + heat sources (sinks)	$\rho\left(\frac{\mu_t}{\sigma_t} + \frac{\mu}{Pr}\right)$
Kinetic energy of turbulence	k	$G_k - \rho\varepsilon$	$\frac{\mu}{\sigma_k}$
Eddy dissipation rate	ε	$C_1\left(\frac{\varepsilon}{k}\right)G - C_2\rho\left(\frac{\varepsilon^2}{k}\right)$	$\frac{\mu}{\sigma_\varepsilon}$

Table 1. Source rate and effective exchange coefficient for each φ.

In addition to the standard k-ε turbulence model, the realisable k-ε model with standard wall functions, and, non-equilibrium wall functions for the near-wall treatments were used to model turbulent flow as they show good performance in modelling flow structures [29, 30]. Although low-Reynolds number modelling (LRNM) may give more accurate simulation results, this requires very fine cells close to the wall to resolve the near wall region, which increases the difficulties of grid generation and computing time cost. Also the grid used by LRNM is unsuitable for the high-Reynolds number turbulence models used here because the very fine cells close to the wall cannot satisfy the first node near the wall located out of the viscous sub-layer [31]. The equations for the realisable k-ε turbulence model are

$$\frac{\partial}{\partial t}(\rho k) + \frac{\partial}{\partial x_j}(\rho k u_j) = \frac{\partial}{\partial x_j}\left(\left(\mu + \frac{\mu_t}{\sigma_k}\right)\frac{\partial k}{\partial x_j}\right) + G_k - \rho\varepsilon \tag{22}$$

$$\frac{\partial}{\partial t}(\rho \varepsilon) + \frac{\partial}{\partial x_j}(\rho \varepsilon u_j) = \frac{\partial}{\partial x_j}\left(\left(\mu + \frac{\mu_t}{\sigma_\varepsilon}\right)\frac{\partial \varepsilon}{\partial x_j}\right) + C_1 \rho S_\varepsilon - C_2 \rho \frac{\varepsilon^2}{k + \sqrt{\mu\varepsilon}} \tag{23}$$

$$\mu_t = \rho C_\mu \frac{k^2}{\varepsilon} = \frac{1}{4.04 + A_s k u^*/\varepsilon} \tag{24}$$

$$u^* = \sqrt{S_{ij}S_{ij}\tilde{\Omega}_{ij}\tilde{\Omega}_{ij}}, \quad \tilde{\Omega}_{ij} = \Omega_{ij} - 2\varepsilon_{ijk}\omega_k \tag{25}$$

$$A_s = \sqrt{6}\cos\varphi', \quad \varphi' = \frac{1}{3}\cos^{-1}\left(\sqrt{6}W\right), \quad W = \frac{S_{ij}S_{ik}S_{jk}}{\tilde{S}^3} \tag{26}$$

$$\tilde{S} = \sqrt{S_{ij}S_{ij}}, \quad C_1 = \max\left[0.43, \frac{\tilde{\mu}}{\tilde{\mu} + 5}\right] \tag{27}$$

where $\sigma_k = 1.0$, $\sigma_\varepsilon = 1.2$ and $C_2 = 1.9$. The standard wall functions used here are based on the work of Launder and Spalding [32] and have been found to be suitable for a broad range of wall-boundary flows. The law-of-the-wall for mean velocity gives

$$U^* = \begin{cases} y^* & (y^* > 11.225 \\ \dfrac{1}{\kappa}\ln(Ey^*) & (y^* < 11.225 \end{cases} \tag{28}$$

where

$$U^* = \frac{U_p C_\mu k_p^{1/2}}{\tau_w/\rho} \tag{29}$$

is the dimensionless velocity, and

$$y^* = \frac{\rho C_\mu^{1/4} k_p^{1/2} y_p}{\mu} \tag{30}$$

is the dimensionless distance from the wall and κ is the von Karman constant (=0.4187), E is the empirical constant (=0.9793), U_p is the mean velocity of the fluid at the near-wall node P, k_p is

the turbulence kinetic energy at the near-wall node P, y_p is the distance from the point P to the wall, and μ is the dynamic viscosity of the fluid. The temperature wall functions include the contribution from the viscous heating, and for incompressible flow calculations, the law-of-the-wall for the temperature field has the following composite form

$$T^* = \frac{(T_w - T_p)\left(C_\mu^{1/4} k_p^{1/2}\right)}{(q_w/\rho C_p)} = \begin{cases} Pry^* & (y^* < y_T^* \\ Pr_t\left[\frac{1}{\kappa}\ln(Ey^*) + P\right] & (y^* > y_T^* \end{cases} \tag{31}$$

where P is given by Jayatilleke [33]

$$P = 9.24\left(\frac{Pr}{Pr_t} - 1\right)\left(\frac{Pr}{Pr_t}\right)^{-1/4} \tag{32}$$

where y_T^* is the dimensionless thermal sublayer thickness, C_p is the specific heat of the fluid, q_w the wall heat flux, T_p is the temperature at the first near-wall node P, T_w is the temperature of the wall, Pr is the molecular Prandtl number ($= \mu C_p/a'$), a' is the coefficient of heat diffusion, and Pr_t is the turbulent Prandtl number (-0.85 at the wall).

The standard wall functions tend to become less reliable when the flow situations depart from the ideal conditions and are subjected to severe pressure gradients and strong non-equilibrium. The non-equilibrium wall functions are introduced and can potentially improve the results in the above mentioned situations [34]. The law-of-the wall for mean temperature remains the same as in the standard wall functions already described and the log-law for mean velocity sensitised to the pressure gradient is

$$\frac{\tilde{U}C_\mu^{1/4}k^{1/2}}{\tau_w/\rho} = \frac{1}{\kappa}\left(E\frac{\rho C_\mu^{1/4}k^{1/2}y}{\mu}\right) \tag{33}$$

where

$$\tilde{U} = U - \frac{1}{2}\frac{dp}{dx}\left[\frac{y_v}{\rho\kappa\sqrt{k}}\ln\left(\frac{y}{y_v}\right) + \frac{y - y_v}{\rho\kappa\sqrt{k}} + \frac{y_v^2}{\mu}\right] \tag{34}$$

and y_v is the physical viscous sublayer thickness, and computed from

$$y_v = \frac{\mu y_v^*}{\rho C_\mu^{1/4} k_p^{1/2}} \tag{35}$$

where $y_v^* = 11.225$.

In this study, the Boussinesq model was used to treat the variable water density in which the water density is taken as a constant in all terms of the solved equations, except for the buoyancy term in the momentum equation

$$(\rho - \rho_0)g = -\rho_0\beta(T - T_0)g \tag{36}$$

where ρ_0 is the reference density of the water flow (kg/m^3); T_0 is the reference temperature (K); and, Eq. (37) is obtained by the Boussinesq approximation $\rho = \rho_0(1 - \beta\Delta T)$ to replace the buoyancy terms. This approximation is acceptable so long as changes in actual density are small. Specifically, it is valid when $\beta(T - T_0) \ll 1$, and should not be used if the temperature difference in the domain is large.

2.2.2. Solid section

The solid section in this work consists of three components, namely, the aluminium block, the wall of the helix coil and the battery module. When the velocity is set to zero in Eq. (20), the equation governing pure conductive heat transfer by diffusion is obtained, that is,

$$\frac{\partial}{\partial t}(\rho\varphi) = \frac{\partial}{\partial x_i}\left(\Gamma_\varphi \frac{\partial \varphi}{\partial x_i}\right) + S_\varphi \tag{37}$$

Conjugate heat transfer was used between the solid domain and fluid domain.

2.3. Boundary conditions and settings

The cooling fluid is modelled using the material properties of water calculated using the inlet temperature. The settings and boundary conditions are set out in **Tables 2** and **3**.

2.4. Grid dependence and computer storage

The requirements set out in two recent guidelines referring to good CFD practice [35, 36] were followed in the present work. Non-uniform structured Cartesian grids were used throughout this work with extensive tests for independence of grid size checked by increasing the grid numbers until further refinement was shown not to be of significance. Close to solid surfaces, the grid was refined using geometric progression with an expansion ratio from the solid surfaces of less than 1.1 and with the Y^+ values adjacent to a solid boundary held around a

Battery module outside dimensions	Radius = 130 mm, height = 360 mm
Cooling pipe radius (r_{inner})	5–15 mm
Coolant	H_2O
Final mesh size	10^7

Table 2. Various settings used during the calculations.

Cylinder outer wall	293.15 K
Coolant/solid interface	Conjugate heat transfer
Cooling pipe inlet	$u_{in} = 0.005 - 0.1$ m/s
Cooling pipe outlet	$T_{in} = 293.15$ K
Cell initial temperatures	101,325 Pa
	$T_{init} = 313.15$ K
	$T_{init} = 349.15$ K

Table 3. Boundary conditions used during the calculations.

value of 20, so complying with recommendations given in the literature that Y^+ should be between 11.5 and 300 to ensure accuracy when using a high-Reynolds turbulence model [37]. Tests for grid independent solutions were carried out using 2.0×10^5, 2.0×10^6 and 1.0×10^7. The overall change in the residual for each variable between the last two numbers of elements was less than 0.1%, indicating grid independence had been achieved. The calculations were performed on a Dell T5500 workstation with 32 nm six-core Intel Xeon 5600 series processor and main memory of 24 GB. A typical CPU time for a transient run with a grid having 10^6 nodes was just over 24 h.

3. Results

3.1. Heat generation within a single cell

The thermal characteristics of a Li-ion battery cell are first investigated using Eqs. (1)–(19), which form thermal-electrochemical coupled model. The cell used in these calculations has an electrolyte consisting of zinc and lithium salts dissolved in water. When the battery is fully charged, the anode consists of nonporous zinc and the cathode of porous Mn_2O_4. It is important to note that some of the electrochemical calculations are strongly dependent on coefficients, which are in turn strongly dependent of experimental results. For example, for the electrolyte just described, the specific conductivity Eq. (11) of the electrolyte is a function of temperature and the concentration of the electrolyte in the liquid phase, and so the ionic conductivity, κ_i had to be determined by experiment, the results of which are summarised in **Figure 4**.

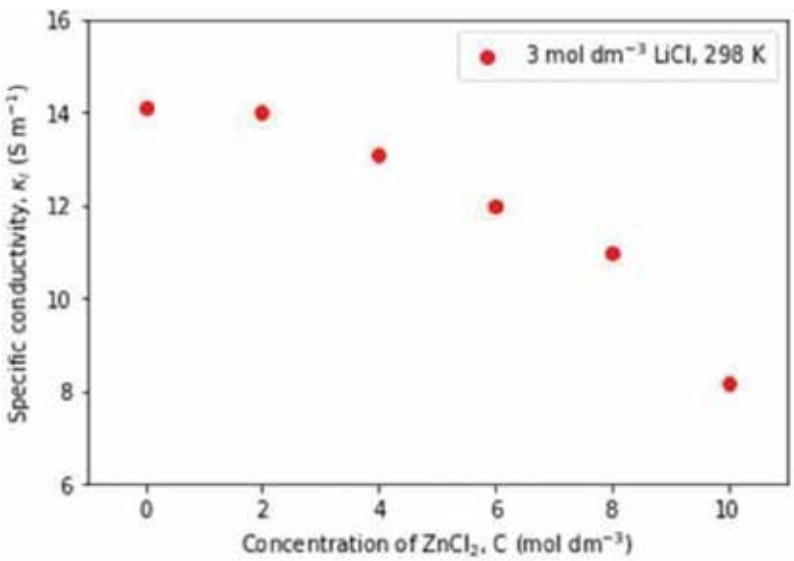

Figure 4. Ionic conductivity of electrolyte consisting of a $ZnCl_2$ and LiCl aqueous solution.

The effect of using different current rates during discharge of the battery cell is illustrated in **Figure 5**. Here temperature on the cell surface is calculated against the depth of discharge (DOD), which indicates the state of discharge of the battery cell starting at 100% fully charged. In these calculations, DOD was calculated as time $*\frac{\text{C rate}}{3600}$ and the heat transfer coefficient h was set at 1.0 $Wm^{-2}\,K^{-1}$. As would be expected, the cell surface gets hotter as the discharge current rate increases. There is a 'kink' in the curve at lower current rates, which is thought to be due to an interaction between the ohmic and reversible heat in the energy balance equation.

Also calculated were the profiles of cell surface temperatures over a long time of discharge. Two limiting cases, that is, adiabatic and isothermal were used as the boundaries for this study with different heat transfer coefficients used for the intervening calculations, as shown in **Figure 6**. It can be seen that the heat transfer coefficient 1.0 $W^{-2}\,K^{-1}$ gives a reasonable result and keeps the battery cell well within the desired operating range, while the 0.1 $W^{-2}\,K^{-1}$ setting allows the battery cell wall temperature to reach the upper region of the desired range.

3.2. Cooling the battery module

In this part of the study, the temperature history of the battery module was modelled with ambient conditions (T_∞) set at 293.15 K, and each of the cells sets initially at T_{init}=313.15 K and then at T_{init}=349.15 K. This part of the calculations is important to the design process in that, in addition to testing, if the chosen geometry parameters are suitable, it also gives an indication concerning the selection of a suitable pump and heater/refrigeration unit. Typical velocity contours for the liquid coolant are shown in **Figure 7**. The important part here is that heat can be removed from the coolant in the plenum chamber efficiently. From **Figure 7**, it can be seen that there is slow moving water adjacent to the heating/refrigeration unit, and hence there is sufficient time for dissipation of heat.

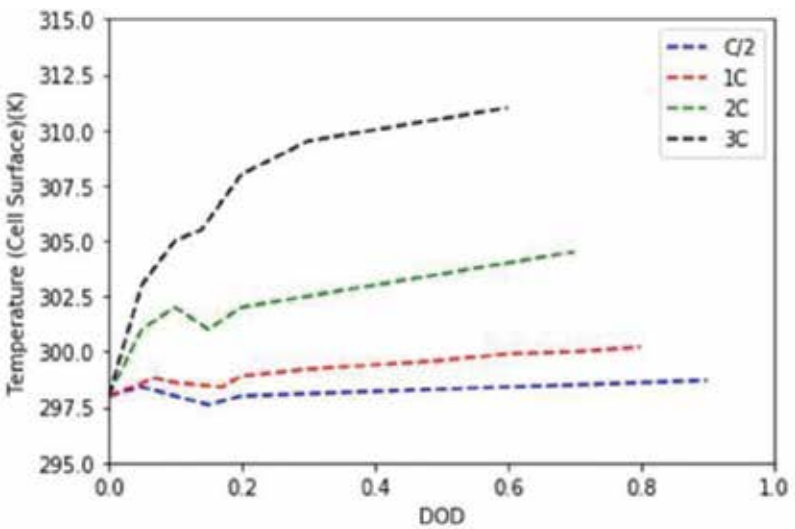

Figure 5. Cell surface temperature during discharge at different current rates.

http://dx.doi.org/10.5772/intechopen.74113

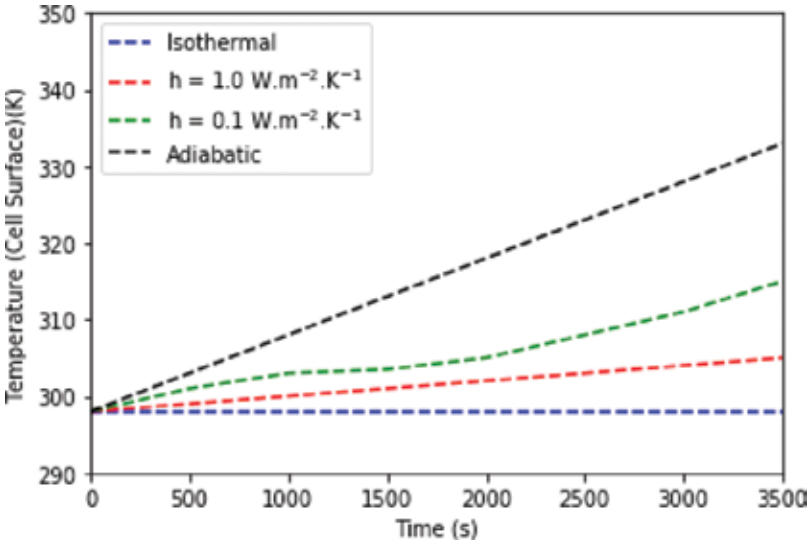

Figure 6. Cell surface temperature for different cooling conditions.

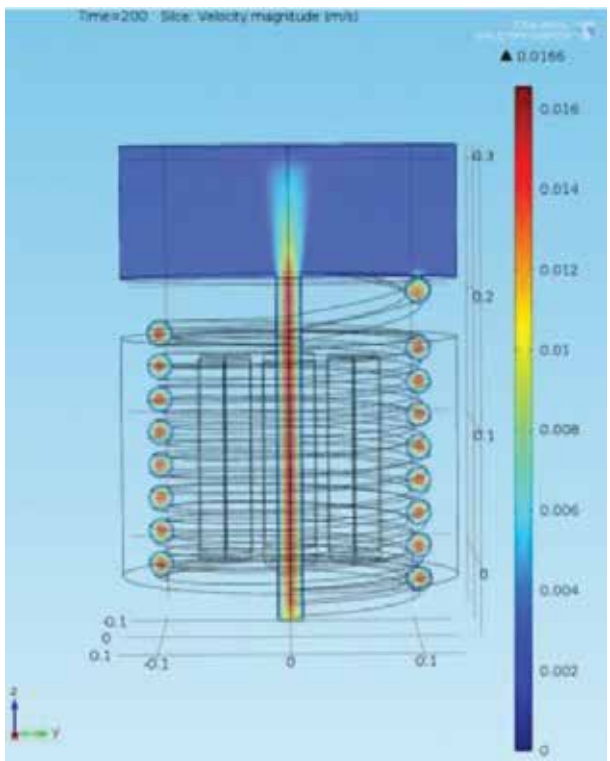

Figure 7. Velocity contours, $u_{in} = 0.01$ m/s, $T_{in} = 293.15$ K, $r_{inner} = 10$ mm, $T_{\infty} = 293.15$ K.

Several tests were conducted, where the battery module was cooled to find appropriate values for the parameters, u_{in} and the optimum number of helix coil turns. **Figure 8** shows temperature values obtained at the centre of a cell versus time during cooling. The figure shows results for two initial cell temperatures, that is, 313.15 and 349.15 K, and the temperature profiles were obtained for different inlet velocities to the helix tube ranging from 0.005 to 0.1 m/s. It was found that when using an inlet velocity of 0.005 m/s, the cell temperature did not reach an acceptable temperature over what was regarded as a reasonable time. When the inlet velocity was increased to 0.01 m/s, acceptable temperatures were calculated after 80 and 20 s for the higher and lower initial temperatures, respectively. With the much higher inlet velocity of coolant to the helix pipe, that is, 0.1 m/s, there was a definite faster reduction in temperature. However, this faster velocity has design implications in that more powerful pumps together with a greater danger of coolant leakage make use of this inlet velocity value less attractive. Therefore, it was decided to continue the study with $u_{in} = 0.01$ m/s. It is also noticeable from **Figure 8** that as the initial temperature of the cells was reduced, increasing the velocity of the coolant through the pipe had much less effect on the cooling rate. This could mean that, although the coolant at higher velocity had more capacity to carry heat energy away from the battery pack, the temperature gradient between solid helix pipe and water was no longer sufficient to drive heat energy from solid to liquid effectively. This could possibly be due to the complex nature of the flow within the helix tube. Inside the tube, the flow is stretched from the inner wall, where most of the heat energy enters the liquid towards the outer wall due to centrifugal forces. Secondary flow also results due to the centrifugal forces. This aspect of the design needs further research.

It is important to know the optimum number of turns the helix coil makes for a number of reasons. One is that if too many coils are used, then more expense occurs in the manufacturing

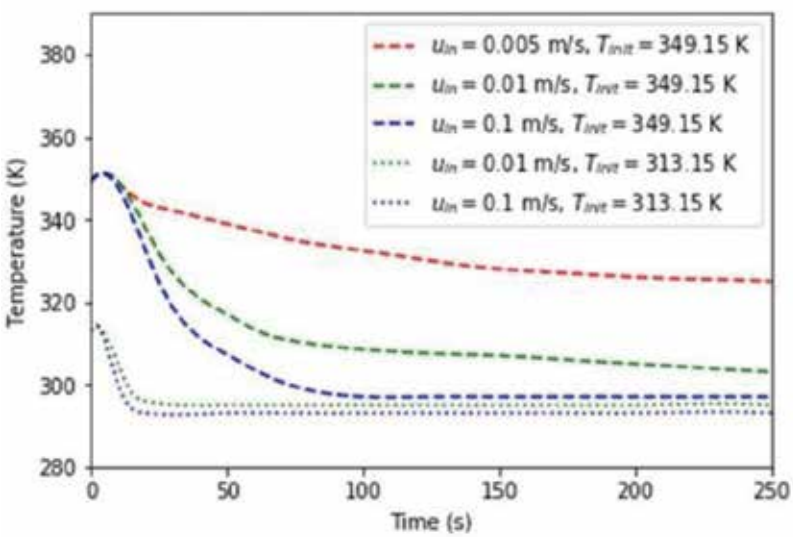

Figure 8. Temperature cooling profiles versus time at the centre of a cell for different initial cell temperatures and fluid velocities in the helix tube. Here $r_{inner} = 10$ mm, $T_{\infty} = 293.15$ K and $T_{in} = 293.15$ K.

stage and also the integrity of the structure may suffer. If the number of coils is too small, then cooling of the battery to its ideal operating temperature range may become unacceptable. As can be seen from **Figure 9**, there is a big advantage to the cooling system when increasing the number of turns for 5 to say 15, but after that, the cooling effect of increasing the number of turns is greatly diminished. Increasing the number of turns is equal to lengthening the heat transfer path. According to **Figure 9**, as the number of turns increases, the amount of the heat transfer coefficient decreases significantly and after, say, 15 turns, it remains almost constant. The Prandtl number for water is larger than the one which would make the thermal entrance greater than the hydraulic entrance length. This means that after about 15 turns the thermal entrance length has been passed. An optimum number of turns appear to be around 10. The rest of this study continues with the number of helix turns in the aluminium block to be 10.

It is important for the lengthening of battery cell life and the enhancement of charging and discharging performance that uniformity of temperature is achieved throughout each cell, in addition to uniformity of cell temperatures across the cells within the battery module. To confirm that uniformity of temperature could be achieved across a single cell lodged within the battery module, temperature profiles were calculated in the radial direction through the battery module. As can be seen from **Figure 10**, where the radius at 0 is the battery module centre and radius at 130 mm is the outer wall of the module, the temperature profiles gradually move from an initial profile distorted by the hot cell to an acceptable final uniform distribution after about 15 s.

Another series of tests were conducted on the battery module which had, in addition to initial temperatures of 313.15 and 349.15 K, an internal heat source for each cell of either 0.25, 0.5 or 1 W. Results for the module with each of the cells having internal heat sources of 1 W are

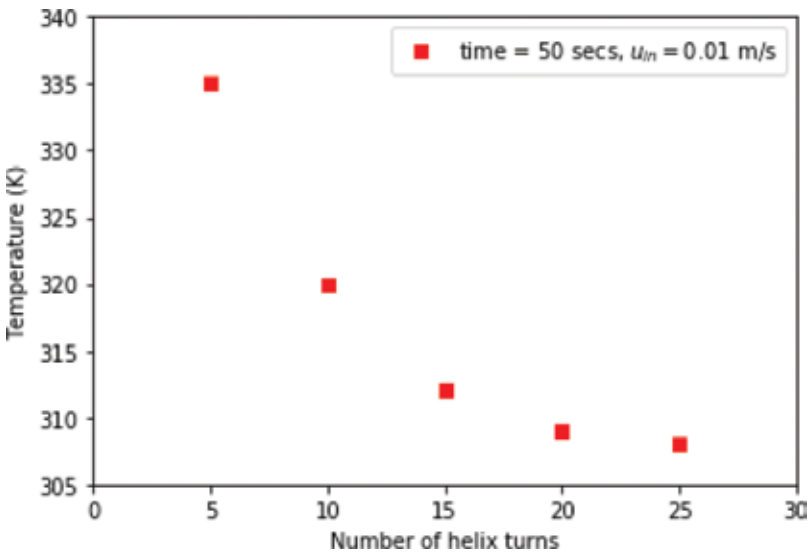

Figure 9. Temperature values at the centre of a cell for different number of helix coil turn after 50 s. Here, $T_{init} = 313.15$ K, $u_{in} = 0.01$ m/s, $r_{inner} = 10$ mm, $T_{\infty} = 293.15$ K, $T_{in} = 293.15$ K.

shown in **Figures 11** and **12**. As with the previous tests, what was important was the control of temperature between acceptable limits and a good uniformity of temperature across each cell.

It can be seen from **Figures 11** and **12** that in the early stages of cooling, non-uniformity was found, but after, say, 1 min, uniformity was acceptable throughout each cell, and after 2 min, each cell was within the desired operating temperature limits (Note: each sub-figure has its

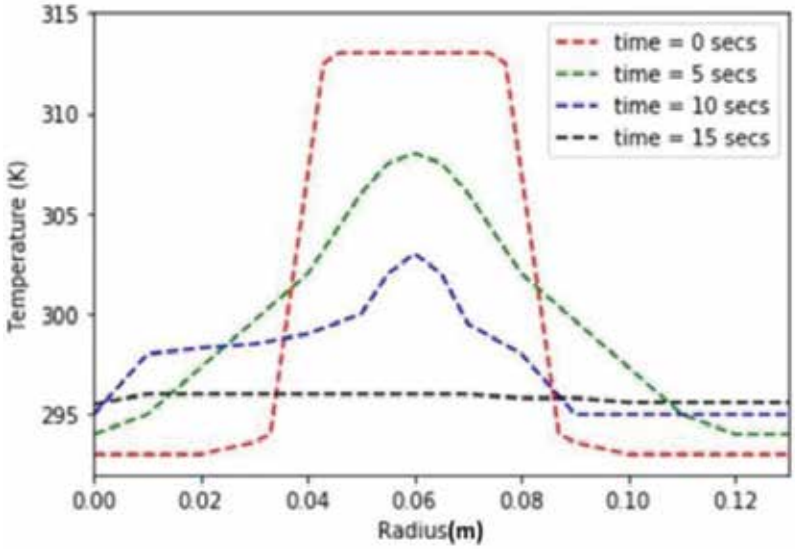

Figure 10. Temperature profiles in the radial direction for $T_{init} = 313.15$ K, $u_{in} = 0.01$ m/s, $r_{inner} = 10$ mm, $T_{\infty} = 293.15$ K, $T_{in} = 293.15$ K.

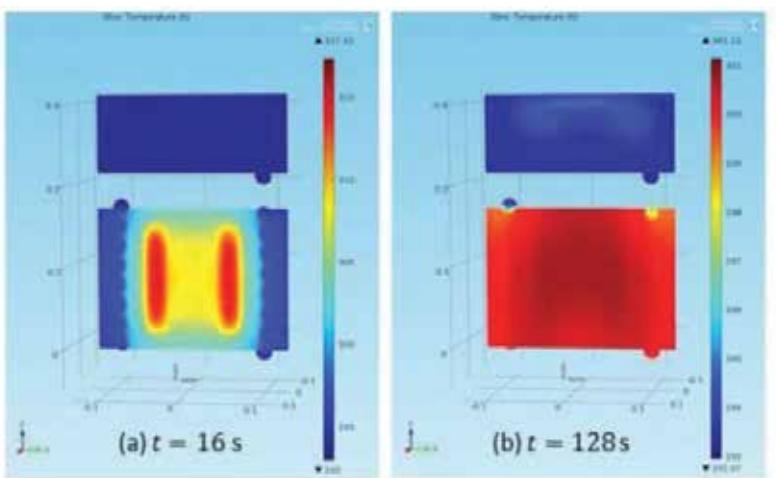

Figure 11. Front view of temperature profiles for T_{init} =313.15 K, $u_{in} = 0.01$m/s, $r_{inner} = 10$ mm, $T_{in} = 293.15$ K, and heat source within each cell of 1 W.

http://dx.doi.org/10.5772/intechopen.74113

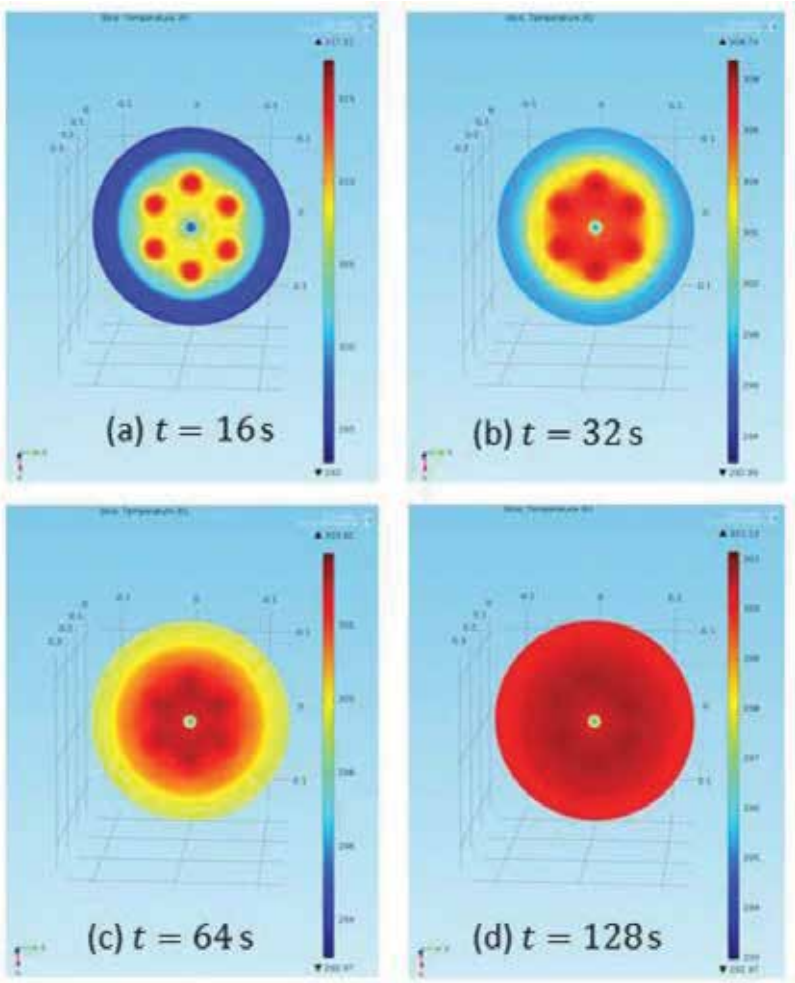

Figure 12. Plan view of temperature profiles for T_{init} =313.15 K, $u_{in} = 0.01$m/s, $r_{inner} = 10$ mm, $T_{in} = 293.15$ K, and heat source within each cell of 1 W.

own temperature scale). At times greater than 2 min, the heat loss to the atmosphere was slightly higher than heat production within the cells, even at 1 W, so reducing the need for further cooling. In the propose prototype, the temperature would be monitored using a thermostat, and further cooling would ensue intermittently as necessary.

4. Conclusion(s)

Preliminary results useful to the final design of a prototype battery module have been produced. The values found for the important parameters help in confirming the chosen geometry, and give indications of necessary pump and heating/refrigeration specifications needed when assembling

the prototype. The calculations were made first inside a given battery cell to indicate what sort of temperature differences may be expected. It was found that these calculations depended heavily on experimental work to find appropriate coefficients for the coupled equations. After getting the range of temperatures arising from single battery cell calculations, a method was developed to find the temperature characteristics of the battery module, with stress being put on uniformity of temperature both within an individual cell and across the complete battery module.

Conflict of interest

There is no conflict of interest associated with this chapter.

Nomenclature

a	specific surface area, m^{-2}
c	electrolyte concentration in the solution phase, mol^{-3}
c_s	Li concentration in electrode particles, mol m^{-3}
C_1, C_2	k -ε turbulence model constants
C_p	specific heat
C_μ	turbulence model coefficient
D_{eff}	effective diffusion coefficient of Li in the electrode
D_s	diffusion coefficient of Li in electrode particles, $m^2\ s^{-1}$
E	potential
F	Faraday's constant
h	heat transfer coefficient
I	current
J	surface reaction flux, mol $m^{-2}\ s^{-1}$
J_i	pore wall flux
k	turbulence kinetic energy
k_p	turbulence kinetic energy at near wall node
k_T	lumped thermal conductivity of cell
L_n	anode thickness, m
L_p	cathode thickness, m

L_s	separator thickness
Pr	Prandtl number
q_w	wall heat flux
$\dot{Q}_{rea}$	heat generation due to electrochemical reaction
$\dot{Q}_{rev}$	reversible heat
$\dot{Q}_{ohm}$	ohmic heat
r	radius/radial
R	universal gas constant
t	time
t_+^0	transference number
T	temperature
T_∞	ambient temperature
T_0	reference temperature
T_w	wall temperature
U	mean velocity
U_i	open circuit voltage
x_i	spatial coordinates
y_v	viscous sublayer thickness
y^+	dimensionless velocity

Greek letters

β	constant, Boussinesq model
ε	dissipation
ε'	volume fraction of electrolyte
η_i	overpotential
κ	von Karman constant
λ	coefficient, Newton's cooling law
μ	absolute viscosity
ρ	density

ρ_0 reference density

σ_{eff} effective electric conductivity

σ_k constant in turbulence model

σ_ε constant in turbulence model

τ_w wall shear stress

ϕ potential

Γ_φ effective exchange coefficient

Author details

Desmond Adair*, Kairat Ismailov and Zhumabay Bakenov

*Address all correspondence to: dadair@nu.edu.kz

Nazarbayev University, Astana, Kazakhstan

References

[1] Aifantis KE, Hackney SA, Kumar RV. High Energy Density Lithium Batteries: Materials, Engineering, Applications. New York: Wiley; 2010

[2] Ramadass P, Haran B, White R, Popov BN. Capacity fade of Sony 18650 cells cycled at elevated temperatures: Part I. Cycling performance. Journal of Power Sources. 2002; **112**(2):606-613

[3] Ramadass P, Haran B, White R, Popov BN. Capacity fade of Sony 18650 cells cycled at elevated temperatures: Part II. Capacity fade analysis. Journal of Power Sources. 2002; **112**(2):614-620

[4] Pinson MB, Bazant MZ. Theory of SEI formation in rechargeable batteries: Capacity fade, accelerated aging and lifetime prediction. Journal of the Electrochemical Society. 2013;**160**: A243-A250

[5] Zhang SS, Xu K, Jow TR. The low temperature performance of Li-ion batteries. Journal of Power Sources. 2003;**115**(1):137-140

[6] Fan J. On the discharge capability and its limiting factors of commercial 18650 Li-ion cell at low temperatures. Journal of Power Sources. 2003;**117**:170-178

[7] Wang Q, Ping P, Zhao X, Chu G, Sun J, Chen C. Thermal runaway caused fire and explosion of lithium ion battery. Journal of Power Sources. 2012;**208**:210-224

[8] Fan L, Khodadadi JM, Pesaraan AA. Parametric study on thermal management of an air-cooled lithium battery module for plug-in hybrid electric vehicles. Journal of Power Sources. 2013;**247**(3):961-966

[9] Ling Z, Wang F, Fang X, Gao X, Zhang Z. A hybrid thermal management system for lithium ion batteries combining phase change materials with forced-air cooling. Applied Energy. 2015;**148**:403-409

[10] Mahamud R, Park C. Reciprocating air flow for Li-ion battery thermal management to improve temperature uniformity. Journal of Power Sources. 2011;**196**(13):5685-5696

[11] Yang N, Zhang X, Li G, Hua D. Assessment of the forced air-cooling performance for cylindrical lithium-ion battery packs: A comparative analysis between aligned and staggered cell arrangements. Applied Thermal Engineering. 2015;**80**:55-65

[12] Amiribavandpour P, Shen W, Mu D, Kapoor A. An improved theoretical electrochemical-thermal modelling of lithium-ion battery packs in electric vehicles. Journal of Power Sources. 2015;**284**:328-338

[13] Ye Y, Shi Y, Cai N, Lee J, He X. Electro-thermal modeling and experimental validation for lithium-ion battery. Journal of Power Sources. 2012;**199**:227-238

[14] Cai L, White RE. Mathematical modelling of lithium ion battery with thermal effects in COMSOL Inc multiphysics software. Journal of Power Sources. 2011;**196**:5985-5989

[15] Gu WB, Wang CY. Thermal-electrochemical modeling of battery systems. Journal of the Electrochemical Society. 2000;**147**(8):2910-2922

[16] Anwar S, Zou C, Manzie C. Distributed thermal-electrochemical modeling of a lithium-ion battery to study the effect of high charging rates. The International Federation of Automatic Control; 24-29 August, 2014; Cape Town, South Africa

[17] Sabbah R, Kizilel R, Selman JR, Al-Hallaj S. Active (air-cooled) vs. passive (phase change material) thermal management of high power lithium-ion packs: Limitation of temperature rise and uniformity of temperature distribution. Journal of Power Sources. 2008; **182**(2):630-638

[18] Pesaran AA, Burch S, Keyser M. An approach for designing thermal management systems for electric and hybrid vehicle battery packs. Fourth Thermal Management Systems Conference and Exhibition; 24-27 May, 1999; London, UK

[19] Klien R, Chaturvedi NA, Christensen J, Ahmed J, Findeisen R, Kojic A. Electrochemical model based observer design for a lithium-ion battery. IEEE Transactions on Control Systems Technology. 2013;**21**(2):289-301

[20] Karimi G, Li X. Thermal management of lithium-ion batteries for electric vehicles. International Journal of Energy Research. 2013;**37**:13-24

[21] Ismailov K, Adair D, Massalin Y, Bakenov Z. On using splitter plates and flow guide-vanes for battery module cooling. Heat and Mass Transfer. 2017;**53**(1):1-10

[22] Chen K, Li X. Accurate determination of battery discharge characteristics - a comparison between two battery temperature control methods. Journal of Power Sources. 2014;**247**(3): 961-966

[23] Yeow K, Teng H, Thelliez M, Tan E. Thermal analysis of a Li-ion battery systems with indirect liquid cooling using finite element analysis approach. SAE International Journal of Alternative Power. 2012;**1**(1):65-78

[24] Tong W, Somasundaram K, Birgersson E, Mijumdar AS, Yap C. Numerical investigation of water cooling for a lithium-ion bipolar battery pack. International Journal of Thermal Science. 2015;**94**:259-269

[25] Pesaran AA. Battery thermal management in EVs and HEVs: Issues and solutions. Advanced Automotive Battery Conference; 6-8 Feb., 2001; Las Vegas, Nevada

[26] Doyle M, Fuller TF, Newman J. Modeling of galvanostatic charge and discharge of the lithium/polymer/insertion cell. Journal of the Electrochemical Society. 1993;**140**:1526-1533

[27] Valoen LO, Reimers N. Transport properties of LiPF6 - based li-ion battery electrolytes. JES. 2005;**152**:A882-A891

[28] Adair D. Numerical calculations of aerial dispersion from elevated sources. Applied Mathematical Modelling. 1990;**14**:459-467

[29] Allegrini J, Dorer V, Carmeliet J. Buoyant flows in street canyons: Validation of CFD simulations with wind tunnel measurements. Building and Environment. 2014;**72**:63-74

[30] van Hooff T, Blocken B. Coupled urban wind flow and indoor natural ventilation modelling on a high-resolution grid: A case study for the Amsterdam arena stadium. Environment Modelling and Software. 2010;**25**(1):51-65

[31] Tao WQ. Numerical Heat Transfer. 2nd ed. Xi'an: Xi'an Jiaotong University Press; 2001

[32] Launder BE, Spalding DB. The numerical computational of turbulent flows. Computer Methods in Applied Mechanics and Engineering. 1974;**3**(2):269-289

[33] Jayatillaka C. The influence of Prandtl number and surface roughness on the resistance of the laminar sublayer to momentum and heat transfer. Progress in Heat and Mass Transfer. 1969;**1**:193-321

[34] Kim SE, Choudhury D. A near-wall treatment using wall functions sensitized to pressure gradient. In F.E.D. ASME, editors, Symp. on Separated and Complex Flows. 1995;**217**:249-256

[35] Tominaga Y, Mochida A, Yoshie R, Kataoka H, Nozu T, et al. All guidelines for practical applications of CFD to pedestrian wind environment around buildings. Journal of Wind Engineering and Industrial Aerodynamics. 2008;**96**:1749-1761

[36] Meroney R, Ohba R, Leitl B, Kondo H, Grawe D, Tominaga Y. Review of CFD guidelines for dispersion modeling. Fluids. 2016;**1**(14):1-16

[37] Patankar SV. Numerical Heat Transfer and Fluid Flow. New York: CRC Press; 1980

Edited by Yong Ren

Heat and mass transfer are ubiquitous transport phenomena in many fields, from the natural environment and living organisms to the engineering process. This book focuses on the latest advances in applying fundamental heat and mass transfer theory and novel technologies for addressing a wide range of industrial problems of interest. This book will present readers with a recent analytical study, CFD modelling, and experimental investigations of heat and mass transfer topics associated with a variety of engineering disciplines including multiphase flow, nanofluids, porous media, battery thermal management, and engineering processes such as extractive distillation and arc welding. The book aims to provide new insights to understand the heat and mass transfer phenomena, serving as a platform for exchanging inspiring ideas and boosting further development of these disciplines.

ISSN 2631-6196
ISBN 978-1-78923-772-6

Published in London, UK

IntechOpen